CHAPTER FOUR

Apparent Inhibition of Thermal

Decomposition of Bicarbonate

4.1 Introduction

Alkaline scales such as calcium carbonate $CaCO_3$ and magnesium hydroxide $Mg(OH)_2$ are one of the main operational problems in thermal desalination of seawater such as multi stage flash (MSF). Without effective scale control, this can make periodic shut-down of the plant for cleaning essential.[1]

Two main mechanisms have been proposed to explain the formation of alkaline scale in thermal desalination plants. First is the "bimolecular mechanism" that was proposed by Langelier *et al*. in 1950 [2] and second is the "unimolecular mechanism" that was proposed by Dooly and Glater in 1972.[3] In both mechanisms, the first step is the thermal decomposition of bicarbonate ion HCO_3^-.

Currently, it is believed that both bimolecular and unimolecular mechanisms can occur under desalination conditions, as demonstrated by Walinsky and Morton in 1979[4], Mubarak in 1998[5] and Shams El-Din *et al.* in 2002.[6] Note below the values of ΔG° for reactions (Re- 4.1 to Re- 4.6) as cited in Shams El-Din *et al.,* 2005.[7]

$2HCO_3^- \rightleftharpoons CO_3^{2-} + CO_2 + H_2O$ $\qquad \Delta G^{\circ} = +11.506$ kJ/mol at 100 °C $\qquad$ Re- 4.1

$Ca^{2+} + CO_3^{2-} \rightarrow CaCO_3$ $\qquad \Delta G^{\circ} = -62.760$ kJ/mol at 100 °C $\qquad$ Re- 4.2

$CO_3^{2-} + H_2O \rightleftharpoons 2OH^- + CO_2$ $\qquad \Delta G^{\circ} = +43.304$ kJ/mol at 100 °C $\qquad$ Re-4.3

$Mg^{2+} + 2OH^- \rightarrow Mg\,(OH)_2$ $\qquad \Delta G^{\circ} = -78.450$ kJ/mol at 100 °C $\qquad$ Re- 4.4

Although the thermal decomposition of HCO_3^- is a bimolecular reaction, it was reported to follow first order kinetics by Dooly and Glater.[3] That paradox is resolved by assuming the bimolecular reaction involves two primary first order steps. First primary reaction is

$$HCO_3^- \rightleftharpoons OH^- + CO_2 \qquad \Delta G^\circ = +27.405 \text{ kJ/mol at } 100 \text{ °C} \qquad \text{Re- 4.5}$$

In the absence of any competing reaction, the second primary reaction is as a fast acid – base neutralization

$$OH^- + HCO_3^- \rightleftharpoons CO_3^{2-} + H_2O \qquad \Delta G^\circ = -15.899 \text{ kJ/mol at } 100 \text{ °C} \qquad \text{Re- 4.6}$$

The overall reaction is

$$2HCO_3^- \rightleftharpoons CO_3^{2-} + CO_2 + H_2O \qquad \Delta G^\circ = +11.506 \text{ kJ/mol at } 100 \text{ °C}$$

Most investigators in the desalination field believe the mechanism of alkaline scale formation is a more complex process involving competitive equilibria between unimolecular and bimolecular reactions. Moreover, many parameters such as supersaturation, temperature, mixing conditions, impurities, homogenous and heterogeneous nucleation and the effect of additives on calcium carbonate and magnesium hydroxide formation need to be considered and it is very difficult to separate them and investigate independently.[8]

4.2 The effect of scale inhibitor on the thermal decomposition of HCO_3^-

As for all kinetically controlled reactions, the thermal decomposition of HCO_3^- can be catalyzed and inhibited by specific agents. In our knowledge, only three papers have been published on the effect of scale inhibitor on the thermal decomposition of HCO_3^-. Those papers were by Walinsky and Morton (1979)[4], Mubarak (1998)[5] and Shams El-Din (2002)[6]. In those studies, commercial scale inhibitors were used.

4.2.1 Walinsky and Morton (1979)

The effect of commercial scale inhibitor (Flocon Antiscalant 247, 10 ppm as poly maleic acid) on the kinetic of thermal decomposition of HCO_3^- and hydrolysis of CO_3^{2-} in refluxing

synthetic brine which contained ^{14}C- radiolabelled sodium bicarbonate (375 ppm), calcium (824 ppm) and magnesium (1260 ppm) were studied by Walinsky and Morton (1979).

The rate of decomposition of HCO_3^- in absence and presence of scale inhibitor was monitored by radiochemical liquid scintillation assays of production of $^{14}CO_2$. The results showed that the rate of decomposition of HCO_3^- decrease in the presence of scale inhibitor, as well as the presence of calcium and magnesium working as a catalyst for the decomposition of HCO_3^-. They suggested the retardation of decomposition of HCO_3^- in the presence of scale inhibitor proceeded either by the formation of complex from scale inhibitor and Ca^{2+} and/or Mg^{2+} inhibiting the calcium and magnesium catalysed decomposition of HCO_3^- or by preventing the heterogeneous decomposition of HCO_3^- on scale surface.

4.2.2 Mubarak (1998)

The kinetic model of alkaline scale formation in MSF plant at 90 ℃ was developed by Mubarak (1998). The results for refluxing of seawater with/without commercial scale inhibitor (Belgard 2000 as poly maleic acid) for 5.5 hours under ether partial vacuum (68947.6 Pa) or purging nitrogen showed that the decomposition of HCO_3^- follows Re. 4.5 and Re. 4.6 and both reactions as first order reaction and their rate constant is 9.7×10^{-4} and 6.6×10^3 min^{-1} respectively. However, the presence of 10 ppm of Belgard 2000, only affected Re. 4.5 and the rate constant decreased to 9.4×10^{-4} min^{-1}.

The hydrolysis of CO_3^{2-} as Na_2CO_3 for one hour at 100 ℃ showed no significant release of hydroxide ion or loss of CO_3^{2-}, results fairly compatible with Dooly and Glater Mechanism. Generally, Mubarak focused on the mechanism and kinetic model for the decomposition of HCO_3^- at 90 ℃ and demonstrated that both HCO_3^- and generated OH^- were available in the same time in solution. However, this study did not mention the mechanism for the inhibition of thermal decomposition of HCO_3^- by scale inhibitor.

4.2.3 Shams El-Din (2002)

The most comprehensive study on the effect of scale inhibitor on the thermal decomposition of HCO_3^- was by Shams El-Din (2002). The effect of three different polymaleate commercial scale inhibitors on the thermal decomposition of HCO_3^- (150 ppm) was studied in 4% NaCl solution at 100 ºC. The results demonstrated that the thermal decomposition of HCO_3^- follows the Langelier Mechanism "Re. 4.1 and Re 4.3" and has first order kinetics. The concentration of HCO_3^-, CO_3^{2-} and OH^- changing throughout the experiment as $2HCO_3^- = CO_3^{2-} = 2\ OH^-$.

On the other hand, the effect of scale inhibitor on the thermal decomposition of HCO_3^- was clearly on the rate constant of thermal decomposition of HCO_3^- which decreased with increasing of scale inhibitor concentration for all three different scale inhibitors, however by different values. Shams El-Din and his workers believed that, the different behaviour for the scale inhibitors were due to the different on the structure, molecular mass and co-polymerization for scale inhibitors. According to the kinetic model used by Shames El-Din et al. for decomposition of HCO_3^-, the hydrolysis of CO_3^{2-} only begins after HCO_3^- dropped to zero.

Those results were obtained in the absence of calcium or magnesium ions, suggesting that the obvious explanation for the effect of polymeric scale inhibitor advanced by Walinsky and Morton complexation of divalent ions by the PAA cannot catalyse bicarbonate decomposition, cannot be true.

4.2.4 Thermodynamic and kinetics treatment of alkaline scale in MSF

The possibility of reactions may be estimated by the sign and value of their Gibbs free energy ΔG. The values of standard Gibbs free energy of formation (ΔG°) for Re. (4.1 to 4.6) at 25°C and 100 °C were calculated by Shams El-Din et al. (2005).[7]

The results showed all reactions have a positive value of ΔG°, except three reactions (4.2), (4.4) and (4.6) as spontaneous reactions at 100 °C. The first two reactions (4.2) and (4.4) have relatively high negative ΔG° values (-62.760) kJ/mol and (-78.450) kJ/mol and that for the precipitation of $CaCO_3$ and $Mg(OH)_2$ respectively. The third one is the reaction of acid – base neutralization (4.6) which has a small negative ΔG° value (-15.899) kJ/mol and that may be due to the electric repulsion between the two negative reactant species. Other important results were the comparison of ΔG° value for reactions (4.3) and (4.5). Although both have a positive ΔG° value, the probability of the formation of OH^- through reaction (4.5) (ΔG° = +27.405 kJ/mol) is higher than reaction (4.3) (ΔG° = +43.304 kJ/mol) and is compatible with the Dooly and Glater mechanism at high temperature. That study strongly suggests that besides thermodynamics, the kinetics of these reactions play a very important role. On the kinetics term, the author supposes that" the activation energies of scale- forming reactions are temperature – dependent". This can be seen from Figure 4.1 representing the variation of activation energy for reactions (4.5) and (4.6) with temperature. At low temperature, reaction (4.6) has lower activation energy than reaction (4.5) therefore; the calcium carbonate precipitation is more favored than magnesium hydroxide. However, at high temperature this case completely changes, reaction (4.5) has lower activation energy than reaction (4.6) and that causes the scale formation to tend more towards the precipitation of magnesium hydroxide. Note the cross point "transition temperature" on the Figure- representing the temperature which has 50:50 of the composition of $CaCO_3$: $Mg(OH)_2$ and that depend on the seawater composition and the conditions of experiments. The value of this point is between 82- 90.5 °C.
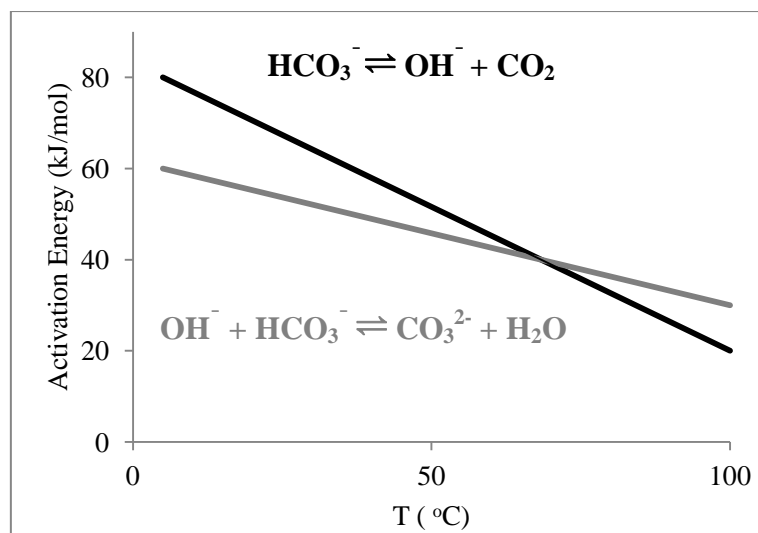
Figure 4.1- Schematic presentation of the variation of the activation energies of Re- 4.5 and Re- 4.6 with temperature.

4.3 The objective of this chapter

The objective of this work is to further investigate the role of polycarboxylic acids in controlling the decomposition of bicarbonate, using a series of well-characterised-PAA prepared by ATRP in order to propose a mechanistic basis for any differences in effectiveness observed for different scale inhibitors. Conductivity measurements are applied to assess the capacity of PAA with different end-groups and controlled molecular weights in retarding the thermal decomposition of HCO_3^- at boiling water (97.2 ± 0.5 °C). The important difference between this study and previous work is that the scale inhibitors which were used in this study have been synthesised in a controlled manner in our laboratory and fully characterised, while commercial scale inhibitors have been used in previous studies. The Pitzer model was used to calculate the activity coefficient for the ions which are believed to contribute in the alkaline scale mechanism and standard Gibbs free energy of formation ΔG° and ΔG were calculated for each reaction under MSF conditions.

4.4 Advance thermodynamic treatment of alkaline scale in MSF desalination plants

The previous thermodynamic treatment of alkaline scale in literature for MSF plants using standard Gibbs free energy of formation (ΔG°) is considered as a basic treatment and its results were not enough to give a clear picture for alkaline scale formation in MSF plants.[7]

In this section, the thermodynamic calculations for the activity coefficients, ΔG° and ΔG of the ions and reactions that cause alkaline scale formation in MSF plants will be described.

4.4.1 Pitzer Model

The Pitzer model was used to calculate the activity coefficients γ of HCO_3^-, CO_3^{2-}, OH^-, Ca^{2+}, Mg^{2+} and CO_2 at 25 °C and 100 °C under the condition of seawater and concentrated brine. The Pitzer equations for each ion are as follows

$$ln\left(\gamma(HCO_3^-)\right) = f^{\gamma} + 2m_{Na}\left(B_{NaHCO_3} + m_{Cl}C_{NaHCO_3}\right) + m_{Na}\,m_{Cl}\left(B_{NaCl}' + C_{NaCl}\right) +$$
$$m_{Cl}\left(2\theta_{Cl-HCO_3} + m_{Na}\,\psi_{Cl-HCO3-Na}\right)^* \qquad \text{Eq- 4.1}$$

$$ln\left(\gamma(CO_3^{2-})\right) = 4f^{\gamma} + 2m_{Na}\left(B_{Na_2CO_3} + m_{Cl}C_{Na_2CO_3}\right) + 4m_{Na}\,m_{Cl}\,B_{NaCl}' +$$
$$2m_{Na}\,m_{Cl}\,C_{NaCl} + m_{Cl}\left(2\theta_{Cl-CO_3} + 2\theta_{Cl-CO3}^{E} + m_{Na}\,\psi_{Cl-CO3-Na}\right)^* \qquad \text{Eq- 4.2}$$

$$ln\left(\gamma(OH^-)\right) = f^{\gamma} + 2m_{Na}\left(B_{NaOH} + m_{Cl}C_{NaOH}\right) + m_{Na}\,m_{Cl}\left(B_{NaOH}' + C_{NaOH}\right) +$$
$$m_{Cl}\left(2\theta_{OH-Cl} + \theta_{OH-Cl}^{E} + m_{Na}\,\psi_{OH-Cl-Na}\right)^* \qquad \text{Eq- 4.3}$$

* Millero, F. *et. al.* (2007)[9]

$$ln\left(\gamma\left(Ca^{2+}\right)\right) =$$

$$4f^{\gamma} + 2m_{Cl}\left(B_{CaCl_2} + m_{Na}C_{CaCl_2}\right) + 4m_{Na}\,m_{Cl}\,B'_{NaCl} + 2m_{Na}\,m_{Cl}\,C_{NaCl}\ +$$

$$m_{Na}\left(2\theta_{NaCa} + 2\theta^{E}_{Na-Ca} + m_{Cl}\,\psi_{Na-Ca-Cl}\right)^{**} \hspace{3cm} \text{Eq- 4.4}$$

**Christov and Moller (2004)[10]

$$ln\left(\gamma\left(Mg^{2+}\right)\right) =$$

$$4f^{\gamma} + 2m_{Cl}\left(B_{MgCl_2} + m_{Na}C_{MgCl_2}\right) + 4m_{Na}\,m_{Cl}\,B'_{NaCl} + 2m_{Na}\,m_{Cl}\,C_{NaCl}\ +$$

$$m_{Na}\left(2\theta_{Na-Mg} + 2\theta^{E}_{Na-Mg} + m_{Cl}\,\psi_{Na-Mg-Cl}\right) \hspace{3cm} \text{Eq- 4.5}$$

$$ln\left(\gamma\left(CO_2(aq)\right)\right) = 2\,m_{Na}\left(\lambda_{Na-CO_2} + \lambda_{Cl-CO_2}\right) + m_{Na}\,m_{Cl}\,\xi_{NaCl-CO_2} \hspace{2cm} \text{Eq- 4.6}$$

$$\ln a(H_2O) = -\left(\frac{2\,m_{NaCl}}{55.51}\right)\emptyset \hspace{4cm} \text{Eq- 4.7}$$

Where $\emptyset$ value is given by:

$$\emptyset - 1 = f^{\phi} + m_c B^{\phi}_{ca} + m_c m_a C^{\phi}_{ca} \hspace{4cm} \text{Eq- 4.8}$$

And f^{γ} in Eqs. $(4.1 - 4.5)$ is Debye-Hückel term as follows

$$f^{\gamma} = -A_{\emptyset}\left[\frac{I^{0.5}}{(1+1.2I^{0.5})} + \frac{2}{1.2}\ln\left(1 + 1.2I^{0.5}\right)\right] \hspace{2cm} \text{Eq- 4.9}$$

Where values of $A_{\emptyset}$ valid from 0 to 350 °C are given by [11] as follows

$$A_\emptyset = 0.36901532 - 6.32100430 \times 10^{-4}T + \frac{9.14252359}{T} - 1.35143986 \times 10^{-2}lnT +$$

$$\frac{2.26089488\times10^{-3}}{T-263} + 1.92118597 \times 10^{-6}\,T^2 + \frac{45.2586464}{680-T} \qquad \text{Eq- 4.10}$$

4.4.1.1 The values of Pitzer parameters (B_{MX}, $B\acute{}\,_{MX}$ and C_{MX}) in EQs. 4.1- 4.5 are given by Millero, F. *et. al.,* (2007)[9] as follows

$$B_{MX} = \beta^\circ_{MX} + \left(\frac{\beta^1_{MX}}{2I}\right)[1 - (1 + 2I^{0.5})\exp(-2I^{0.5})] \qquad \text{Eq- 4.11}$$

$$B\acute{}\,_{MX} = \left(\frac{\beta^1_{MX}}{2I^2}\right)[-1 + (1 + 2I^{0.5} + 2I\exp(-2I^{0.5})] \qquad \text{Eq- 4.12}$$

$$C_{MX} = \frac{C^\phi_{MX}}{(2|Z_M Z_X|^{0.5})} \qquad \text{Eq- 4.13}$$

$$B^\emptyset_{NaCl} = \beta^\circ_{NaCl} + \beta^1_{NaCl}\,exp(-2I^{0.5}) \qquad \text{Eq- 4.14}$$

4.4.1.2 The effect of temperature in Pitzer parameters (B_{MX}, $B\acute{}\,_{MX}$ and C_{MX}) for carbonate system are given by Millero, F. *et. al.,* (2007)[9] as follows

$$\beta^{(0)}_{NaHCO_3}(T) = 0.028 + 0.00048\,(T - 298.15) - (3.2 \times 10^{-4}(T - 298.15)^2) - (1 \times$$

$$10^{-8}\,(T - 298.15)^3) \qquad \text{Eq- 4.15}$$

$$\beta_{NaHCO_3}^{(1)}(T) = 0.044 + 0.002\,(T - 298.15) - (2.7 \times 10^{-5}(T - 298.15)^2) - 2 \times 10^{-7}\,(T - 298.15)^3 \qquad \text{Eq- 4.16}$$

$$C_{NaHCO_3}^{(\emptyset)}(T) = -0.01243 + 1 \times 10^{-5}\,(T - 298.15) + (8.0 \times 10^{-7}(T - 298.15)^2)$$

$$\text{Eq- 4.17}$$

$$\beta_{Na_2CO_3}^{(0)}(T) = 0.0362 + 0.00506\,(T - 298.15) + (2.034 \times 10^{-4}(T - 298.15)^2) - (3.926 \times 10^{-6}\,(T - 298.15)^3) + (2.197 \times 10^{-8}\,(T - 298.15)^4) - (3.97 \times 10^{-11}\,(T - 298.15)^5) \qquad \text{Eq- 4.18}$$

$$\beta_{Na_2CO_3}^{(1)}(T) = 1.51 - 0.0076\,(T - 298.15) - (9.13 \times 10^{-4}(T - 298.15)^2) + (1.592 \times 10^{-5}\,(T - 298.15)^3) - (8.59 \times 10^{-8}\,(T - 298.15)^4) - (1.528 \times 10^{-10}\,(T - 298.15)^5) \qquad \text{Eq- 4.19}$$

$$\beta_{Na_2CO_3}^{(\emptyset)}(T) = 0.052 - 0.00115\,(T - 298.15) - (7.1 \times 10^{-5}(T - 298.15)^2) + (1.2546 \times 10^{-6}\,(T - 298.15)^3) - (6.765 \times 10^{-9}\,(T - 298.15)^4) + (1.199 \times 10^{-11}\,(T - 298.15)^5) \qquad \text{Eq- 4.20}$$

4.4.1.3 The values of $\beta_{MX}^{(O)}$, $\beta_{MX}^{(1)}$ and β_{MX}^{ϕ} at 25 °C and 100 °C for NaCl, NaOH, MgCl₂ and CaCl₂ are given by Pitzer (1986)[12] and Neck, V. *et. al.* (1997)[13] as shown in Table 4.1

Table 4.1- The values of $\beta_{MX}^{(O)}$, $\beta_{MX}^{(1)}$ and β_{MX}^{ϕ} at 25 °C and 100 °C

Electrolyte	$\beta_{MX}^{(O)}$		$\beta_{MX}^{(1)}$		β_{MX}^{ϕ}	
	25 °C	100 °C	25 °C	100 °C	25 °C	100 °C
NaCl	0.0754	0.1002	0.2770	0.3326	0.70×10^{-3}	-1.65×10^{-3}
NaOH	0.0864	0.0827	0.2530	0.3985	2.05×10^{-2}	6.15×10^{-5}
MgCl₂	0.3509	0.3242	1.651	1.989	2.301×10^{-2}	-1.193×10^{-3}
CaCl₂	0.3053	0.3024	1.708	2.049	7.61×10^{-4}	-2.088×10^{-3}

4.4.1.4 The values of higher order terms θ_{ij} and Ψ_{ijk} are given in Millero and Pierrot (1998)[14] as shown in Table 4.2.

Table 4.2- The values of higher order terms θ_{ij} and Ψ_{ijk}

i	j	k	θ_{ij}	Ψ_{ijk}
Cl	HCO₃	Na	0.0359	–0.0143
Cl	CO₃	Na	–0.053	0.016
OH	Cl	Na	–0.05	–0.006
Na	Ca	Cl	0.05	–0.003
Na	Mg	Cl	0.07	0.0199

4.4.1.5 The relationship between the neutral terms λ_{Na-CO_2} and $\xi_{NaCl-CO_2}$ and temperature T are given by Millero *et. al.* (2007)[9] and He and Mores (1993)[15] as follows

$$\lambda_{Na-CO_2} = -5.310 + \frac{279.630}{T} + 0.78810 lnT \qquad \text{Eq- 4.21}$$

$$\xi_{NaCl-CO_2} = 0.39750 + \frac{19.70}{T} + 0.05960 lnT \qquad \text{Eq- 4.22}$$

$$\lambda_{Cl-CO_2} = 0 \qquad \text{Eq- 4.23}$$

The results of calculation of activity coefficients for HCO_3^- , CO_3^{2-}, OH^-, Ca^{2+}, Mg^{2+} and CO_2 (aq) at 25 °C and 100 °C under the condition of seawater and concentrated brine by using Pitzer model (Eq- 4.1 to 4.22) are given in Table 4.3. The values of activity coefficients for those ions at 25 °C are very close to the values in literature as shown in Table 4.3.

Table 4.3- The activity coefficients of HCO_3^-, CO_3^{2-}, OH^-, Ca^{2+}, Mg^{2+} and CO_2 at S= 3.5 % and 25 °C and 100 °C for seawater and concentrated brine

Activity coefficient	Seawater			Concentrated Brine (CF=1.4)	
	25 °C		100°C	25 °C	100°C
	This study	value in literature*	This study	This study	This study
$\gamma_{HCO_3^-}$	0.569	0.574	0.528	0.532	0.507
$\gamma_{CO_3^{2-}}$	0.038	0.035	0.023	0.019	0.012
γ_{OH^-}	0.265	0.263	0.246	0.182	0.161
$\gamma_{Ca^{2+}}$	0.215	0.214	0.156	0.201	0.140
$\gamma_{Mg^{2+}}$	0.227	0.219	0.160	0.211	0.141
γ_{CO_2} (aq)	1.112	1.13	1.106	1.160	1.149
a_{H2O}	0.977	0.981	0.977	0.968	0.968

* Harvie, C, *et. al* (1984)[16] and Millero and Pierrot (1998)[14]

4.4.2 Calculation of enthalpy (ΔH_f°) and Gibbs free energy (ΔG_f°)

The values of standard enthalpy of formation (ΔH_f°) and standard Gibbs free energy of formation (ΔG_f°) at different temperature for competitive reactions such as (Re- 4.1 to Re. 4.6) are important to estimate the probability of those competitive reactions and hence the relative probability of the unimolecular and bimolecular mechanisms.

The calculations of ΔH_f° and ΔG_f° for reactions Re- 4.1 to Re. 4.6 were carried out at 25 °C using Eq- 4.24, Eq- 4.25 and standard values of ΔH_f° and (ΔG_f°) for the species were available in references . At 100 °C, the values of ΔG_f° were obtained by applying Eq- 4.26 as shown in Table 4.4.

The results of ΔH_f° at 25 °C showed that (Table 4.5), all the competitive reactions are endothermic reactions except Re-4.6 which is an exothermic reaction ($\Delta H_f^\circ = -40.983$ kJ/mol). As well as, there is a small difference in values of ΔG_f° at 100 °C in this study and Shams El-Din calculations (2005). The reason for that is the calculations in this study were done based on the G° values for CO_2 and H_2O in aqueous solution. However, Shams El-Din calculations it seems were done based on the G° values for CO_2 and H_2O in gas phase at 100 °C.

$$\Delta H^o = \sum n_P \, \Delta H_P^o - \sum n_R \, \Delta H_R^o \qquad\qquad \text{Eq- 4.24}$$

$$\Delta G_f^o = \sum n_P \, \Delta G_P - \sum n_R \, \Delta G_R \qquad\qquad \text{Eq- 4.25}$$

$$\Delta G_f^o = \Delta H_f^o - T\Delta S^o \qquad\qquad \text{Eq- 4.26}$$

Table 4.4- Standard values of ΔH_f° and (ΔG_f°) for some species available in references.

| Constituent | 25 °C | | | 100 °C |
	ΔH_f° kJ/mol	S° J/deg mol	ΔG_f° kJ/mol	ΔG_f° kJ/mol
HCO_3^-	-691.992	91.211	-586.848	-726.029
CO_3^{2-}	-677.139	-56.902	-527.895	-655.905
CO_2 (aq)	-413.798	117.570	-386.016	-457.671
OH^-	-229.994	-10.753	-157.293	-225.982
H_2O (aq)	-285.830	69.915	-237.178	-311.919
Ca^{2+}	-542.832	-53.137	-553.543	-523.004
$CaCO_3$	-1206.917	92.885	-1128.843	-1241.577
Mg^{2+}	-466.851	-138.072	-454.801	-415.329
$Mg(OH)_2$	-924.538	63.178	-833.578	-948.115

Table 4.5- The values of enthalpy (ΔH_f°) and Gibbs free energy (ΔG_f°) changes associated with scale formation reactions at 25 °C and 100 °C

| Reaction | 25 °C | | 100 °C |
	ΔH° kJ/mol	ΔG_f° kJ/mol	ΔG_f° kJ/mol
$HCO_3^- \rightleftharpoons OH^- + CO_2$ (aq)	+48.200	+43.539	+42.376
$OH^- + HCO_3^- \rightleftharpoons CO_3^{2-} + H_2O$	-40.983	-20.933	-15.815
$2HCO_3^- \rightleftharpoons CO_3^{2-} + H_2O + CO_2$ (aq)	+7.217	+22.606	+26.561
$Ca^{2+} + CO_3^{2-} \rightleftharpoons CaCO_3$	+13.054	-47.405	-62.667
$CO_3^{2-} + H_2O \rightleftharpoons 2OH^- + CO_2$ (aq)	+89.183	+64.471	+58.191
$Mg^{2+} + 2OH^- \rightleftharpoons Mg(OH)_2$	+2.301	-64.191	-80.820

The equilibrium constant (K_{eq}) for reactions Re- 4.1 to Re- 4.6 and solubility product (K_{sp}) for scale formation ($CaCO_3$ and $Mg(OH)_2$) of reactions Re- 4.2 and Re- 4.4 at 25 °C and 100°C were obtained by applying Eq- 4.27 and the results are presented in Table 4.6.

$$K = e^{\frac{-\Delta G^O}{RT}}$$ Eq- 4.27

Table 4.6- The values of Equilibrium Constant (K_{eq}) and Solubility Product (k_{sp}) changes associated with scale formation reactions at 25 °C and 100 °C

Reaction	25 °C		100 °C	
	K_{eq}	K_{sp}	K_{eq}	K_{sp}
$HCO_3^- \rightleftharpoons OH^- + CO_2$ (aq)	2.35×10^{-8}	-	1.76×10^{-4}	-
$OH^- + HCO_3^- \rightleftharpoons CO_3^{2-} + H_2O$	$4.65 \times 10^{+3}$	-	$1.64 \times 10^{+2}$	-
$2HCO_3^- \rightleftharpoons CO_3^{2-} + CO_2$ (aq) $+H_2O$	1.09×10^{-4}	-	2.88×10^{-2}	-
$Ca^{2+} + CO_3^{2-} \rightleftharpoons CaCO_3$ (s)	$2.02 \times 10^{+8}$	4.95×10^{-9}	$5.92 \times 10^{+8}$	1.69×10^{-9}
$CO_3^{2-} + H_2O \rightleftharpoons 2OH^- + CO_2$ (aq)	5.06×10^{-12}	-	1.08×10^{-6}	-
$Mg^{2+} + 2OH^- \rightleftharpoons Mg(OH)_2$ (s)	$1.76 \times 10^{+11}$	5.67×10^{-12}	$2.06 \times 10^{+11}$	4.85×10^{-12}

4.4.3 Estimation of Gibbs free energy (ΔG) for the competitive reactions under desalination conditions

The free energy (ΔG) for the competitive reactions (Re- 4.1 to Re- 4.6) under thermal desalination conditions pH = 8.1, pH = 9 and CF = 1.4 was estimated by using Eq-4.28.

$$\Delta G = \Delta G^o + RT \ln Q$$ Eq- 4.28

The concentrations of species of interest such as Ca^{2+} and Mg^{2+} were determined based on 35 ‰ of standard seawater. CO_2 (aq) was determined assuming the solution was in equilibrium with the atmosphere and by applying Henry's law Eq- 4.29

$$p_{CO_2} = K_{CO_2} . C_{CO_2}$$
<div align="right">Eq- 4.29</div>

Where, p_{CO_2} is the partial pressure of CO_2 gas in atmosphere which is equal to 367 ppm in this study, K_{CO_2} is the Henry's law constant which is estimated by Eq- 4.30 (proposed by Plummer and Busenberg, 1982)[17] and C_{CO_2} is the concentration of CO_2 in the liquid phase. The results are presented in Figure 4.2.

$$logK_H = 108.3865 + 0.01985076\,T - \frac{6919.53}{T} - 40.4515\log T + \frac{669365}{T^2}$$
<div align="right">Eq- 4.30</div>

The concentration of HCO_3^- in seawater is 140 ppm and CO_3^{2-} were determined from C_{CO2} using the empirical formula for K_{a1} and K_{a2} calculated by Millero *et al*, 2007 [9] as shown in Figure 1.4 in Chapter 1.

The concentration of species of interest under MSF desalination conditions are listed in Table 4.7.
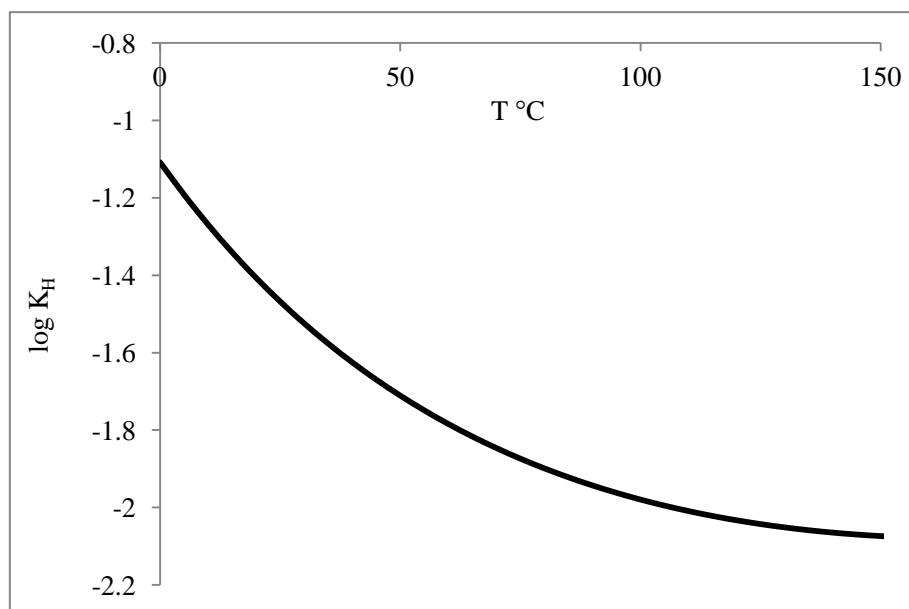
Figure 4.2- log K_H as function of temperature in °C.

Table 4.7- The concentration of species (mol/L) of interest under MSF desalination conditions.

Constituent (mol/L)	concentrated brine(CF=1.4) and pH = 8.1		concentrated brine(CF=1.4) and pH = 9.0	
	25 °C	100 °C	25 °C	100 °C
HCO_3^-	2.62×10^{-3}	2.70×10^{-3}	2.570×10^{-3}	2.49×10^{-3}
CO_3^{2-}	1.52×10^{-5}	2.50×10^{-5}	1.18×10^{-3}	1.90×10^{-4}
CO_2 (aq)	1.25×10^{-5}	3.85×10^{-6}	1.25×10^{-5}	3.85×10^{-6}
OH^-	1.26×10^{-6}		1.00×10^{-5}	
Ca^{2+}	1.47×10^{-2}			
Mg^{2+}	7.63×10^{-2}			

Estimation of Gibbs free energy (ΔG) of the competitive reactions Re-4.1 to Re-4.6 under desalination conditions showed clearly that both unimolecular and bimolecular mechanisms can occur under desalination conditions. For example, at low temperature (T = 25 °C) and pH = 8.1 and pH = 9.0, Re-4.1 ($2HCO_3^- \rightleftharpoons CO_3^{2-} + CO_{2\ (aq)} + H_2O$) has free energy value (ΔG = -9.740 kJ) more negative than the free energy value of Re-4.5 ($HCO_3^- \rightleftharpoons OH^- + CO_{2\ (aq)}$, ΔG = -5.687 kJ) which leads to the calcium carbonate formation being thermodynamically more favored than magnesium hydroxide formation. However, at high temperature (T= 100 °C), that case completely changes, Re-4.5 has free energy value (ΔG = -10.044 kJ) more negative than the free energy value of Re-4.1 (ΔG = -8.602kJ) which tend more towards the precipitation of magnesium hydroxide than calcium carbonate precipitation, as shown in Table 4.8 and Figures 4.4 and 4.5.

The cross point in Figures 4.3 and 4.4 represent the equal possibility of reactions Re- 4.1 and Re- 4.5.at pH = 8.1 and pH = 9.0. The free energy value and temperature under both pH is (ΔG = -8.899 kJ and T = 80. 27 °C) and (ΔG = -3.558 kJ and T = 79.5 °C) respectively. At those temperatures, the possibility of $CaCO_3$: $Mg (OH)_2$ may be equal to 50:50, however; the $Mg (OH)_2$ formation is only favored at high temperature (T > 80 °C) and high pH (pH = 9.0) and may precipitate as a result of the thermal decomposition of bicarbonate following a unimolecular mechanism as shown in Figures 4.5 and 4.6.

At pH = 8.1, the formation of $CaCO_3$ is favored reaction and may precipitate above 45 °C as a result of the thermal decomposition of bicarbonate following bimolecular mechanism. However, $CaCO_3$ may precipitate at low temperature with increase in pH as shown in Figures 4.5 and 4.6.

The acid – base neutralization reaction (Re- 4.6) has a negative value of ΔG at low temperature for both pH. However, with increasing temperature, ΔG of that reaction becomes positive and the inversion point is at T = 80 °C. The direction of the neutralization reaction may represent the threshold between the unimolecular and bimolecular mechanisms. At low temperature where neutralization is spontaneous, the bimolecular mechanism is likely to predominate, however at high temperature (T > 80 °C) where neutralization is not spontaneous the unimolecular mechanism is likely to predominate.

Those results agree with experimental observations of alkaline scale formation in thermal desalination, strongly suggesting that, scale formation in thermal desalination plant is thermodynamically controlled. As mentioned in Chapter 1, an understanding of alkaline scale formation involving competitive equilibria between the unimolecular and bimolecular decomposition of bicarbonate has not yet been achieved. In our knowledge, we are the first researchers who have done these calculations. The author, who works as a researcher in the

Desalination Research Institute, Saudi Arabia, believes that these results for advanced thermodynamic treatments of the formation of alkaline scale in thermal desalination are a turning and a starting point in the understanding of the mechanism of alkaline scale formation in desalination.

Table 4.8- The values of Gibbs free energy (ΔG) changes associated with scale formation reactions at 25 °C and 100 °C for brine solution (CF=1.4) at pH = 8.1 and 9.0 ($[HCO_3^-]$ = 160 ppm)

Reaction	ΔG concentrated brine factor (CF=1.4) and pH = 8.1		ΔG concentrated brine factor (CF=1.4) and pH = 9.0	
	25 °C	100 °C	25 °C	100 °C
$HCO_3^- \rightleftharpoons OH^- + CO_2$ (aq)	-5.687	-10.044	-0.495	-4.710
$OH^- + HCO_3^- \rightleftharpoons CO_3^{2-} + H_2O$	-4.052	+1.442	-4.055	+1.525
$2HCO_3^- \rightleftharpoons CO_3^{2-} + CO_2$ (aq) $+H_2O$	-9.740	-8.602	-4.550	-3.190
$Ca^{2+} + CO_3^{2-} \rightleftharpoons CaCO_3$ (s)	+4.347	-10.046	-0.732	-15.068
$CO_3^{2-} + H_2O \rightleftharpoons 2OH^- + CO_2$ (aq)	-1.635	-11.487	+3.559	-6.235
$Mg^{2+} + 2OH^- \rightleftharpoons Mg(OH)_2$ (s)	+21.856	+6.823	+11.583	-3.451
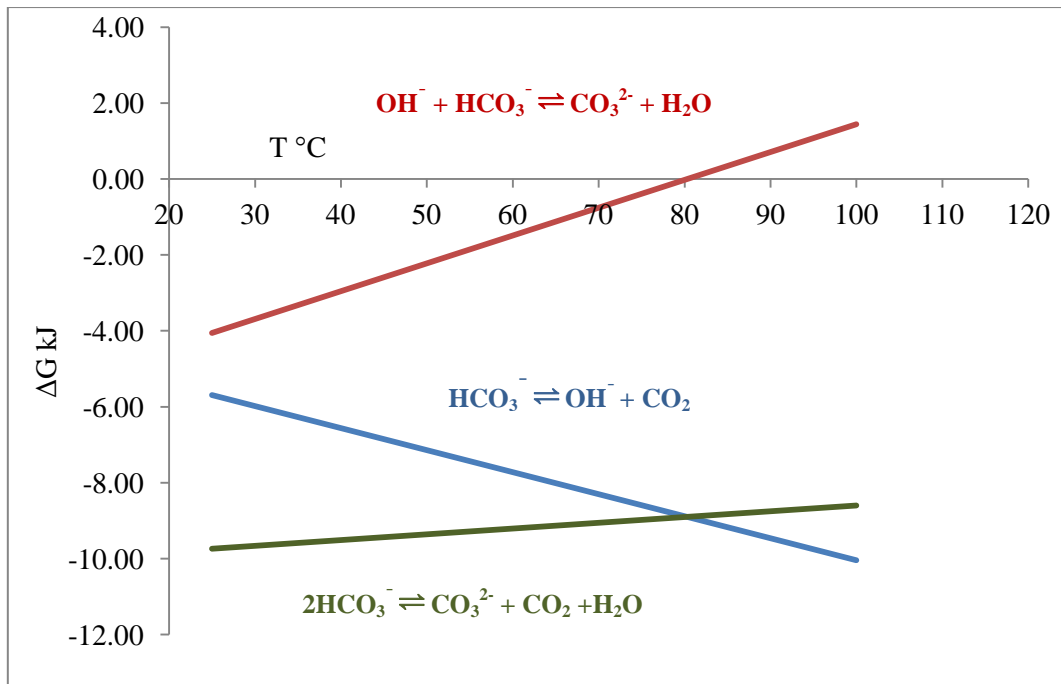
Figure 4.3- The variation of Gibbs free energy (ΔG) associated with alkaline scale formation reactions at 25 °C and 100 °C of brine solution (CF=1.4, pH = 8.1 and $[HCO_3^-]$ = 160 ppm).
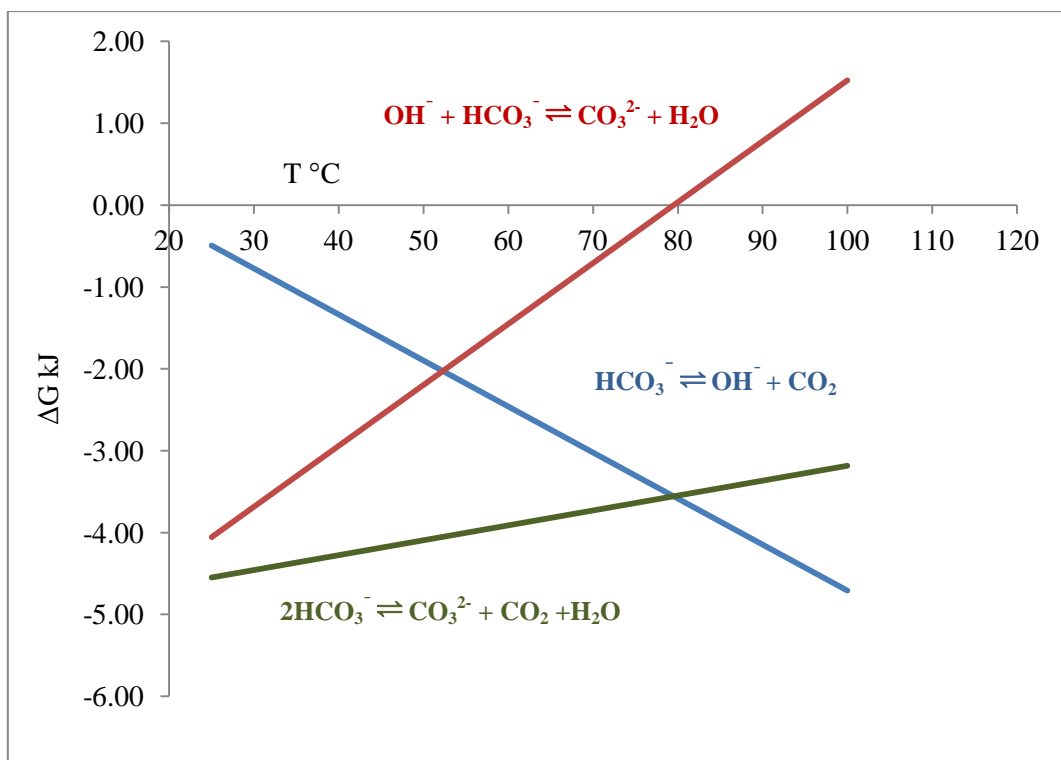
Figure 4.4- The variation of Gibbs free energy (ΔG) associated with alkaline scale formation reactions at 25 °C and 100 °C of brine solution (CF=1.4, pH = 9.0 and $[HCO_3^-]$ = 160 ppm).
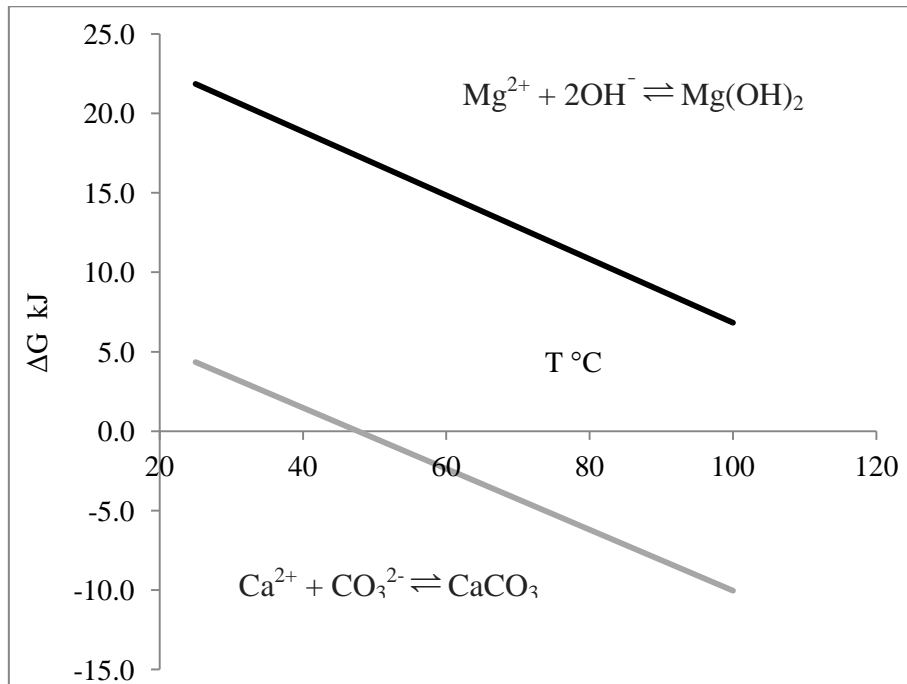
Figure 4.5- The variation of Gibbs free energy (ΔG) associated with alkaline scale formation reactions at 25 °C and 100 °C of brine solution (CF=1.4, pH = 8.1 and [HCO_3^-] = 160 ppm).
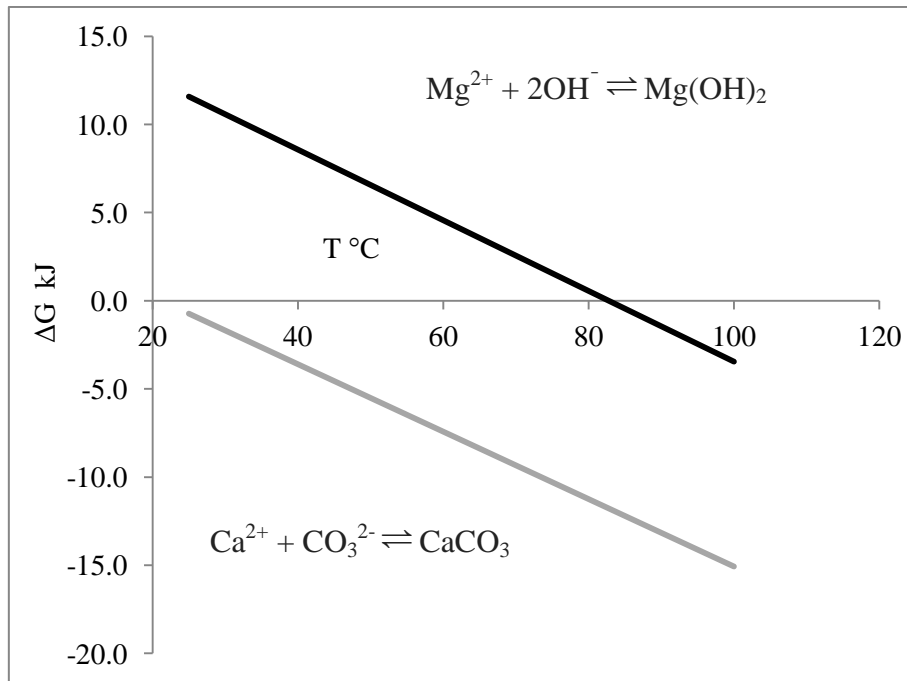
Figure 4.6- The variation of Gibbs free energy (ΔG) associated with alkaline scale formation reactions at 25 °C and 100 °C of brine solution (CF=1.4, pH = 9.0 and [HCO_3^-] = 160 ppm).

4.5 The kinetics of thermal decomposition of HCO_3^- at high temperature

4.5.1 Experiment determination of conductivity at 97.2 °C

A known volume of filtered (0.45µm cellulose acetate membrane) deionized water was placed in a three neck round bottom flask containing a conductivity probe (Eco Scan con 6, Eutech Instruments), thermometer, magnetic stirrer under a water-cooled glass condenser. Measurements were first carried out in the absence of PAA then in the presence of PAA at concentrations of 10, 15 and 30 ppm. When the deionized water began to boil, enough HCO_3^- as $NaHCO_3$ solution was added to ensure a concentration of 40 ppm. Conductivity data was collected from 30 s after addition of the $NaHCO_3$ solution until the conclusion of the experiment. Figure 4.7 represents the system of electrical conductivity measurements for thermal decomposition of HCO_3^- at high temperatures.

The purpose for doing the thermal decomposition of HCO_3^- in the simple system is to study and understand the mechanism of that process experimentally in the absence of the additive, and then to understand the nature of the reaction between carbonic species (HCO_3^- and CO_3^{2-}) and the fully characterized PAA scale inhibitors.
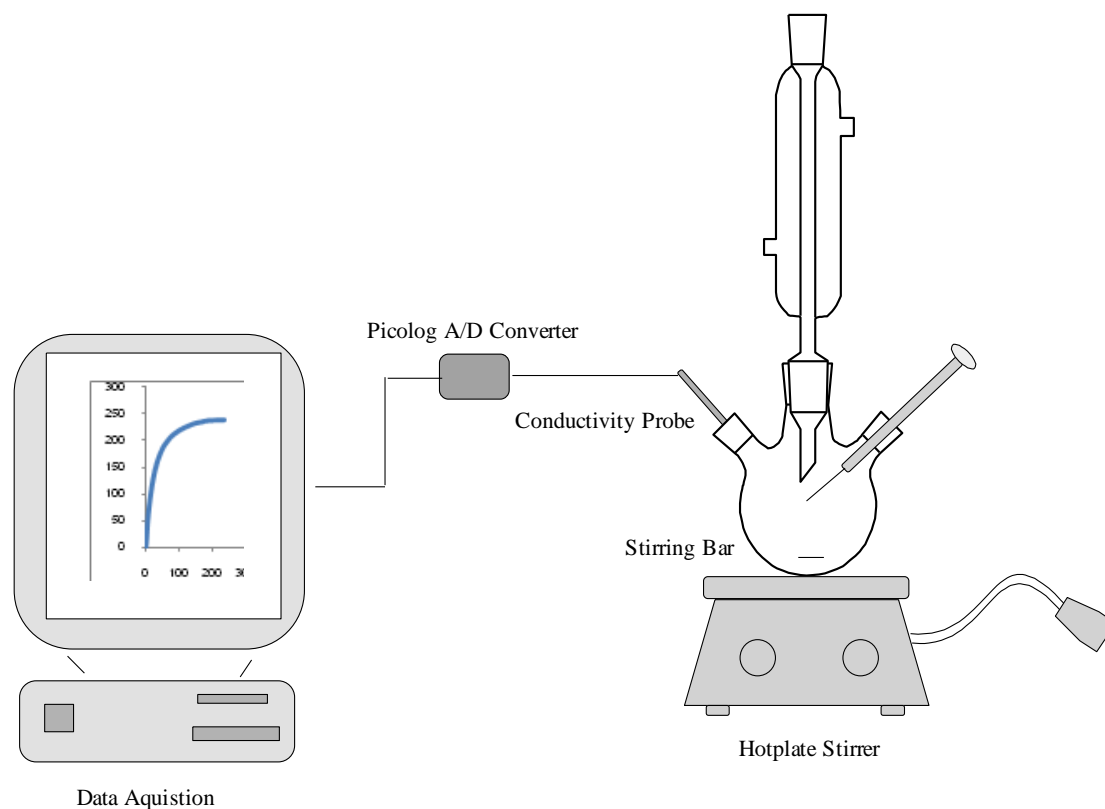
Figure 4.7- Electrical conductivity system for thermal decomposition of HCO_3^-

4.5.2 Derivative of electrical conductivity equation for decomposition of HCO_3^-

The estimation of ions conductivity at high temperature was done using

$$\lambda_{i,T} = \lambda_{i,25\,°C}\,[1 + \alpha(T - 25°C)] \hspace{3cm} \text{(Eq- 4.31)}$$

Where α is a temperature coefficient and its value for all ions ≈ 0.02 °C^{-1} except H_3O^+ ($\approx$ 0.0139 °C^{-1}) and OH$^-$(≈ 0.018 °C^{-1}) and λ_i is the equivalent conductivity of ion i. The equivalent conductance of HCO_3^-, CO_3^{2-} and OH$^-$ at 25 (CRC Handbook of Chemistry and Physics) and 97.2 °C are summarized in Table 4.9.

Table 4.9- Equivalent conductivities of HCO_3^-, CO_3^{2-} and OH^- at 25 (CRC Handbook of Chemistry and Physics) and 97.2 °C

Ions	λ (S.cm^2 /eq)/1000 25 °C	λ (S.cm^2 /eq)/1000 97.2 °C
HCO_3^-	0.0445	0.1088
CO_3^{2-}	0.0693	0.1694
OH^-	0.1991	0.4579

The derivation of electrical conductivity equation for thermal decomposition of HCO_3^- at high temperature was for the cases in the absence and presence of PAA as follows (Pilling & Seakins (1995)[18] & Belfares et al., (1993).[19]

4.5.2.1 In the absence of PAA

The conductivity of solution (K) in the unit of S/cm can be expressed as

$$K = \frac{\sum \lambda_i\, C_i\, Z_i}{1000} \tag{Eq- 4.32}$$

Where, λ_i is the equivalent conductivity of ion i in (S.cm^2/eq), C_i the molarity of ion i and Z_i its charge.

The total conductivity (K_T) at initial time (t = 0) for the thermal decomposition of HCO_3^- as NaHCO$_3$ at high temperature (T = 97.2 °C) is given by

$$(K_T)_0 = \left[(K_{H2O}) + (\lambda_{Na^+} \times [Na^+]_0) + \left(\lambda_{HCO_3^-} \times [HCO_3^-]_0 \right) \right] \tag{Eq- 4.33}$$

Where, K_{H2O} is the conductivity of deionized water.

The total conductivity (K_T) at any time over the experiment (t = t) for the systems of $2HCO_3^- \rightleftharpoons CO_3^{2-} \rightleftharpoons 2OH^-$ and the system of $HCO_3^- \rightleftharpoons OH^-$ at high temperature (97.2 °C) is given by

$$(K_T)_t = (K_{H2O}) + (\lambda_{Na^+} \times [Na^+]_t) + (\lambda_{HCO_3^-} \times [HCO_3^-]_t) + (2 \times \lambda_{CO_3^{2-}} \times [CO_3^{2-}]_t) +$$

$$(\lambda_{OH^-} \times [OH^-]_t) \hspace{4cm} \text{(Eq- 4.34)}$$

In equations 4.33 and 4.34, the conductivity of deionized water and Na^+ (K_{H2O} and K_{Na}^+) are constant (C). Therefore, Eq- 4.33 and Eq- 4.34 should be written as

$$(K_T)_0 = C + (\lambda_{HCO_3^-} \times [HCO_3^-]_0) \hspace{3cm} \text{(Eq- 4.35)}$$

$$(K_T)_t = C + (\lambda_{HCO_3^-} \times [HCO_3^-]_t) + (2 \times \lambda_{CO_3^{2-}} \times [CO_3^{2-}]_t) + (\lambda_{OH^-} \times [OH^-]_t)$$

$$\text{(Eq- 4.36)}$$

At the end of experiment ($t = \infty$) equation (4.36) will be

$$(K_T)_\infty = C + (\lambda_{OH^-} \times [OH^-]_\infty) \hspace{3cm} \text{(Eq- 4.37)}$$

Therefore,

$$\Delta K = (K_T)_\infty - (K_T)_0 = (\lambda_{OH^-} \times [OH^-]_\infty) - (\lambda_{HCO_3^-} \times [HCO_3^-]_0) \hspace{1cm} \text{(Eq- 4.38)}$$

As $[HCO_3^-]_0 = [OH^-]_\infty$

$$\Delta K = (K_T)_\infty - (K_T)_0 = [HCO_3^-]_0 \times [(\lambda_{OH^-}) - (\lambda_{HCO_3^-})] \hspace{1cm} \text{(Eq- 4.39)}$$

If the thermal decomposition of HCO_3^- follow first-order kinetics, then

$$ln[(K_T)_\infty - (K_T)_t] = -kt + a \hspace{3cm} \text{(Eq- 4.40)}$$

The plot of $ln[(K_T)_\infty - (K_T)_t]$ vs. time (t), the slope = -k (rate coefficient)

In the absence of PAA, equation (4.40) was applied to analyze the conductivity data and calculate rate coefficient by the plot of $\ln[(K_T)_\infty - (K_T)_t]$ *vs.* time (t), where the slope $= -k$ (rate coefficient)

4.5.2.2 In the presence of PAA

In the presence of PAAs, $(K_T)_0$, $(K_T)_t$ and $(K_T)_\infty$ can be written as

$$(K_T)_0 = (K_{H2O}) + (K_{Na^+}) + (K_{PAA}) + \left(\lambda_{HCO_3^-} \times [HCO_3^-]_0\right) \qquad \text{(Eq- 4.41)}$$

Over the experiment, the carboxylic acid groups in PAA were neutralized by OH^- that was generated as the final product of thermal decomposition of HCO_3^-. Therefore, $(K_T)_t$ can be written as

$$(K_T)_t = (K_{H2O}) + (K_{Na^+}) + (K_{PAA}) + \left(\lambda_{HCO_3^-} \times [HCO_3^-]_t\right) + \left(2 \times \lambda_{CO_3^{2-}} \times [CO_3^{2-}]_t\right) +$$

$$(\lambda_{OH^-} \times [OH^-]_t) + (\lambda_{PA^-} \times [PA^{n-}]_t) \qquad \text{(Eq- 4.42)}$$

At the steady state, $(K_T)_\infty$ can be written as follow

$$(K_T)_\infty = (K_{H2O}) + (K_{Na^+}) + (\lambda_{OH^-} \times [OH^-]_t) + (\lambda_{PA^-} \times [PA^{n-}]_t) \qquad \text{(Eq- 4.43)}$$

In equations 4.41, 4.42 and 4.43 K_{H2O} and K_{Na^+} are constant (C) and K_{PAA} is very small and can be ignored. Therefore, ΔK can be written as follow

$$\Delta K = (K_T)_\infty - (K_T)_0 = [(\lambda_{OH^-} \times [OH^-]_\infty) + (\lambda_{PA^-} \times [PA^{n-}]_\infty)] - \left(\lambda_{HCO_3^-} \times [HCO_3^-]_0\right)$$

$$\text{(Eq- 4.44)}$$

The concentration of carboxylic acid groups at different concentration of PAA (10, 15 and 30 ppm) were calculated in the monomolar units. Therefore, the equivalent of OH^- which need to neutralize all of them will be known over the experiment and after that time the

conductivity of PA$^-$ will not change until reaching the steady state. Eq- 4.44 can be written as follow

$$\Delta K = (K_T)_\infty - (K_T)_0 = (\lambda_{OH^-} \times [OH^-]_\infty) - \left(\lambda_{HCO_3^-} \times [HCO_3^-]_0\right) + K_{PA^{n-}} \quad \text{(Eq- 4.45)}$$

If the decomposition of HCO_3^- follow first-order kinetics, then

$$ln\,[(K_T)_\infty - (K_T)_O] = -kt + a \qquad \text{(Eq- 4.46)}$$

The plot of $ln[(K_T)_\infty - (K_T)_t]$ vs. time (t), the slope = $-k$ (rate coefficient)

Equation 4.42 (Eq- 4.42) can be rearranged to calculate the conductivity of PA^{n-} as follows

$$K_{PA^-} = \Delta K_{EXP} - \Delta K_{Blank} + K_{OH^-}(\text{Consuming}) \qquad \text{(Eq- 4.47)}$$

Equation (Eq- 4.47) was used to calculate the conductivity (K) of PA^{n-}.

4.6 Results and Discussion

To determine the rate coefficient for thermal decomposition of HCO_3^- and the inhibition of that decomposition by PAA with different end groups and molar mass, the conductivity measurements were collected under the following conditions: T= 97.2 ± 0.5 °C, $[HCO_3^-]$ = 6.557×10^{-4} M (40 ppm), and scale inhibitor concentration [PAA] =10, 15, 30 ppm with different end groups and molecular mass.

Based on the experimental conductivity data, the results can be distinguished in two sections:

4.6.1 Section one: The kinetic model of thermal decomposition of HCO_3^- in absence of PAA

Theoretically, when 40 ppm of HCO_3^- converts solely to OH$^-$, the pH of the final solution should be 10.81. Under the experiment conditions employed, the final experimental pH value

was found to be 10.73. Moreover, the theoretical change in conductivity (ΔK) for the overall system ($HCO_3^- \rightarrow OH^-$) of 6.557×10^{-4} (40 ppm) HCO_3^- as $NaHCO_3$ was calculated to $\Delta K = 228$ µS/cm using Eq- 4.39. Experimentally, the value ($\Delta K = 224 \pm 7$ µS/cm) was obtained. This is an excellent agreement between theory and experiment.

In absence of PAA, the equation (Eq. 4-40) was applied to analyze the conductivity data and determine rate coefficient by plot of $\ln[(K_T)_\infty - (K_T)_t]$ *vs.* time (*t*), where the rate coefficient (*k*) = - slope. The plot (Figure- 4.8) shows a very good linear ($R^2 > 0.996$, n= 52) relationship for overall reaction clearly indicating the thermal decomposition of HCO_3^- follows first order kinetics with $k = 3.35 \times 10^{-2}$ min^{-1}. The concentration of CO_3^{2-} in the system associated with the presence of HCO_3^- and OH^- can be calculated by

$$[CO_3^{2-}] = [HCO_3^-] \times [OH^-] \times 164 \qquad \text{(Eq. 4.48)}$$

Where

$$K_{eq} = \frac{[CO_3^{2-}]}{[HCO_3^-] \times [OH^-]} = 164$$
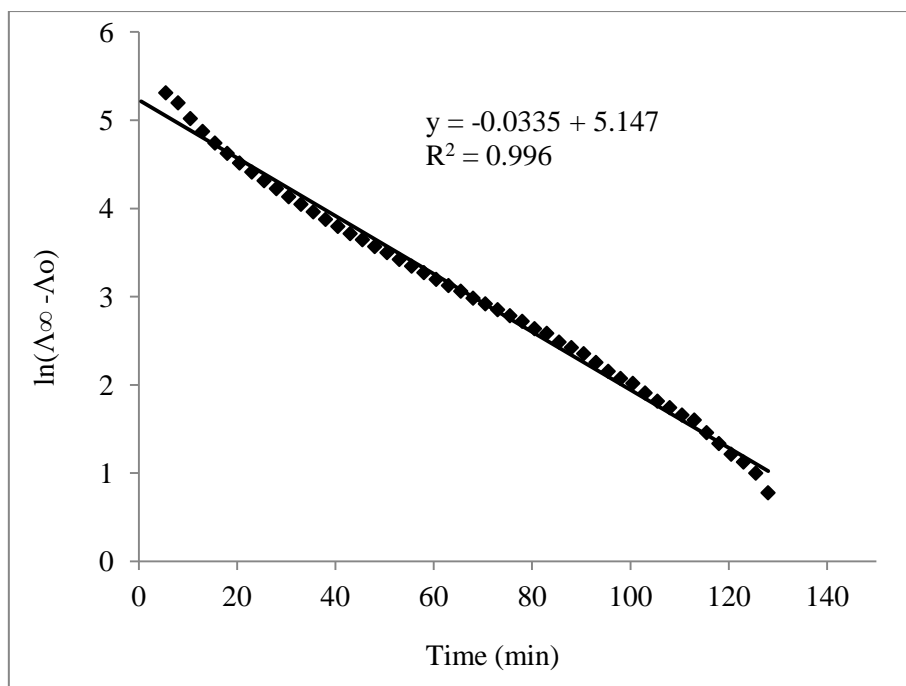
Figure 4.8- The overall rate coefficient of thermal decomposition of 40 ppm HCO_3^-

4.6.1.1 Thermodynamic treatment for thermal decomposition of HCO_3^-

It is not apparent whether the thermal decomposition of HCO_3^- is a unimolecular reaction or a bimolecular reaction following first-order kinetics. The two possibilities may be differentiated by considering the thermodynamics of the system (reference to the thermodynamics results above, section 4.4, p.146).

ΔG *vs.* time for Re. 4.1 and Re. 4.5 as a first step in both bimolecular mechanism and unimolecular mechanism under experimental conditions was calculated and the results are shown in Figure 4.9. ΔG for the unimolecular mechanism (Re. 4.5) is more negative and probable than ΔG for the bimolecular mechanism (Re. 4.1) at all times.
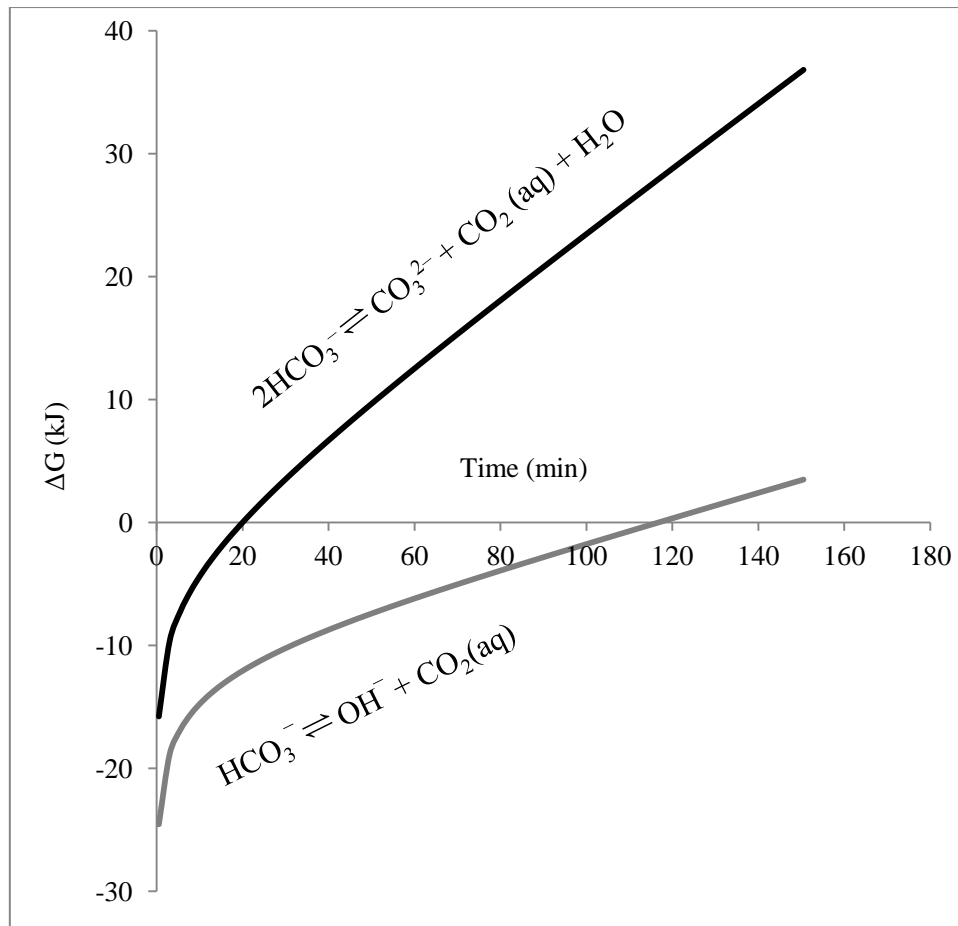
Figure 4.9- Free energy (ΔG) changes with time for the decomposition of 40 ppm of bicarbonate as unimolecular mechanism and bimolecular mechanism.

In the case where the thermal decomposition of HCO_3^- follows the unimolecular mechanism, the equation for first order kinetics can be applied to follow the concentration of HCO_3^- during experiment (Figure 4.10) which is given as

$$\ln \frac{[HCO_3^-]_0}{[HCO_3^-]_t} = kt \qquad \text{(Eq- 4.49)}$$

Where $[HCO_3^-]_0$ and $[HCO_3^-]_t$ are the initial concentration and the residual amount at time (t) of HCO_3^- respectively.
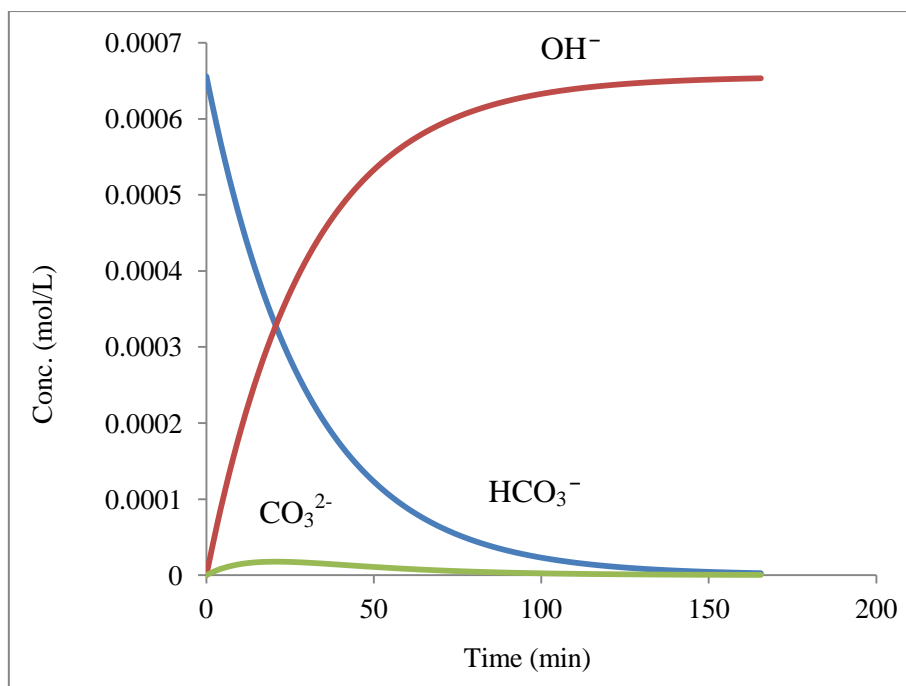
Figure 4.10- The concentration of HCO_3^- (blue curve), OH^- (red curve) and CO_3^{2-} (green curve) for thermal decomposition of HCO_3^- as unimolecular mechanism in the absence of PAA

4.6.2 Section two: Thermal decomposition of HCO_3^- in the presence of PAA

To study the effect of PAA on the thermal decomposition of HCO_3^-, conductivity measurements (ΔK) and the pH of the 40 ppm HCO_3^- solution under the same experimental conditions were collected. Two points were observed in the comparison between ΔK and pH in the absence and presence of PAA. First, ΔK (μS/cm) values in the presence of PAA are higher than ΔK for blank solution and those values of ΔK decrease with increasing the concentration of PAA. Second, pH values in the presence of PAA are lower than pH value of blank solution and the pH values decrease with increasing PAA concentration.

These observations can be explained on the fact that, PAA is a weak acidic polyelectrolyte with many ionizable carboxylic acid groups and in aqueous solution at pH > 8.1, PAA is close to fully ionized and should be more conductive than the neutral polymer.

Phenomenon due to the neutralization of carboxylic acid groups in PAA at high pH (pH $\geq$ 10.4) solution by OH^- are as shown in Figure 4.11.
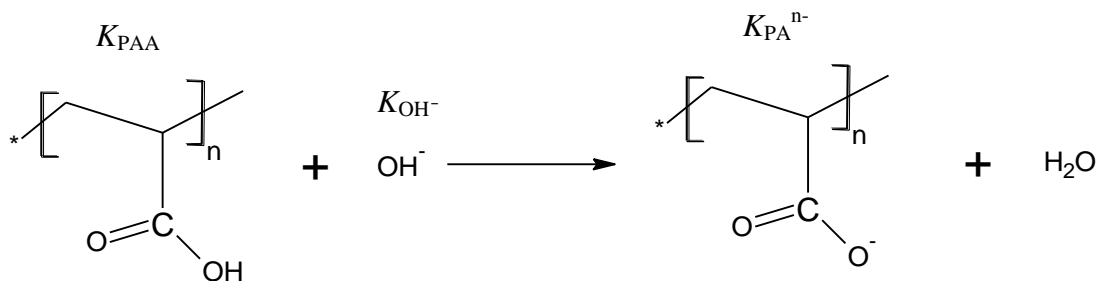
Figure 4.11- The neutralization of carboxylic acid groups in PAA by OH^-

The experimental results of electrical conductivity ΔK (μS/cm) and pH of final solution in presence of PAA with different end groups and molecular mass are summarized in Table 4.10.

Table 4.10- The experimental results of ΔK (μS/cm) and pH of final solution in presence of PAA with different end groups and molecular mass

End Groups of PAA	M_n	[PAA]	pH	ΔK (μS/cm)
Blank			10.73	223.66 ± 6.75
CMM	2106	10	10.61	239.78 ± 8.30
	2106	15	10.53	240.76 ± 8.88
	2106	30	10.40	202.72 ± 3.02
	7633	10	10.62	260.61 ± 2.15
EIB	1669	10	10.58	270.61 ± 7.29
	7180	10	10.59	270.94 ± 11.18
CIB	1689	10	10.60	274.90 ± 1.17
	6210	10	10.59	271.44 ± 5.15
	9954	10	10.56	266.16 ± 2.84
	9954	15	10.49	260.30 ± 5.53
	13209	10	10.65	254.10 ± 5.40
HIB	1403	10	10.55	266.97 ± 6.40
	1403	15	10.52	262.15 ± 6.59
	1403	30	10.35	195.85 ± 0.29
	3563	10	10.58	267.12 ± 8.41
	8928	10	10.59	257.89 ± 2.49
	13049	10	10.65	259.53 ± 0.70
DIB	2422	10	10.55	279.14 ± 3.14
	6203	10	10.52	271.02 ± 2.37
HDIB	1687	10	10.65	273.13 ± 5.19
	1687	15	10.52	254.41 ± 0.46
	4135	10	10.42	272.22 ± 11.62
	9391	10	10.54	278.05 ± 2.75
	17167	10	10.65	273.20 ± 10.32

4.6.2.1 The conductivity of polyacrylate ($PA^{(n-)}$) at high temperature

The electrical conductivity of the solution containing different concentrations of PAA was determined by Bordi, *et al.,* (2002)[21] at room temperature. However, the lowest concentration of PAA in the Bordi *et al.* study was 0.1 M, much higher than the concentration used in this study (1×10^{-6} M) making the comparison between studies s difficult.

In our knowledge, there no data have been reported regarding the conductivity of polyacrylate (PA^{n-}) at high temperature. That makes the estimation of the conductivity for (PA^{n-}) at high temperature due to the neutralization of carboxylic acid groups in PAA by OH^{-} which is the final product on the thermal decomposition of HCO_3^{-} one of the important features of this study.

The estimation of conductivity of (PA^{n-}) at 97.2 °C was carried out by two pathways. Firstly, theoretical estimation of the conductivity of (PA^{n-}) by applying equation 4.47. The results of theoretical conductivity values are summarized in Table 4.11.

Table 4.11- The theoretical conductivity values of $PA^{(n-)}$ with different end groups and molecular mass at high temperature in the units of ($\mu S/cm$) estimated using equation 4.46

End Group of PAA	M_n	[PAA]	[PAA] (M) $\times 10^{-6}$	Monomolar $\times 10^{-5}$	Cond. of OH^- consuming ($\mu S/cm$)	Theoretical Cond. PA^{n-} ($\mu S/cm$)
CMM	2106	10	4.75	2.07	63.05	74.83
		15	7.12	3.10	94.58	107.34
		30	14.25	6.20	189.16	163.88
	7633	10	1.31	2.06	63.59	96.20
EIB	1669	10	5.99	1.98	60.36	102.97
	7180	10	1.39	2.17	66.33	109.27
CIB	1689	10	5.92	1.87	56.93	103.83
	6210	10	1.61	2.03	61.94	105.38
	9954	10	1.00	2.05	62.56	100.72
		15	1.51	3.07	93.84	126.14
	13209	10	0.76	2.06	62.75	88.85
HIB	1403	10	7.13	1.82	55.48	94.45
		15	10.69	2.73	83.22	117.37
		30	21.38	5.45	166.45	134.30
	3563	10	2.81	1.98	60.40	99.52
	8928	10	1.12	2.05	62.57	92.46
	13049	10	0.77	2.06	62.81	94.34
DIB	2422	10	4.13	1.86	56.72	107.86
	6203	10	1.61	2.01	61.27	104.29
HDIB	1687	10	5.93	1.69	51.57	96.70
		15	8.89	2.53	77.36	103.77
	4135	10	2.42	1.92	58.69	102.91
	9391	10	1.06	2.02	61.44	111.49
	17167	10	0.58	2.05	62.42	107.62

Secondly, experimental conductivity of (PA^{n-}) was estimated as follows:

Equation 4.48 was used to follow the concentration of HCO_3^- and OH^- during the experiment. The total conductivities of those ions at 97.2 °C corresponding to their concentration during experiment were used to regenerate a semi-theoretical conductivity curve *vs.* time. Based on the theoretical average number of carboxylic acid units and their concentration in monomol/L, the conductivity of PA^{n-} at 97.2°C was determined by comparing the experimental conductivity curve and semi-theoretical conductivity curve which gives the best matching between them. The electrical conductivities of PA^{n-} with different end groups and molecular mass at 97.2 °C in the units of (μS/cm) and (S.cm^2/monomol) were listed in Table 4.12.

The second pathway was applied first in the absence of PAA to regenerate a semi-theoretical conductivity curve for the decomposition of 40 ppm of HCO_3^- (blank semi-theoretical conductivity curve) assuming the unimolecular mechanism and then compared with the experimental conductivity curve as shown in Figure 4.12.

Figures 4.13 and 4.14 represent examples for estimating the conductivity of PA^{n-} at 97.2 °C for EIB-PAA and CIB-PAA respectively. Table 4.11 represents the estimation of electrical conductivity of $PA^{(n-)}$ with different end groups and molecular mass at 97.2 °C in the units of (μS/cm) and (S.cm^2/monomol).

The agreement between the theoretical and experimental values of the conductivity of PA^{n-} was very good with the correlation coefficient $R^2 = 0.98$ as shown in Figure 4.15.
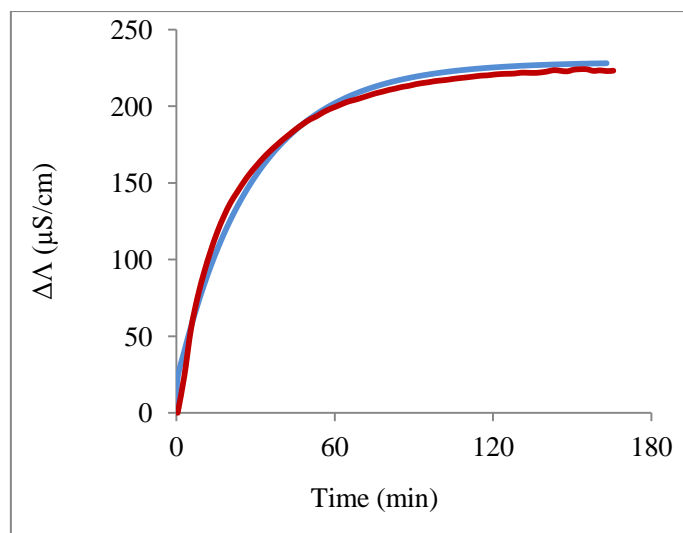
Figure 4.12- Experimental conductivity curve (red curve) and semi- theatrical conductivity curve (blue curve) for thermal decomposition of 40 ppm of HCO_3^- as unimolecular mechanism in absence of PAA (Blank)
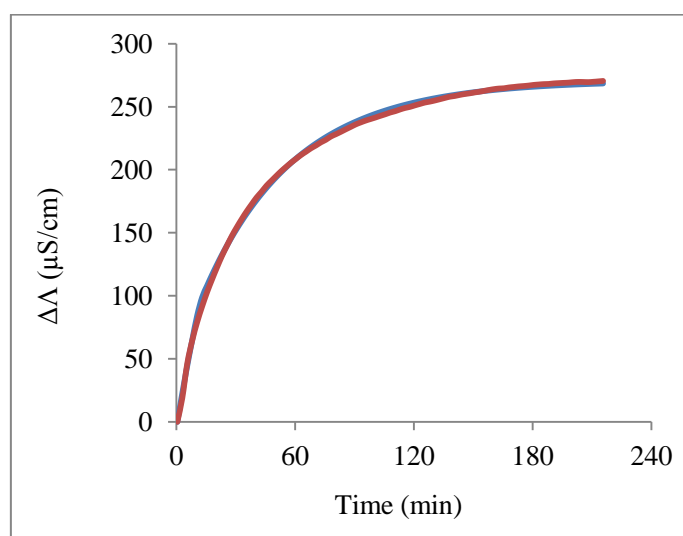
Figure 4.13- Experimental conductivity curve (red curve) and semi- theatrical conductivity curve (blue curve) for thermal decomposition of 40 ppm of HCO_3^- as unimolecular mechanism in presence of 10 ppm of EIB-PAA, (M_n = 7180 g/mol).
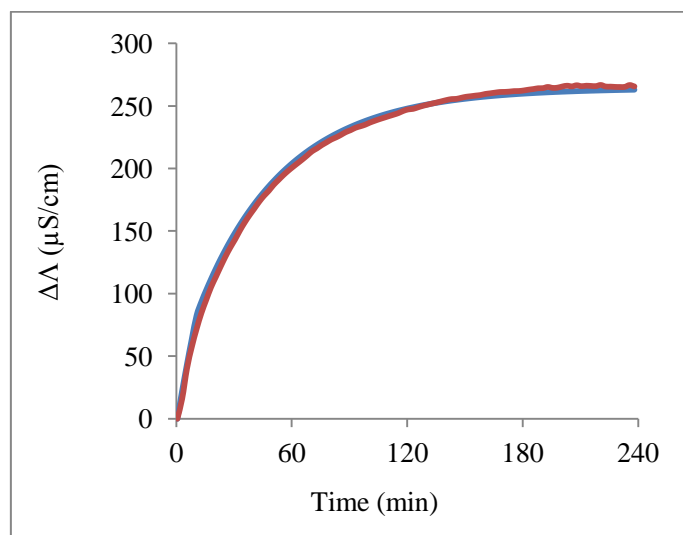
Figure 4.14- Experimental conductivity curve (red curve) and semi- theatrical conductivity curve (blue curve) for thermal decomposition of40 ppm of HCO_3^- as unimolecular mechanism in presence of 10 ppm of CIB-PAA, (M_n = 9954 g/mol).

Table 4.12- The experimental conductivity values of PA^{n-} with different end groups and molecular mass at high temperature in the units of (μS/cm) and (S.cm^2/ monomol).

End Group of PAA	M_n g/mol	Ave. Units (n)	[PAA]	Experimental (K) of PA^{n-} (μS/cm)		Cond. of PA^{n-} (S.cm^2/ monomol)
				mean	$\pm$ RSD	
CMM	2106	29	10	79.87	2.76	0.58 ± 0.02
			15	109.47	4.04	0.53 ± 0.02
			30	165.24	2.46	0.40 ± 0.01
	7633	106	10	98.6	0.81	0.71 ± 0.01
EIB	1669	22	10	106.77	2.88	0.81 ± 0.02
	7180	104	10	112.98	4.66	0.78 ± 0.03
CIB	1689	21	10	104.44	0.44	0.84 ± 0.01
	6210	84	10	108.21	2.05	0.80 ± 0.02
	9954	136	10	102.47	1.10	0.75 ± 0.01
			15	135.26	2.87	0.66 ± 0.01
	13209	181	10	93.18	1.98	0.68 ± 0.01
HIB	1403	17	10	100.57	2.41	0.84 ± 0.02
			15	121.77	3.06	0.67 ± 0.02
			30	138.13	0.20	0.38 ± 0.01
	3563	47	10	104.21	3.28	0.79 ± 0.02
	8928	122	10	95.65	0.92	0.70 ± 0.01
	13049	179	10	97.39	0.26	0.71 ± 0.01
DIB	2422	30	10	111.48	1.25	0.90 ± 0.01
	6203	83	10	107.04	0.94	0.80 ± 0.01
HDIB	1687	19	10	100.24	1.88	0.88 ± 0.02
			15	104.74	0.19	0.62 ± 0.01
	4135	53	10	105.10	4.42	0.82 ± 0.03
	9391	126	10	111.36	1.10	0.83 ± 0.01
	17167	234	10	106.32	4.02	0.77 ± 0.03
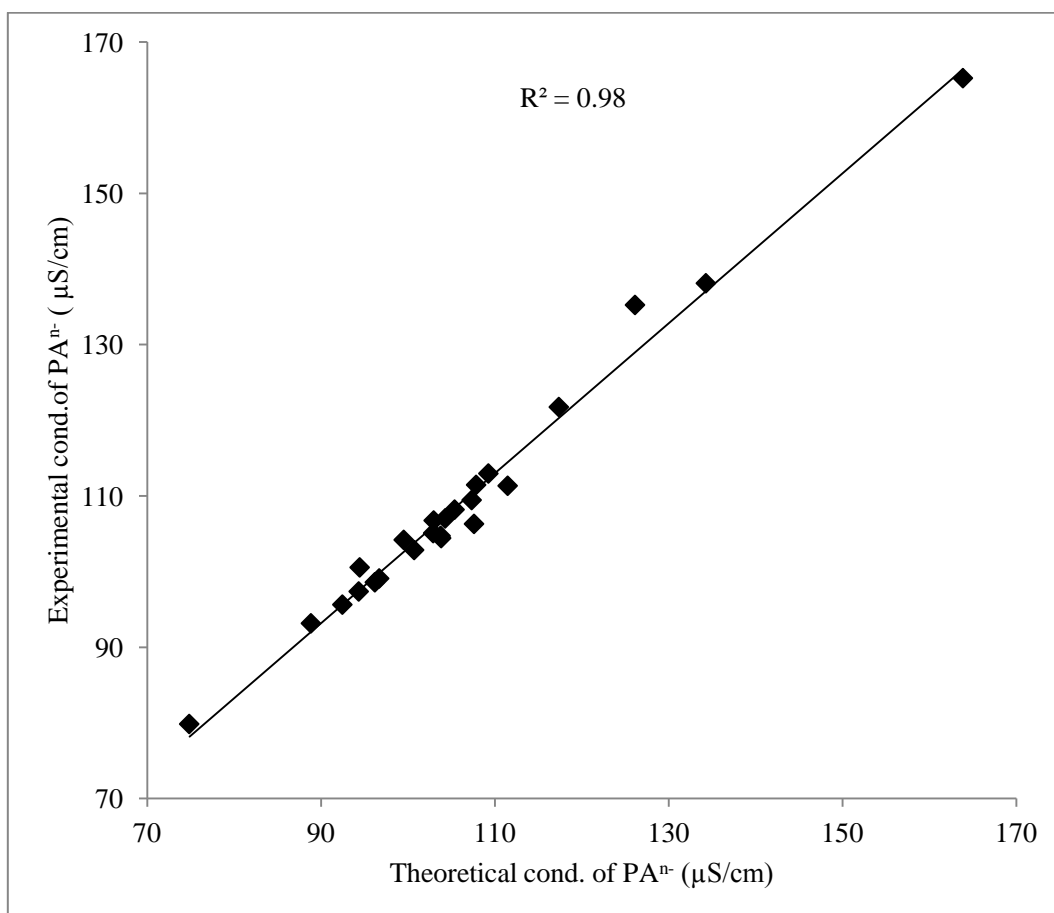
Figure 4.15- The relationship between the theoretical and experimental values of the

conductivity of PA $^{n-}$ at 97.2 °C

The electrical conductivity of PA$^{(n-)}$ with different end groups and molecular mass at high temperature show clearly that the PA$^{(n-)}$ with hydrophobic end groups have electrical conductivity values in units of (μS/cm) and (S.cm^2/monomol) greater than PA$^{(n-)}$ with hydrophilic end group, as shown in Table 4.12 and Figure 4.16.
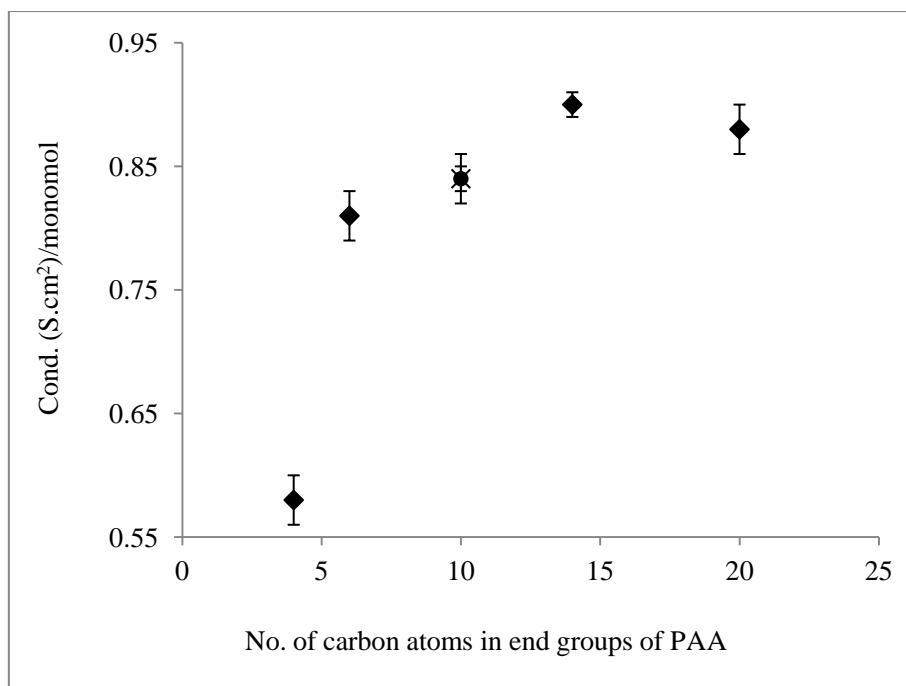
Figure 4.16- The electrical conductivity of PA$^{(n-)}$ with different end groups ($M_n < 2000$ g/mol) at high temperature in unit of (S.cm^2/ monomol)

The equivalent conductivity of PA^{n-} with different end groups and molecular mass was obtained using equation 4.50 (Eq- 4.50) and the results were summarized in Table 4.13.

$$\Lambda = \frac{K}{N}$$ (Eq- 4.50)

Where, N is the normality of the carboxylate groups.

The results of equivalent conductivities of PA^{n-} illustrate that the molecular mass and end groups of PA^{n-} significantly affect on the equivalent conductivities (Table 4.13). The equivalent conductivity increased with increasing hydrophobicity ratio of end group to molecular mass of PA^{n-} (M_{en}/M_n) and decreased with increasing molecular mass of PA^{n-}. Figure 4.17 represents the curve obtained by plotting equivalent conductance against the molecular mass of PA^{n-}. This curve clearly shows that with an increase in molecular mass of

PA^{n-} equivalent conductivity decreases sharply in the range of (1400 – 3500 g/mol) then the decrease was then gradual until M_n=17000 g/mol. .

The equivalent conductivity for all of PAA with different end groups and molecular mass was plotted against the ratio of (M_{ne}/M_n) as shown in Figure 4.18. Figure 4.18 clearly shows a good relationship (R^2 = 0.93) between the equivalent conductivity of PAAs and the ratio of (M_{ne}/M_n). The deviation from that linearity was for PAA with longest end group (HDIB) and different molecular mass, and may be due to the formation of micelles.

The effect of the molecular mass of PA^{n-} on equivalent conductivity is more than that of the corresponding end groups (M_{ne}/M_n). This effect is clearly seen in the comparison of equivalent conductance for the lowest molecular mass of HIB-PA^{n-} (M_n=1386 g/mol) and HDIB-PA^{n-} (M_n=1668 g/mol). Although the ratio of M_{ne}/M_n = 0.187 for HDIB- PA^{n-} (which the highest ratio) is higher than the ratio for HIB-PA^n (M_{en}/M_n= 0.124) however, the later has the highest equivalent conductance 4.941×10^{-2} (S.cm^2/eq).

Table 4.13- The equivalent conductivities of PA^{n-} with different end groups and molecular mass.

End Group of PAA	M_n of PA^{n-} (g/mol)	M_{ne} of end group (g/mol)	Ratio M_{ne}/M_n	Λ of PA^{n-} (S.cm^2/eq) $\times 10^{-2}$
CMM	2077	86.1	0.041	2.000
	7527		0.011	0.670
EIB	1647	115.15	0.070	3.682
	7076		0.016	0.750
CIB	1668	169.24	0.101	4.000
	6126		0.028	0.952
	9818		0.017	0.551
	13028		0.013	0.376
HIB	1386	171.25	0.124	4.941
	3516		0.049	1.681
	8806		0.019	0.574
	12870		0.013	0.397
DIB	2392	227.36	0.095	3.000
	6120		0.037	0.964
HDIB	1668	311.51	0.187	4.684
	4082		0.076	1.547
	9265		0.034	0.659
	16933		0.018	0.329
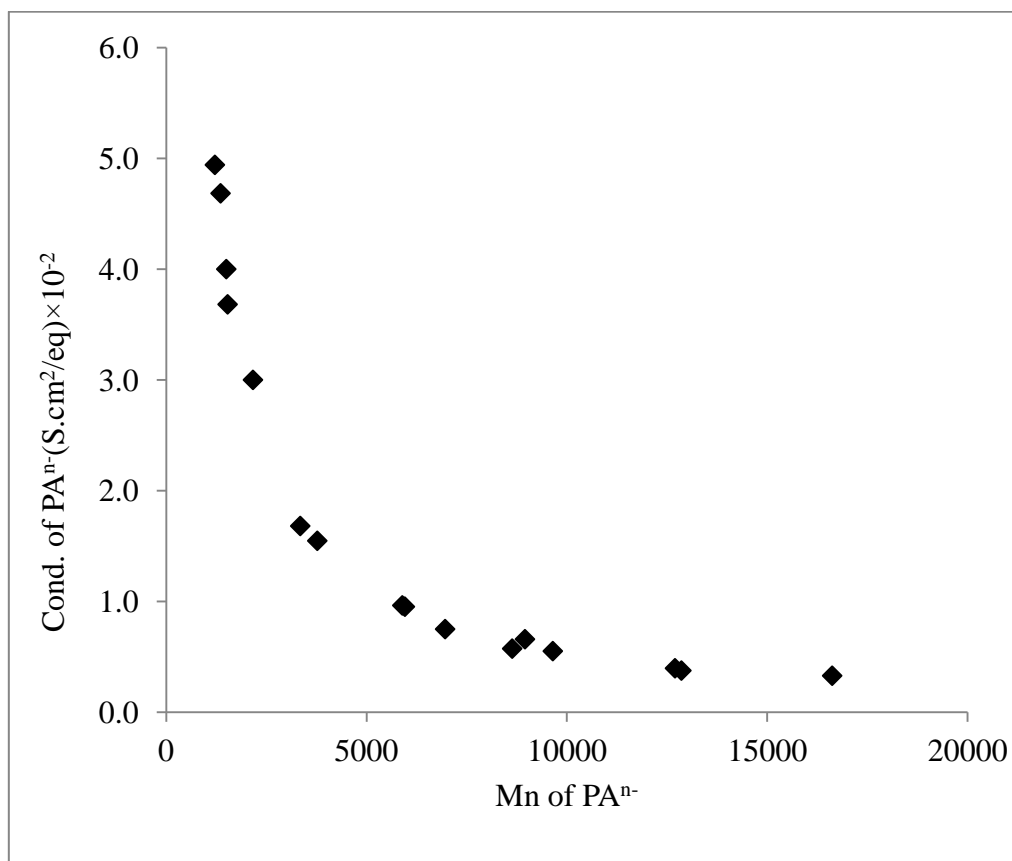
Figure 4.17- Equivalent conductance as a function of the molecular mass of $PA^{(n-)}$
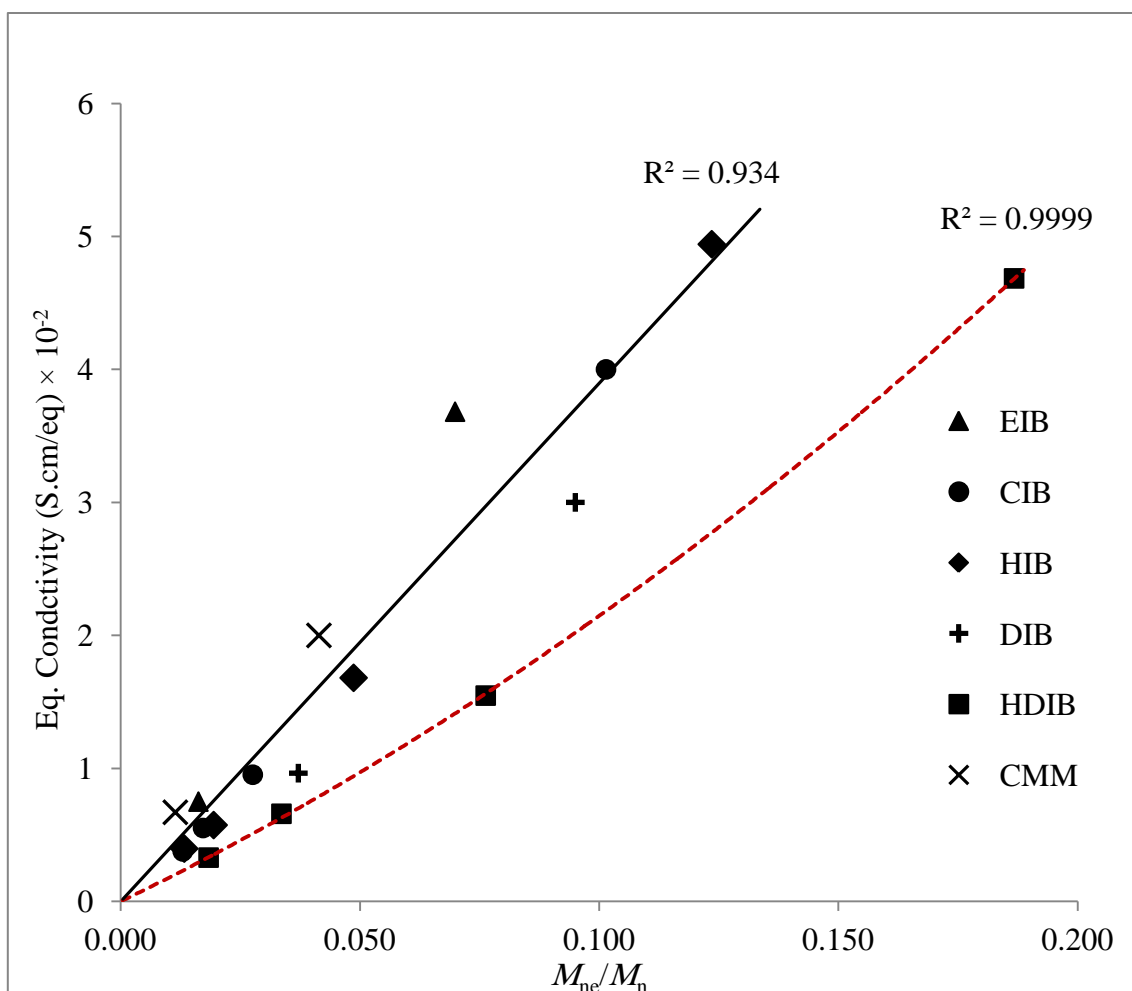
Figure 4.18- Equivalent conductivity as a function of the hydrophobicity ratio of end group to

molecular mass of PA^{n-} (M_{ne}/M_n)

4.6.2.2 The inhibition efficiency of PAA to retard the thermal decomposition of HCO_3^-

To determine the inhibition efficiency of thermal decomposition (% ITD) of HCO_3^- assuming the unimolecular mechanism by different molecular mass and end groups of PAA, equation (Eq- 4.51) was used.

$$\% \ ITD \ of \ HCO_3^- = \left(1 - \frac{k}{k_b}\right) \times 100 \qquad \text{(Eq- 4.51)}$$

Where k_b is the rate coefficient for thermal decomposition of 40 ppm of HCO_3^- in the absence of PAA and k is the rate coefficient for thermal decomposition of 40 ppm of HCO_3^- in the presence of 10, 15 and 30 ppm of PAA, for the following reaction

$$\text{HCO}_3^- \rightleftharpoons \text{OH}^- + \text{CO}_2 \qquad \text{(Re- 4.5)}$$

4.6.2.2.1 The thermal decomposition of 40 ppm HCO_3^- in the presence of 10 ppm of PAA with different end groups and molecular mass

The results of % inhibition of thermal decomposition (% ITD) of 40 ppm HCO_3^- by 10 ppm of PAA with different end groups and molecular mass show that both end groups and molecular mass play very important roles. For all end groups of PAA, the rate coefficient of thermal decomposition of 40 ppm HCO_3^- increased with increasing molecular mass, except PAA with HDIB end group as shown in Table 4.14 and Figure 4.19. The net of reactions for the thermal decomposition of HCO_3^- in the presence of PAA is shown in Figure 4.20.

Table 4.14- Rate coefficient of thermal decomposition of HCO_3^- and % ITD by different molecular mass and end groups of PPA

End Groups of PAA	M_n	[PAA]	$k \times 10^{-2}$ (min^{-1})	% ITD
Blank (HCO_3^-)			3.35 ± 0.10	0
CMM	2106	10	2.27 ± 0.08	32
	2106	15	1.92 ± 0.07	43
	2106	30	1.84 ± 0.03	45
	7633	10	2.29 ± 0.02	32
EIB	1669	10	2.02 ± 0.05	40
	7180	10	2.10 ± 0.09	37
CIB	1689	10	2.01 ± 0.01	40
	6210	10	2.04 ± 0.04	39
	9954	10	2.16 ± 0.02	36
	9954	15	1.91 ± 0.04	43
	13209	10	2.31 ± 0.05	31
HIB	1403	10	1.89 ± 0.05	44
	1403	15	1.74 ± 0.04	49
	1403	30	1.79 ± 0.01	47
	3563	10	2.01 ± 0.06	40
	8928	10	2.16 ± 0.02	36
	13049	10	2.30 ± 0.01	31
DIB	2422	10	1.93 ± 0.02	42
	6203	10	1.99 ± 0.02	41
HDIB	1687	10	2.52 ± 0.05	25
	1687	15	2.49 ± 0.01	26
	4135	10	2.16 ± 0.09	36
	9391	10	2.28 ± 0.02	32
	17167	10	2.47 ± 0.09	26
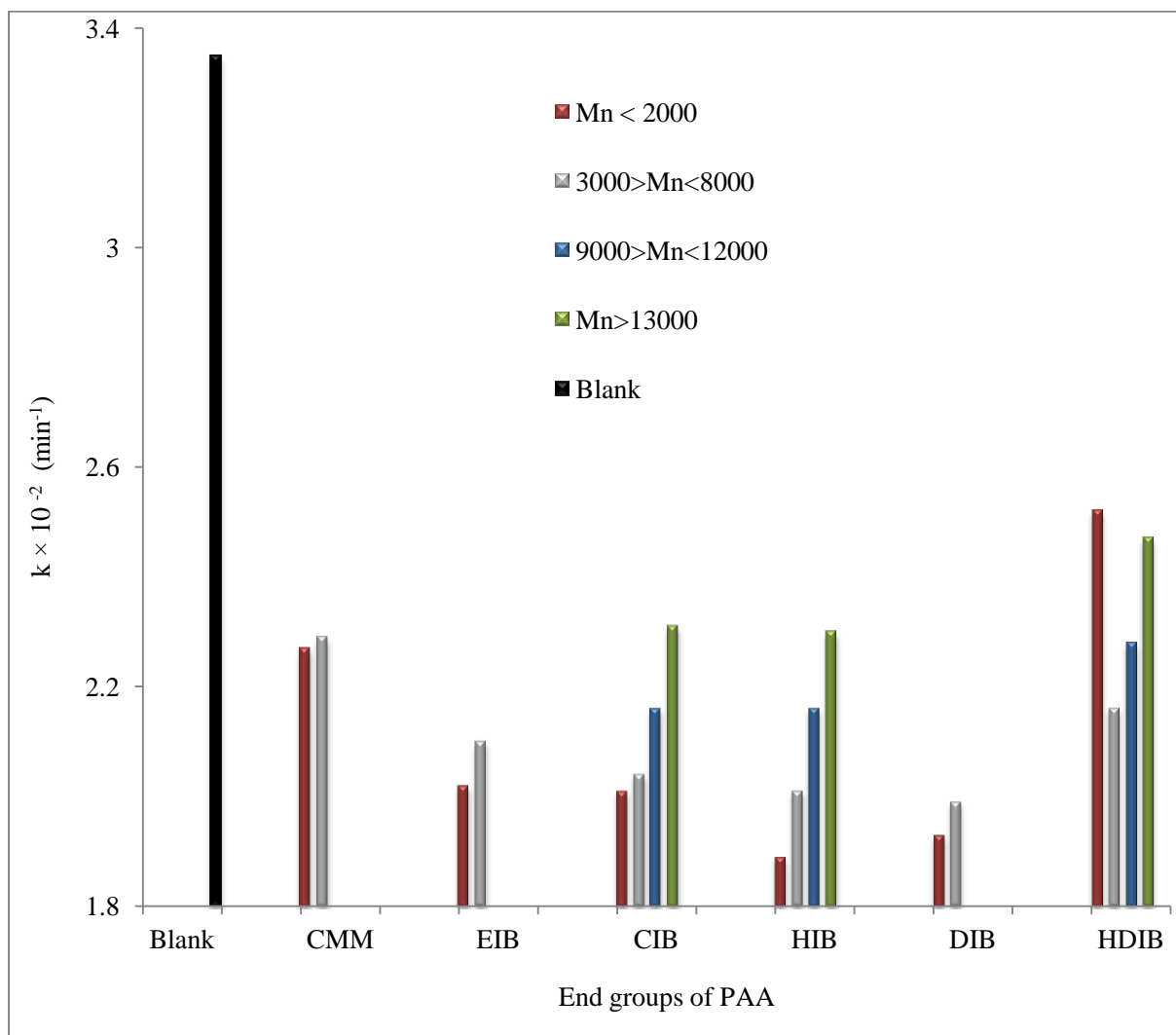
Figure 4.19- Rate coefficient $\times 10^{-2}$ (min^{-1}) for thermal decomposition of 40 ppm HCO$_3^-$ at T = 97 $\pm$ 0.5 °C in the presence of 10 ppm PAA with different end groups and molecular mass. ■ Blank, ■ $M_n < 2000$ g/mol, ■ $M_n = 3000 - 8000$ g/mol, ■ 9000- 120000 g/mol and ■ $M_n > 13000$ g/mol.
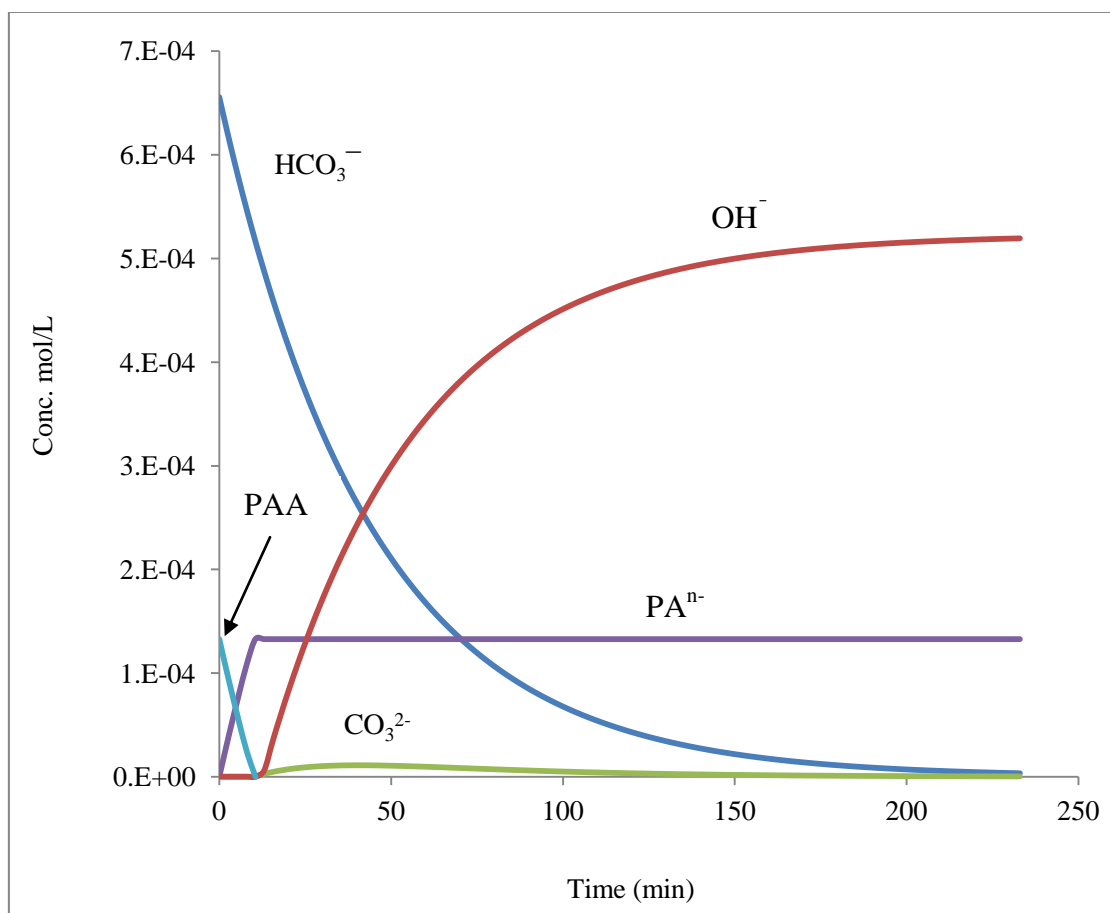
Figure 4.20- The net of reactions for thermal decomposition of HCO_3^- following the unimolecular mechanism

Generally, at 10 ppm of PAA with different end groups and molecular mass, % ITD decreased and rate coefficient of decomposition of 40 ppm HCO_3^- increased in the succession HIB-PAA> DIB-PAA > CIB-PAA> EIB-PAA > HDIB-PAA > CMM-PAA as shown in Table 4.14 and Figure 4.19.

For example, HIB-PAA (M_n=13049 g/mol) has % ITD of HCO_3^- 31 % however, the lowest molecular mass of PAA with CMM and HDIB end groups has % ITD of HCO_3^- 32 % and 25 % respectively. HIB-PAA and DIB-PAA (HIB) in the molecular mass range ($M_n \leq 2000$ g/mol) have the best of % ITD of HCO_3^- 44 % and 42 % respectively. However, PAA with the longest hydrophobic end group (HDIB) (M_n=1687 g/mol) has the lowest % ITD of

HCO_3^- 25 % comparing with all % ITD for PAA with different end groups and molecular mass as a special case as shown in Figure 4.19.

That result may be due to the ratio between hydrophobic chain (end group) and hydrophilic chain (PAA), which is the highest ratio (1:4), compared with the other PAA with different end groups and molecular mass, showing that this polymer has an active surface property. This phenomenon is very clear when the solutions that contain 10 and 15 ppm of this material when boiled, plenty of foam was formed; therefore the % ITD of HCO_3^- was the lowest one. However, in the solution that contained 10 ppm of HDIB-PAA ($M_n \geq 4000$ g/mol) that phenomena disappeared and the % ITD increased. For example, % ITD for HDIB-PAA ($M_n = 4135$ g/mol) and ($M_n = 9391$ g/mol) were 36 % and 32 % respectively.

PAA with EIB and CIB hydrophobic end groups for the molecular mass range (2000- 8000 g/mol) has very close average of % ITD of HCO_3^- 39 % and 40 % respectively. On the other hand, the comparison of % ITD of HCO_3^- between PAA with EIB hydrophobic end group and PAA with CMM hydrophilic end group the result show that, PAA with EIB end group has better average than PAA with CMM hydrophilic end group (39 % and 32 % respectively) as shown in Figures 4.21 and 4.22. Those results represent clearly the effect of the hydrophobicity of end group on % ITD of HCO_3^-. Generally, PAA with CMM hydrophilic end group has the lowest % ITD of HCO_3^- in the range 2000-8000 g/mol of molecular mass.
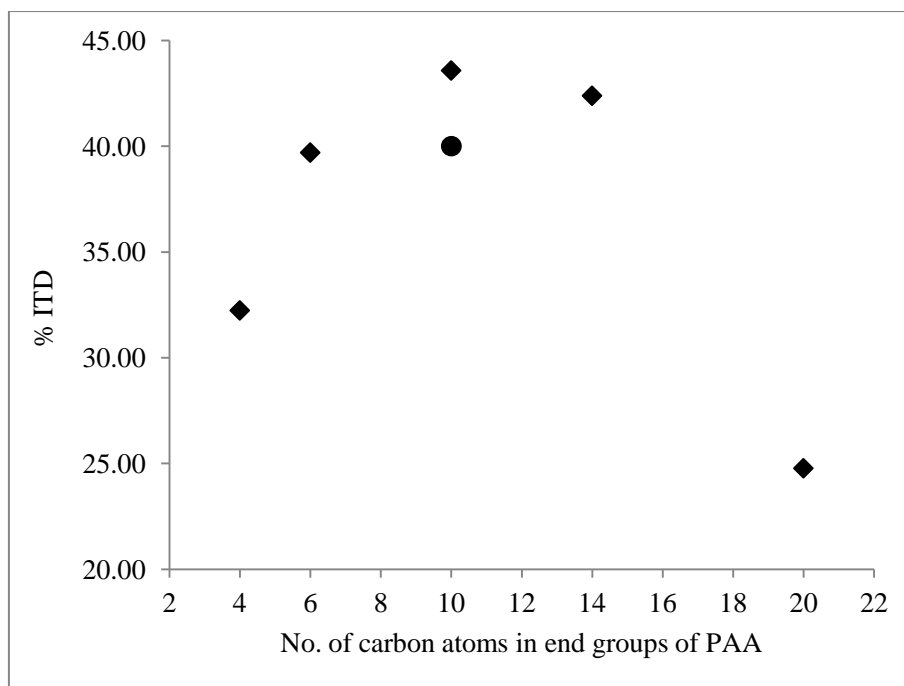
Figure 4.21- % ITD of HCO_3^- by 10 ppm of PAA with different end groups ($M_n \leq 2000$). ($\bullet$ = CIB-PAA)
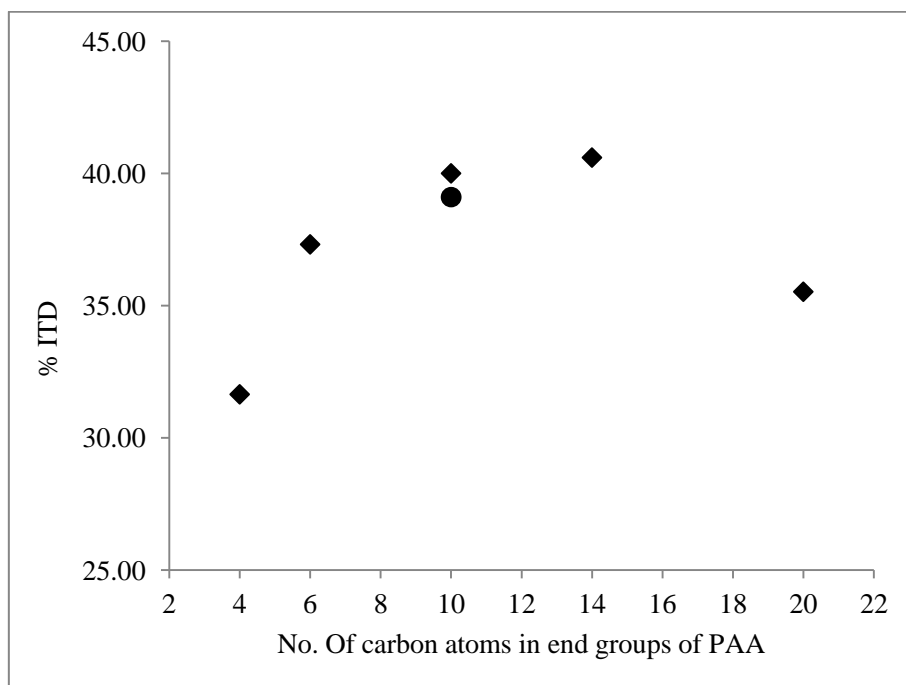
Figure 4.22- % ITD of HCO_3^- by 10 ppm of PAA with different end groups ($3000 < M_n \leq 8000$). ($\bullet$ = CIB-PAA)

4.6.2.2.2 *The thermal decomposition of 40 ppm HCO_3^- in the presence of 15 and 30 ppm of PAA with different end groups and molecular mass*

The effect of increasing concentration of PAA to 15 and 30 ppm on TD of HCO_3^- was studied under the same experimental conditions for the lowest molecular mass of PAA with end groups CMM, HIB and HDIB, and CIB-PAA at molecular mass M_n =9954 g/mol. Onincreasing the concentration of PAA from 10 ppm to 15 ppm, % ITD of HCO_3^- increased significantly by 11 %, 5 % and 7 % for CMM-PAA, HIB-PAA and CIB-PAA respectively. However, the change in the % ITD of HCO_3^- for HDIB-PAA was 1 % only as shown in Figure 4.23.In contrast, the changing on the % ITD of HCO_3^- for CMM-PAA was 2% and for HIB-PAA was insignificant on increasing its concentration from 15 to 30 ppm.
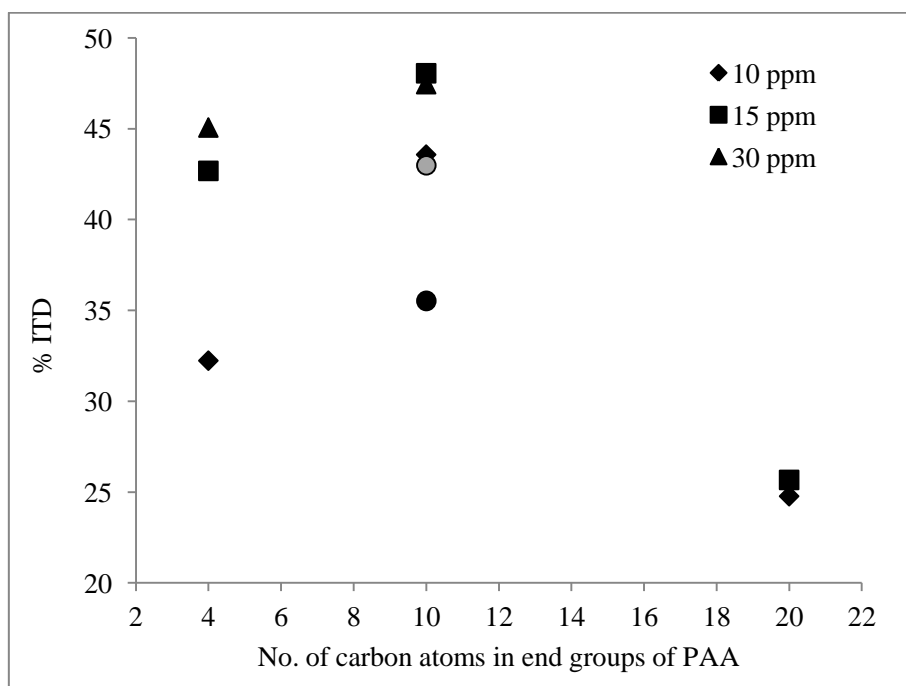
Figure 4.23- % ITD of 40 ppm HCO_3^- at T = 97.2 °C by 10, 15 and 30 ppm of CMM-PAA (M_n = 2106 g/mol), HIB-PAA (M_n= 1403 g/mol), HDIB-PAA (M_n = 1687 g/mol) and CIB-PAA (M_n = 9954 g/mol) (● = [CIB-PAA]=10 ppm and (● = [CIB-PAA]= 15 ppm)

4.6.2.3 The effect of adding 50 ppm NaCl on the ITD of HCO_3^-

If the action of the polymer additive is primarily by its interaction with metal ions (as suggested by Walinsky and Morton, who postulated that the protective effect of PAA arose by complexation of divalent ions which generally hasten bicarbonate decomposition) then addition of positive ions would be expected to accelerate decomposition of bicarbonate. Accordingly, a series of experiments were repeated with an additional 50 ppm NaCl.

The purpose for doing the thermal decomposition of HCO_3^- in solution containing 50 ppm NaCl was to understand the effect of adding NaCl on the ITD of HCO_3^- by the lowest molecular mass of PAA with hydrophobic end groups. The results showed HIB-PAA and DIB-PAA have the best % ITD of HCO_3^- 36% and 34% respectively, as shown in Table 4.15 and Figures 4.24 and 4.25. All rate coefficients for TD of 40 ppm HCO_3^- increases with the addition of 50 ppm NaCl. This may be attributed either to the metal ion complexation between the PAA and Na^+ or 'salting in' effect where less PAA sits on the interface in solutions of higher ionic strength.

Table 4.15- Rate coefficient of thermal decomposition of HCO_3^- and % ITD by different end groups

End Groups of PAA	M_n	[PAA]	Without NaCl		with 50 ppm of NaCl	
			$k \times 10^{-2}$ (min^{-1})	% ITD	$k \times 10^{-2}$ (min^{-1})	% ITD
Blank (HCO_3^-)			3.35	0	3.73	0
EIB	1669	10	2.02	40	2.72	27
CIB	1689	10	2.01	40	2.65	29
HIB	1403	10	1.89	44	2.40	36
DIB	2422	10	1.93	42	2.46	34
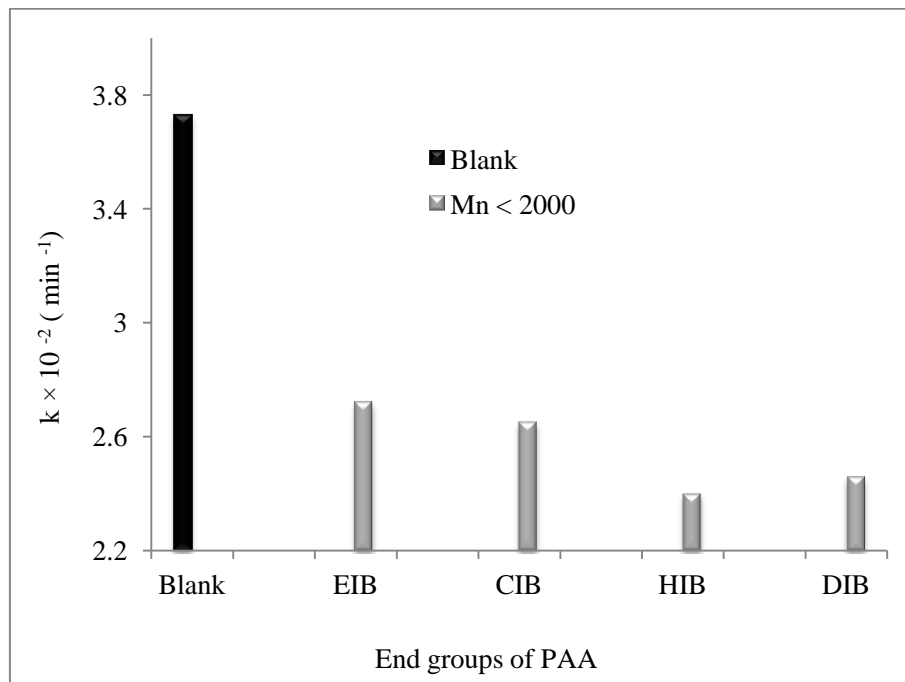
Figure 4.24- Rate coefficient for TD of 40 ppm HCO_3^- at T = 97.2 °C in 50 ppm of NaCl solution and presence of 10 ppm PAA with different end groups ($M_n < 2000$ g/mol)
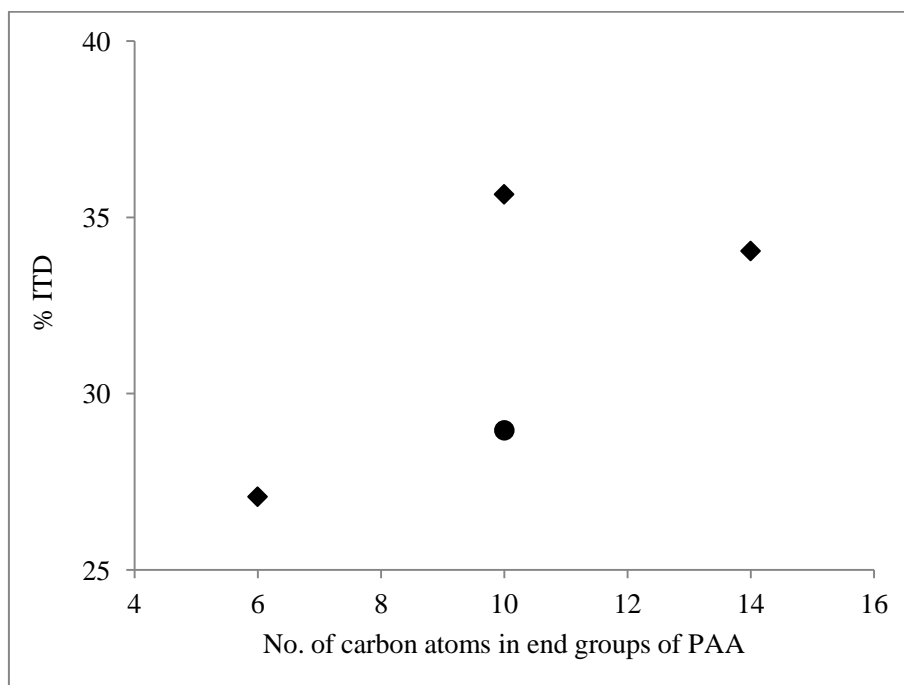
Figure 4.25- % ITD of 40 ppm HCO_3^- at T = 97.2 °C in 50 ppm of NaCl solution and presence of 10 ppm PAA with different end groups (M_n < 2000 g/mol) (● = CIB-PAA)

4.6.3 The mechanism of TD of HCO_3^- by different end groups and molecular mass of PAA

A brief summary for the previous studies in the thermal decomposition of HCO_3^- is given in Table 4.16.

Table 4.16- A brief summary for the previous studies in the thermal decomposition of HCO_3^-

Investigator	Type and concentration of scale inhibitor and T	solution	The study results
Walinsky and Morton (1979)	Flocon 247 as poly maleic acid 10 – 13 ppm at 102 ± 1 °C	Synthetic seawater contain 375 ppm of HCO_3^- 1260 ppm of Mg^{2+} 824 ppm of Ca^{2+} And TDS 35.10 g/kg	TD of HCO_3^- was inhibited by the presence of poly maleic acid. They suggested the retardation of decomposition of HCO_3^- in the presence of scale inhibitor proceeded either by the formation of complex from scale inhibitor and Ca^{2+} and/or Mg^{2+} inhibiting the calcium and magnesium catalysed decomposition of HCO_3^- or by preventing the heterogeneous decomposition of HCO_3^- on scale surface.
Mubarak (1998)	Belgard 2000 as poly maleic acid 10 ppm at 90 °C	Seawater contain Ca^{2+}, Mg^{2+} and HCO_3^-	TD of HCO_3^- was inhibited by the presence of poly maleic acid. This study did not mention the mechanism for the inhibition of thermal decomposition of HCO_3^- by scale inhibitor.
Shams El Din et al (2002)	Three different of polymaleate commercial scale inhibitors 2-10 ppm at 100 °C	4% NaCl solution only contain of 150 ppm of HCO_3^-	TD of HCO_3^- was inhibited by those different of poly maleic acid. Shams El-Din and his workers believed that, the different behavior for the scale inhibitors were due to the difference on the structure, molecular mass and co-polymerization for scale inhibitors.

To suggest a possible mechanism of the inhibition thermal decomposition of HCO_3^- by PAA with different end groups and molecular mass, the following observations are important:

- The lowest molecular mass of HDIB-PAA, which has an active surface property, has the lowest % ITD of HCO_3^-. That behavior is very clear as when the solutions that contains 10 and 15 ppm of this material when boiling, plenty of foam was formed. That foam immediately disappeared when HCO_3^- solution was added; but remained on the addition of similar amounts of NaCl solution.

- The difference in % ITD of HCO_3^- between EIB-PAA, which has 6 carbon atoms in end group as hydrophobic end group, and CMM-PAA which has 4 carbon atoms in end group as hydrophilic end group was equal to 7 %.

- % ITD is inversely-proportional with the molecular mass of PAA as shown in Figure 4.26.

- HIB and DIB have the best % ITD of HCO_3^-.

- All rate coefficients for TD of 40 ppm HCO_3^- increases with the addition of 50 ppm NaCl.

Those observations and other results of ITD of HCO_3^- by PAA with different end groups and molecular mass suggest the mechanism of the inhibition of thermal decomposition of HCO_3^- by PAA with different end groups may be by preventing heterogeneous decomposition of HCO_3^- on interfaces. The interface surfaces such as the water/air interface of bubbles that form in bulk solution are very important in the heterogeneous decomposition of HCO_3^- which may provide the activation energy to decompose HCO_3^- ions lower than that in the bulk solution. Another important interface is the glass/water interface as shown in Figure 4.27. At the end of the experiments there was some PAA adsorbed on that surface which was removed by acid flashing.

The coverage of liquid/gas interfaces by PAAs may increase with decreasing molecular mass of PAA. Theoretically, the concentration of PAA at 10 ppm is approximately same for all PAAs with different end group and molecular mass. However, the number of chains of PAA

increases with decreasing molecular mass, which allow the low molecular mass of PAA to cover a larger fraction of liquid/gas interface than high molecular mass PAA. Another pathway to the effect of the molecular mass of PAA may be the transport of polymer through solution by diffusion, whereas the low molecular mass is faster than the high molecular mass which was proposed previously. Those effects may be making low molecular mass of PAA thermal decomposition more than high molecular mass PAA.
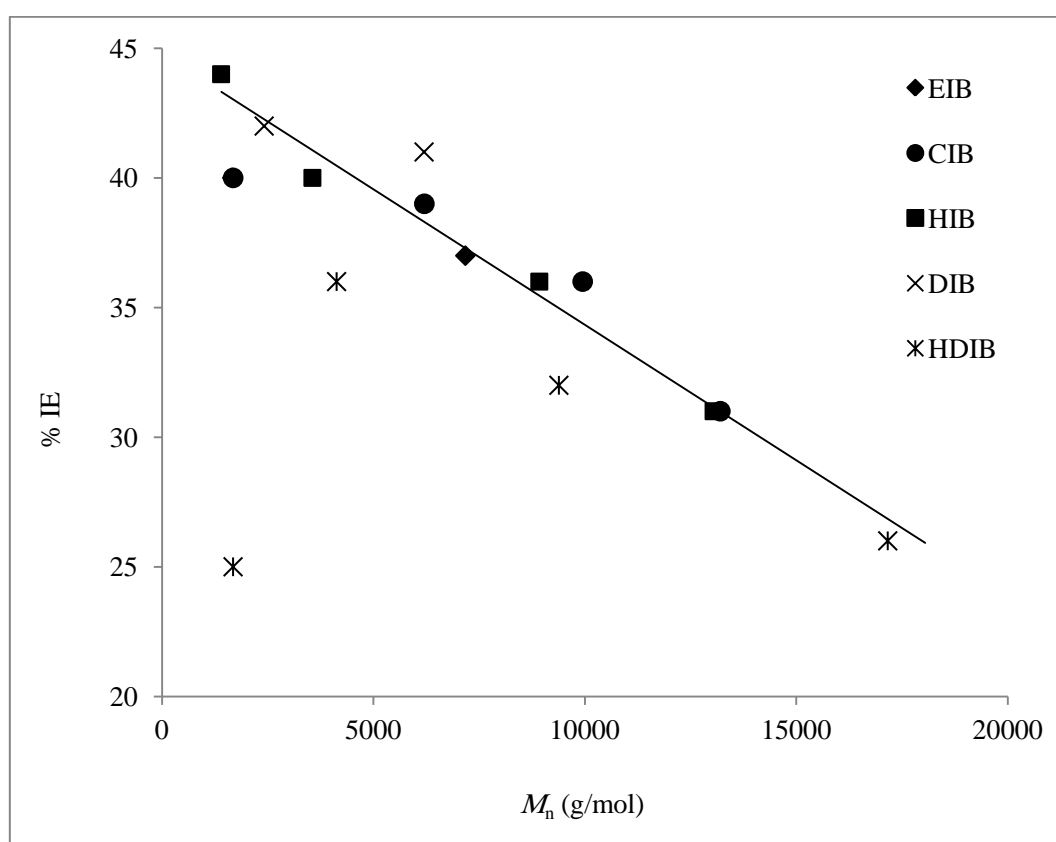
Figure 4.26- Increasing in molecular mass of PAAs decreasing in % ITD

The effect of end groups may appear in two ways. First is in their effect on the transport of PAA (common with molecular mass) in solution which clearly appears in the equivalent conductivity as explained previously. Second is the possible micelle formation, particularly for PAA with the longest end group (HDIB). The lowest molecular mass of HDIB-PAA (at

10 ppm) has the lowest % ITD of HCO_3^- (25 %). Moreover, there was no significant change in % ITD with increasing its concentration to 15 ppm, which may be due to the micelle formation.
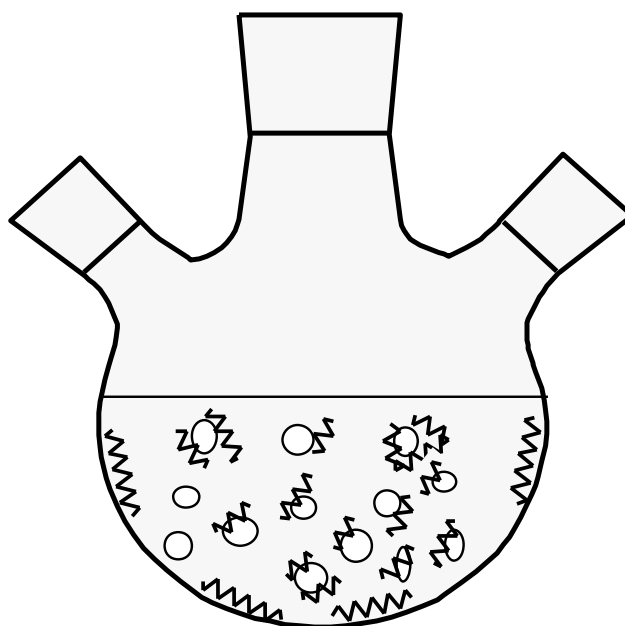
Figure 4.27- The covering of air bubbles by PAAs and the adsorption of PAA on the round bottom flask.

An example of the effect of both end groups and molecular mass of PAA to prevent the heterogenous decomposition of HCO_3^- is PAA with mid-length hydrophobic end groups (CIB & HIB). CIB-PAA (M_n = 9954 g/mol) and HIB-PAA (M_n = 8928 g/mol) have the same % ITD (36%) and very close equivalent conductivities of 5.51×10^{-3} and 5.74×10^{-3} ($S.cm^2/eq$) respectively. CIB-PAA (M_n = 13209 g/mol) and HIB-PAA (M_n = 13049 g/mol) also have the same % ITD (31%) and very close equivalent conductivities of 3.76×10^{-3} and 3.97×10^{-3} ($S.cm^2/eq$) respectively. (Table 4.17)

Table 4.17- the comparison between % ITD and equivalent conductivity for CIB-PAA and HIB-PAA.

End Groups of PAA	M_n	Ratio M_{ne}/M_n	Λ of PA^{n-} (S.cm^2/eq) $\times 10^{-2}$	% ITD
CIB	9954	0.017	0.551	36
	13209	0.013	0.376	31
HIB	8928	0.019	0.574	36
	13049	0.013	0.397	31

4.7 Conclusion

The Pitzer model was used to estimate the activity coefficients of HCO_3^-, CO_3^{2-}, OH^-, Ca^{2+}, Mg^{2+} and CO_2 (aq) at 25 °C and 100 °C and pH = 8.1 and 9.0 under the condition of seawater and brine solution (CF=1.4). The activity coefficients of those ions were used to calculate ΔG of the competitive reactions in both unimolecular mechanism and bimolecular mechanism. The results showed that both mechanisms can appear. At low temperature the bimolecular mechanism is likely to predominate, however at high temperature (T > 80 °C) the unimolecular mechanism is likely to predominate. This is consistent with experimental observations of alkaline scale formation in thermal desalination and strongly suggests that scale formation in thermal desalination plants is under thermodynamic control.

Conductivity measurements were employed to follow the kinetics of thermal decomposition of HCO_3^- by estimate ΔK (µS/cm) under the conditions T= 97.2 ± 0.5 °C, $[HCO_3^-]$ = 6.557×10^{-4} (40 ppm), and in the absence and presence of PAA with different end groups and

molecular mass ([PAA] =10, 15, 30 ppm). The conductivity data showed that the thermal decomposition of HCO_3^- follows first-order kinetics in the absence of PAA. However, it is not apparent whether the thermal decomposition of HCO_3^- is a unimolecular reaction or a bimolecular reaction. ΔG was calculated during experiment then plotted against time for both mechanisms. The results showed that the ΔG for unimolecular mechanism is more negative than ΔG for bimolecular mechanism and hence the reaction is more probable.

In the presence of PAAs, conductivities (ΔK µS/cm) values of thermal decomposition of HCO_3^- were higher than ΔK for blank solution. The reason was the neutralization of carboxylic acid groups in PAA by OH^-. The estimation of conductivity of (PA^{n-}) in units of µS/cm, S.cm²/monomol and S.cm²/eq (equivalent conductivity) at 97.2 °C was carried out by two pathways. First is the estimation of the conductivity of (PA^{n-}) by applying equation 4.47. The second was by regenerating a semi- theoretical conductivity curve for the decomposition of 40 ppm of HCO_3^- as unimolecular mechanism and then comparing with the experimental conductivity curve. The results of equivalent conductivities of PA^{n-} showed that the molecular mass and end groups of PA^{n-} have a significant effect on the equivalent conductivities. The plots of equivalent conductivity versus the ratio of molecular mass of end group to molecular mass of PA^{n-} (M_{en}/M_n) for HDIB-PAA showed a deviation from the linearity that was observed for PAA with other end groups. This may be attributed to the micelles formation.

The inhibition of thermal decomposition of HCO_3^- by 10 ppm of PAA with different end groups and molecular mass showed that both end groups and molecular mass play a significant role. For all end groups of PAA, the rate coefficient of thermal decomposition of 40 ppm HCO_3^- increased with increasing molecular mass, except HDIB-PAA. Equation 4-40 was applied to analyze the conductivity data and determine rate coefficient of the thermal

decomposition of HCO_3^- at 97.2 °C. The result showed that the thermal decomposition of HCO_3^- follows first order kinetics with $k = 3.35 \times 10^{-2}$ min^{-1}.

The mechanism of the inhibition of thermal decomposition of HCO_3^- by PAA with different end groups was suggested. That mechanism was based on the preventing of heterogeneous decomposition of HCO_3^- on the interface surfaces such as the water/air interface of bubbles that form in bulk solution and the interface surface of round bottom flask. The surrounding of bubbles by PAA should increase with decreasing molecular mass and increasing mobility of PAA.

References

1.   Bott, T. R., *Fouling of heat exchangers*. Elsevier.: Amsterdam, 1995.

2.   Langelier, W. F.; Caldwell, D. H.; Lawrence, W. B.; Spaulding, C. H. *J. Ind. Eng. Chem. (Washington, D. C.)* **1950,** 42, 126-30.

3.   Dooly, R.; Glater, J. *Desalination* **1972,** 11, (1), 1-16.

4.   Walinsky, S. W.; Morton, B. J. *Desalination* **1979,** 31, (1-3), 289-298.

5.   Mubarak, A. *Desalination* **1998,** 120, (1-2).

6.   Shams El Din, A. M.; El-Dashan, M. E.; Mohammed, R. A. *Desalination* **2002,** 142, (2), 151-159.

7.   Shams El Din, A. M.; El-Dahshan, M. E.; Mohammed, R. A. *Desalination* **2005,** 177, (1-3), 241-258.

8.   Bolze, J.; Peng, B.; Dingenouts, N.; Panine, P.; Narayanan, T.; Ballauff, M. *Langmuir* **2002,** 18, (22), 8364-8369.

9.   Millero, F.; Huang, F.; Graham, T.; Pierrot, D. *Geochim. Cosmochim. Acta* **2007,** 71, (1), 46-55.

10.   Christov, C.; Moeller, N. *Geochim. Cosmochim. Acta* **2004,** 68, (6), 1309-1331.

11.   Møller, N. *Geochim. Cosmochim. Acta* **1988,** 52, (4), 821-837.

12.   Pitzer, K. S. *Pure & AppI. Chem.* **1986,** 58, (12), 1599-1610.

13.   Neck, V.; Konnecke, T.; Fanghanel, T.; Kim, J. I. *Journal of Solution Chemistry* **1997,** 26, (6), 561-577.

14.   Millero, F.; Pierrot, D. *Aquat. Geochem.* **1998,** 4, 153-199.

15.   He, S.; Morse, J. W. *Geochim. Cosmochim. Acta* **1993,** 57, (15).

16.   Harvie, C. E.; Moeller, N.; Weare, J. H. *Geochim. Cosmochim. Acta* **1984,** 48, (4), 723-51.

17.   Plummer, L. N.; Busenberg, E. *Geochim. Cosmochim. Acta* **1982,** 46, (6), 1011-40.

18.   Pilling, M. J.; Seakins, P. W., *Reaction Kinetics*. Oxford University Press: 1995; p 28.

19.   Belfares, L.; Altaba, S.; Pons, M. N.; Engasser, J. M.; Fick, M. *Bioprocess Engineering* **1993,** 9, (5), 197-204.

20.   Ofir, P. B.-Y.; Govrin-Lippman, R.; Garti, N.; Füredi-Milhofer, R. *Crystal Growth and Design* **2004,** 4, (1), 177-183.

21.   Bordi, F.; Colby, R.; Cametti, C.; De Lorenzo, L.; Gili, T. *J. Phys. Chem. B* **2002,** 106, 6887-6893.

22.   Ebina, S.; Uedaira, H. *Chem. Letters* **1976**, 1015-1018.

CHAPTER FIVE

Inhibition of Heterogeneous Crystallization of Calcium Carbonate and co-precipitation of Calcium Carbonate and Calcium Sulfate

5.1 Introduction

The heterogeneous crystallization on surfaces of scale forming minerals such as $CaCO_3$ and $CaSO_4$ is a very important problem in both major desalination technologies, reverse osmosis (RO) and multi stage flash (MSF). In RO, one of the causes of the decline in productivity of RO system is scale formation on membrane surfaces which cause degradation of the membranes and that not only reduces the production and quality of produce water, but also increases operating expenditure. In MSF, scale formation on heat transfer surfaces leads to reduction in heat exchanger efficiency because of the lower thermal conductivity of scale, and this directly affects the cost of producing water. To control the scaling, scale inhibitors such as organic compounds, organic polymers, and co-polymers were used.

At the present, the evaluation of scale inhibitors in lab depends mainly on two approaches; first, by observing the variation in the conductivity and turbidity of the solution containing scale-forming ions such as calcium ion and sulfate or carbonate ions under supersaturation conduction. Second, monitoring the variation of calcium concentration with time, either by using calcium ion selective electrode with Automatic Titrator or by using spectrometric analytical methods such as Atomic Absorption and Inductive coupled plasma. However, there are some limitations for using these techniques at high temperatures and in high concentration medium (high ionic strength) these approaches are not effective. For instance, turbidity measurements at high temperatures will be limited due to the formation of air bubbles which interfere with those measurements. Ion-selective electrodes need expensive equipment and suffer from the interference of Mg^{2+} and H^+ ions and long laboratory approaches. Another approach for monitoring scaling by direct measurements of heat transfer across the surface was used by Sheikholeslami and Watkinson.[1,2]

The intrinsic exposed core optical fibre sensor (IECOFS) method is superior to these in being more amenable to laboratory use, cheap and portable.[4]

The main goal of this chapter is to apply an optical fibre sensor to the study of the heterogeneous crystallization of $CaCO_3$ and coprecipitation of $CaCO_3$ and $CaSO_4$ over temperature and ionic strength ranges where turbidity and conductivity are ineffective, and to determine the effectiveness of low molecular mass PAA ($M_n < 2000$ g/mol) with different end groups to prevent those scales at 100 and 120 °C respectively.

5.2 Optical fibre system for high temperature

The optical fibre sensor used was a type of IECOFS which is sensitive only for heterogeneous crystallization on the surface.[3, 4] The optical core is usually made from high refractive index material (RI) (*e.g.* fused silica, RI= 1.457) which is surrounded by cladding of low refractive index material (*e.g.* silicone, RI= 1.408).

The refractive index of scale deposit is higher than the refractive index of the optical fibre core (Table 5.1). When the optical fibre core is immersed in supersaturation solution (Figure 5.1) where that medium has a lower refractive index than core material, the exposed optical fibre can be used to monitor the scale deposition on its surface by recording the change in intensity of laser light with time during the experiment (more detail is given in Chapter 1).

The refractive index of calcite and aragonite polymorphs of $CaCO_3$ at $\lambda = 632.9$ nm was calculated by the refractive index expressions of wavelength dependence measured by Tandon (1965).[5] The results were summarized in Table 5.1.

Table 5.1- Refractive index of calcite and aragonite polymorphs of $CaCO_3$ at $\lambda = 632.9$ nm

Compound	Polymorph	RI	
$CaCO_3$	calcite	n_ω	1.653
		n_ε	1.476
	aragonite	n_1	1.576
		n_2	1.684
		n_3	1.619

n_ω and n_ε denote the indices of refraction of uniaxial crystals of calcite with electric vector parallel and perpendicular to trigonal axes respectively.

n_1, n_2 and n_3 correspond to the directions of the electric vector parallel to *c*, *a* and *b* crystallographic axes respectively.[5]
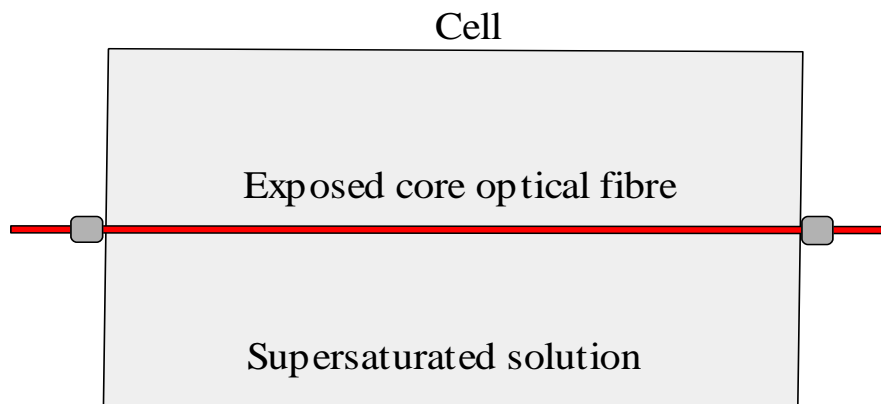
Figure 5.1- Exposed core optical fibre sensor immerse in supersaturated solution

The developed IECOFS sensor for high temperature was constructed with the assistance of Mr. Andrew Wallace of UNE. The system consists of a laser light source 5 mW He-Ne laser (λ = 632.9 nm, Uniphase, CA USA), temperature controller part (Novus-N480D with Thermocouple type J), optical fibre cell and photometric detector (Industrial Fibre optics). The optical fibre cell consists of optical fibre fused silica core of length 21 cm (15 cm immersed in solution) and 1000 μm diameter (F-MBE, Newport Corporation USA and PUV-600T) of refractive index 1.457 and 70 mL cylindrical cell opened on both sides (as heat transfer tube, Figure 5.2) and closed by two special plastic plate both of them contain a small hole to allow the optical fibre to pass through them. That cell is surrounded by an aluminium block which is electrically heated to increase the temperature of solution as shown in Scheme 5.1 and Figure 5.3.

Optical power attenuation *(A)* was calculated using Eq- 5.1

$$A = -10 log \left(\frac{P_t}{P_0} \right)$$
(Eq- 5.1)

Where P_0 and P_t are the intensity of light at initial time (t = 0) and time (t) respectively.

The Inhibition efficiency (% IE) of PAA in reducing the heterogeneous crystallization of $CaCO_3$ on optical fibre surface was determined by applying equation (Eq -5.2)

$$\% IE = \left[1 - \frac{(A_{PAA})}{(A_{Blank})} \right] \times 100$$
(Eq -5.2)

Where A_{PAA} is the attenuation value of steady state in the presence of PAA, A_{Blank} is the attenuation value of steady state in the absence of PAA (blank) under experimental conditions. Thus % IE of PAA at without any heterogeneous crystallization of $CaCO_3$ = 100% and %IE of blank = 0%.
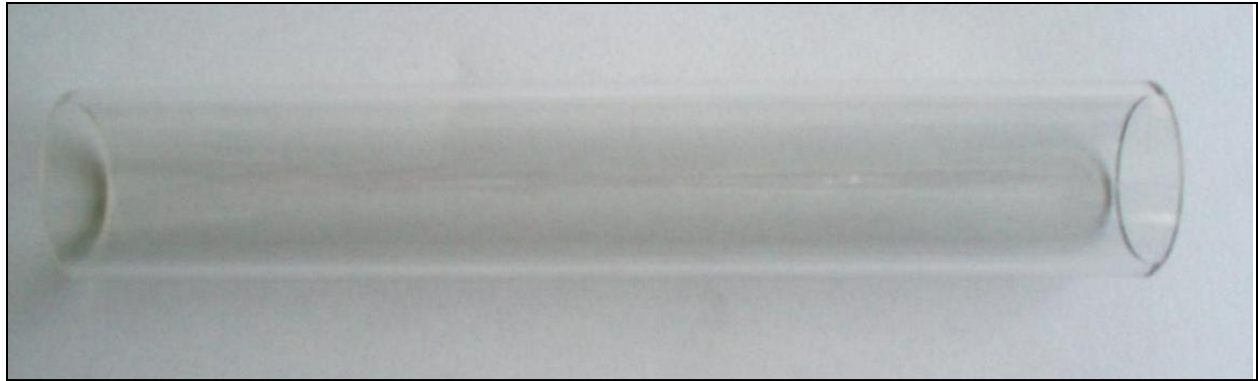
Figure 5.2- Cylindrical cell as heat transfer tube.
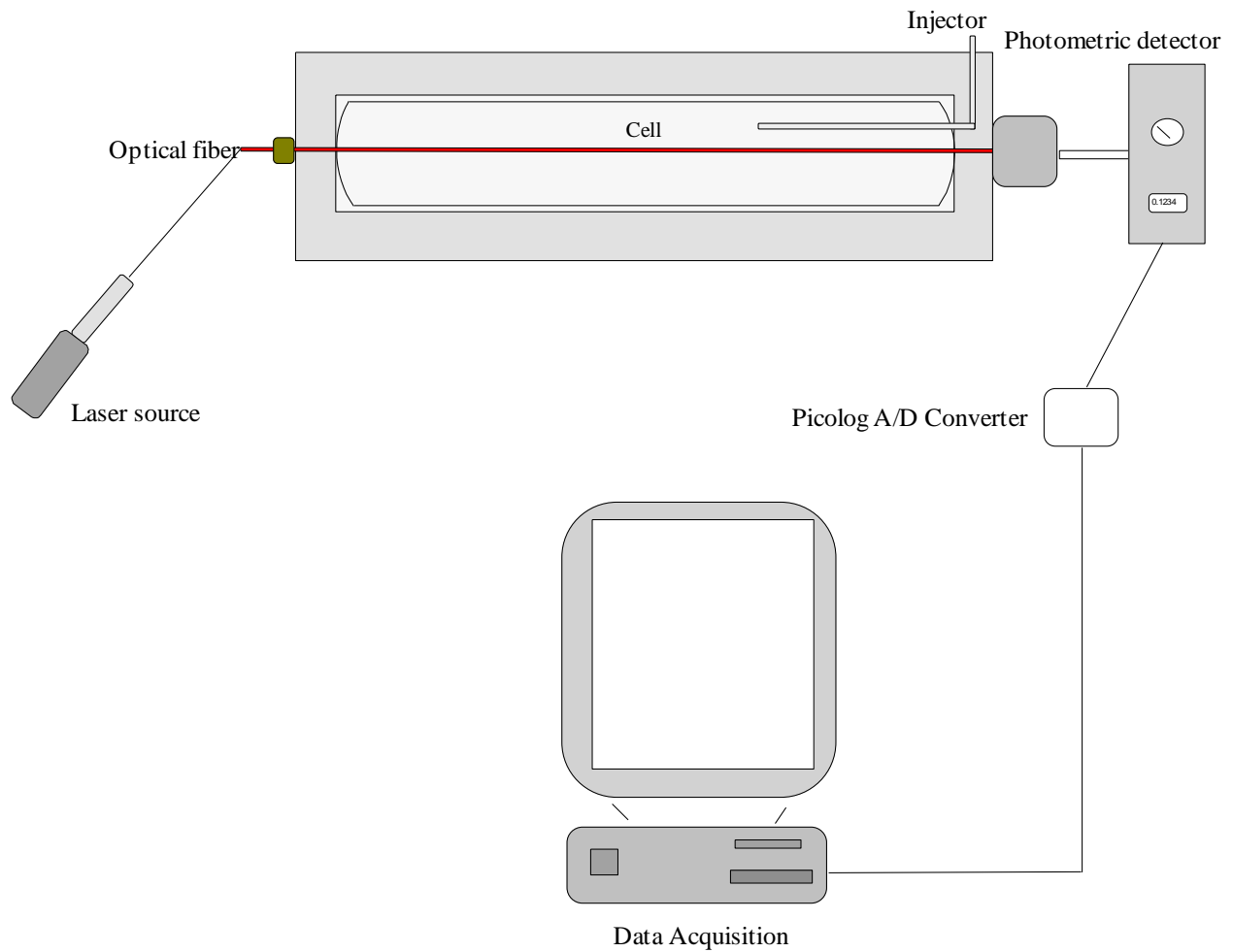
Scheme 5.1- Optical fibre system for high temperature.
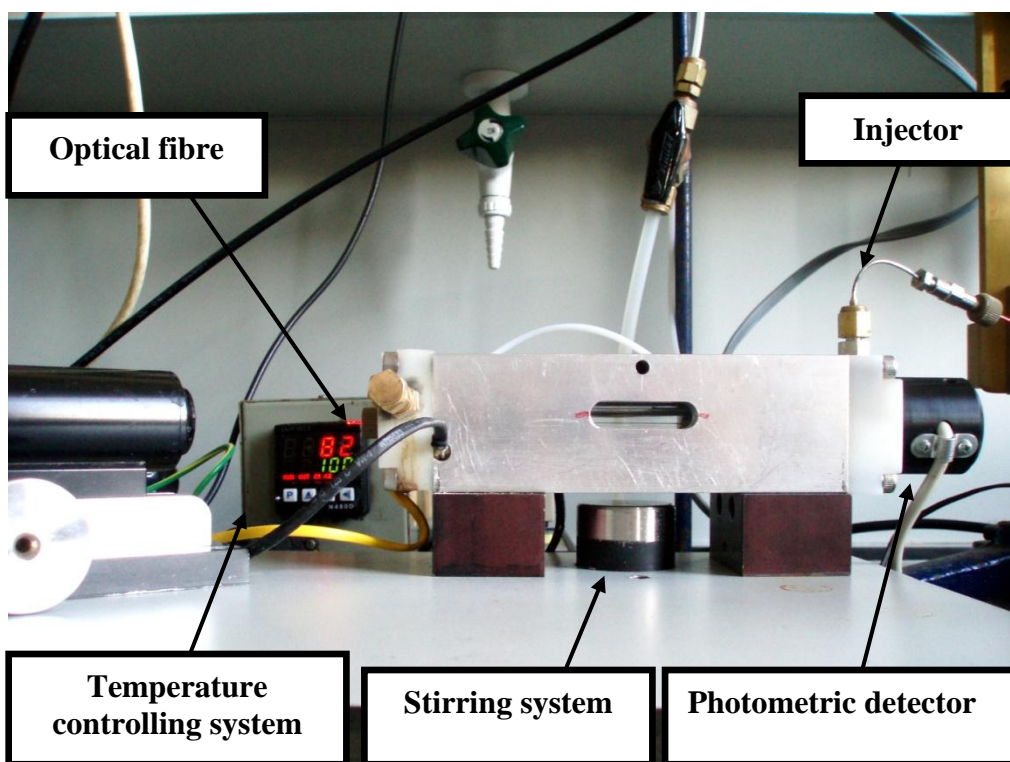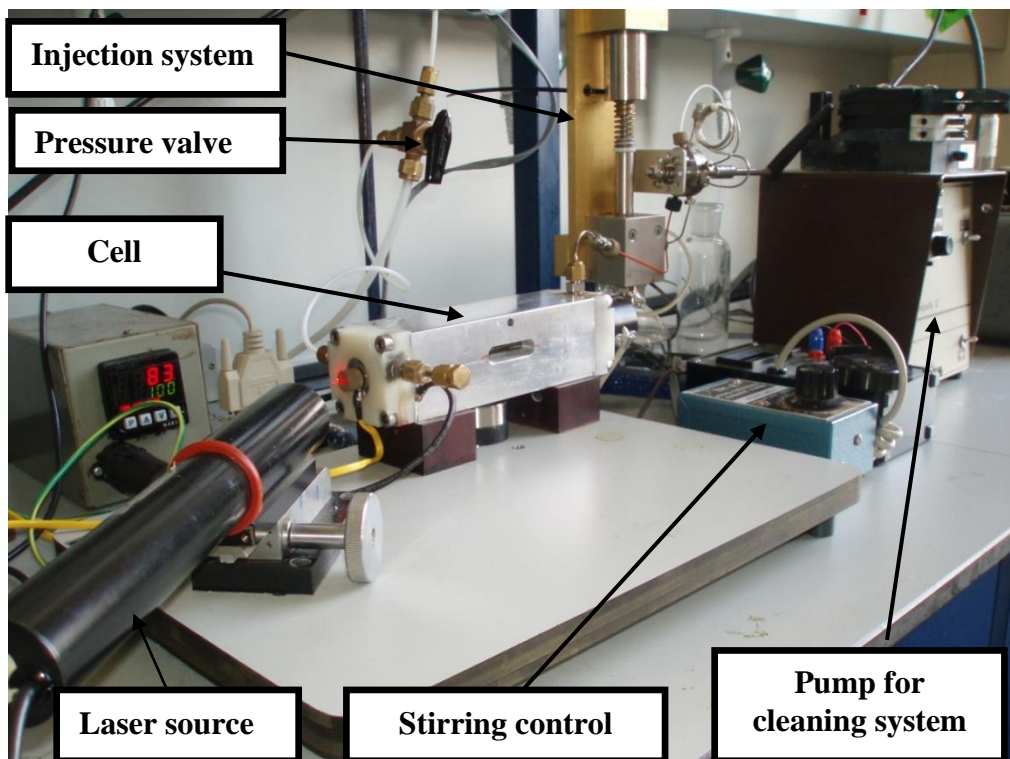
Figure 5.3- Optical fibre system for high temperature.

5.3 The heterogeneous crystallization of $CaCO_3$ on optical fibre surface at 100°C

5.3.1 Experimental

Two solutions, 0.0835 M (5000 ppm) of CO_3^{2-} as Na_2CO_3 and 0.0825 M (3300 ppm) of Ca^{2+} as $CaCl_2$, were prepared. These solutions and the R/O water used were filtered and degassed using a 0.45 μm Millipore solvent filter.

48 mL of deionized water (filtered through 0.45μm cellulose acetate membrane) and one drop of 0.05 M of NaOH to give approximate pH of 9.2 in the absence and presence of 6.70 ppm of PAA were placed in a 70 mL cleaned cylindrical cell (as heat transfer tube open on both sides under magnetic stirring). When the solution reached the target temperature (100 °C), 1 mL of CO_3^{2-} as Na_2CO_3 solution and 1 mL of Ca^{2+} as $CaCl_2$ solution were injected to the cell to give a final concentration of 100 ppm and 66 ppm respectively.

The recording of loss on the laser light density was begun immediately on injection of calcium and carbonate solution and detected by photometric detector over 1000 s. Analogue outputs from photometric detector were digitally converted using a Picolog A/D Converter 16 (16 Bit) and Picolog recording software and data was acquired every 30 seconds.

Optical fibre samples with surface deposit of $CaCO_3$ in absence and presence of PAA ($M_n \leq$ 2000 g/mol) were collected at the end of the experiments (after 1000 s) and characterised by SEM.

Those conditions are the same as conditions 7 for homogeneous crystallization of $CaCO_3$ in Chapter 3. This was done to make a comparison between the efficiency of the lowest molecular

mass of PAA with different end groups to prevent the homogeneous and heterogeneous crystallization of $CaCO_3$. PAA with short hydrophilic (CMM) and hydrophobic (EIB) end groups and middle and long hydrophobic end groups (CIB, HIB and HDIB) were chosen to investigate the effect of the hydrophobicity and size of end groups on the inhibition of the heterogenous formation and the morphology of $CaCO_3$ at elevated temperature.

5.3.2 Results and discussion

Attenuation calculated by Eq. 5.1 of solutions containing 66 ppm of Ca^{2+}, 100 ppm of CO_3^{2-} ions ($Q_{ip}/K_{sp} = 1629$) and in the absence and presence 6.70 ppm of PAA ($M_n \leq 2000$ g/mol) with different end groups at pH = 9.2, t = 1000 s and T = 100 °C was determined in the absence of PAA (blank) and in the presence of PAA as follows

5.3.2.1 In the absence of PAA (blank)

Under those experimental conditions, a linear response of attenuation ($R^2 = 0.995$, n= 18) by optical fibre sensor as IECOFS was obtained in the absence of PAA (Figure 5.4) which is consistent with our previous study for the heterogenous formation of $CaCO_3$ at 25°C (Boerkamp, *et al.*, 2010).[4] That result indicates continuing heterogeneous crystallization on optical fibre surface with an overall attenuation rate of 0.0026 (s^{-1}). The maximum attenuation rate was 0.0048 s^{-1} for the first 30 s of the experiment indicating the depletion of reactants in solution. The attenuation then changed slowly as the system reached a steady state until the end of the experiment as shown in Figure 5.4.
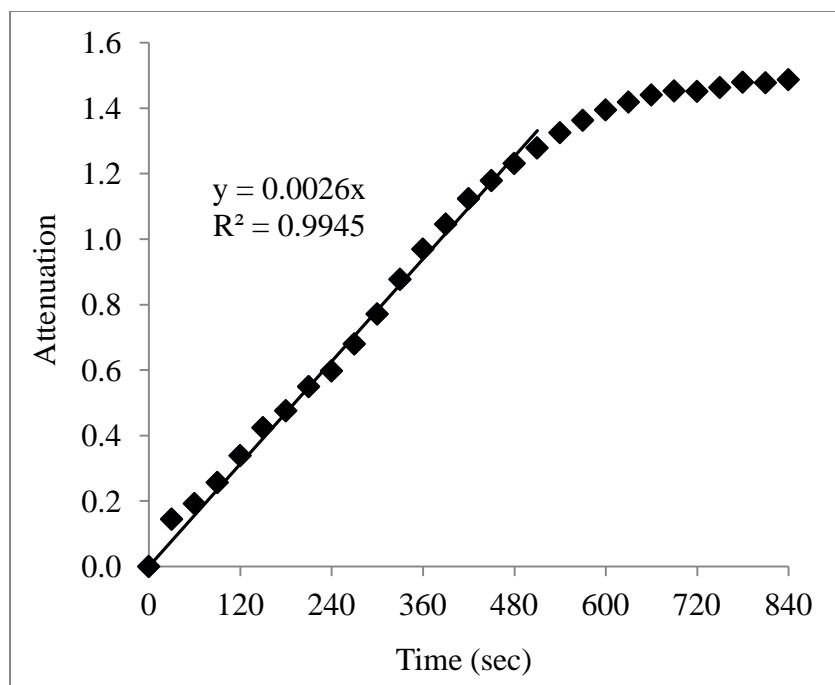
Figure 5.4- Attenuation of intensity laser light in absence of PAA (blank) with progressive calcium carbonate crystallization.

SEM micrograph of the optical fibre surface in the absence of PAAs after 1000 s of crystallization showed that the crystals of $CaCO_3$ occurred primarily as a rod-like morphology (the average length was 8 µm) and some single crystals of rhombohedral calcite as shown in Figure 5.5. Rod-like morphology may consist originally of aragonite polymorph which grows with the longest crystal axis displaying {110} twinning crystal plane.[6]
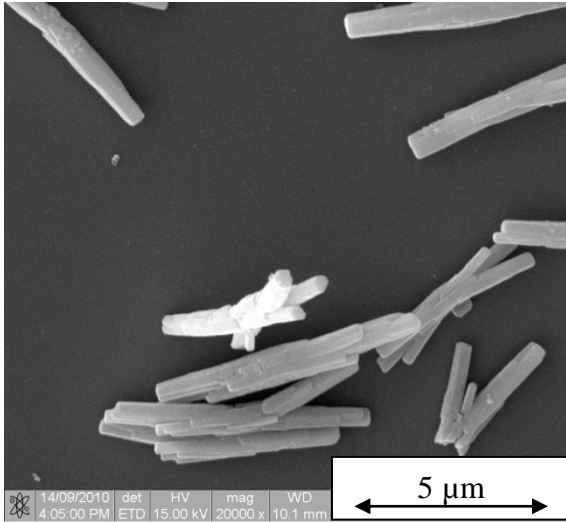
SEM image magnification ($\times$ 20000) showing CaCO$_3$ as rod-like polymorph.
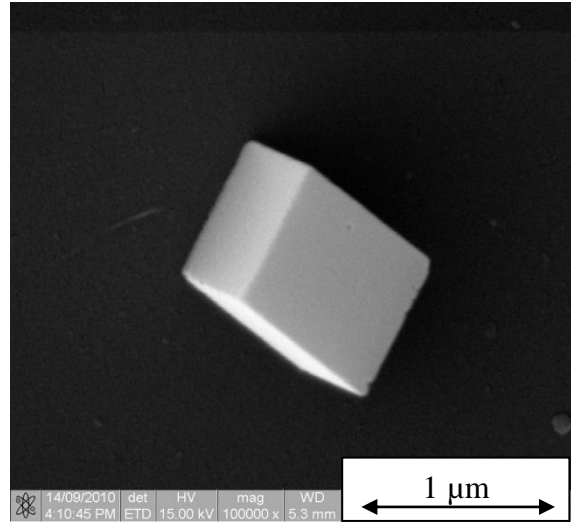
SEM image magnification ($\times$ 100000) showing CaCO$_3$ as rhombohedral calcite polymorph.

Figure 5.5- SEM images of heterogeneous crystallization of CaCO$_3$ on optical fiber surface (diameter 1000 µm) in the absence of PAA (blank) at 100 °C.

5.3.2.2 In the presence of PAA

The observations in regard to the precipitation on the surface of heat transfer tube and the turbidity in bulk solution in the presence of PAA with different end groups in heterogeneous crystallization of CaCO$_3$ system are summarized in Table 5.2.

Table 5.2- Observations for heterogeneous crystallization of $CaCO_3$ at 100 °C.

End groups of PAA	No. of carbon atoms in end group of PAA	The precipitation on heat transfer tube	Turbidity in bulk solution
Blank	0	high	high
CMM	4	low	low
EIB	6	low	low
CIB	10	low	low
HIB	10	nil	nil
HDIB	20	nil	medium

The results of attenuation of IECOFS sensor in the presence of PAA with different end groups and their % IE that was calculated by Eq -5.2 can be discussed as follows

For the lowest molecular mass of PAA with hydrophilic end group (CMM) and short (EIB) and middle (CIB) hydrophobic end group, significant changes in attenuation of IECOFS was obtained during the experiments and % IE was more than 55 %. Those results indicate that the heterogenous nucleation of $CaCO_3$ or settled scale (loose material generated by homogeneous crystallization and precipitated on the surfaces) could be formed on optical fibre surface. However, there is no way of distinguishing these two types of scale formation from IECOFS measurements alone.

In contrast tothe linear response of attenuation of IECOFS that was obtained in the absence of PAA, the response of IECOFS in the presence of PAA with those end groups was a curve with steady state as a final stage as shown in Figure 5.6. The attenuation response of IECOFS in the presence of PAA with short-length hydrophobic end group (EIB, 6 C) and PAA with middle-length hydrophobic end group (CIB, 10C) showed a significant reduction in initial attenuation rate (0.001 and 0.000 s^{-1}) and in overall of % IE (64 and 68 respectively as shown in Figure 5.7).

The attenuation result of IECOFS in the presence of PAA with hydrophilic end group (CMM-PAA) showed a eduction in initial attenuation rate to half (0.0022 s^{-1}) in comparison with attenuation result for blank for the same period. After that period, however, the attenuation in the presence of CMM-PAA became more than the attenuation of bthe lank for the next 150 s, and finally the change in attenuation was very slow over the steady state period as shown in Figure 5.6.
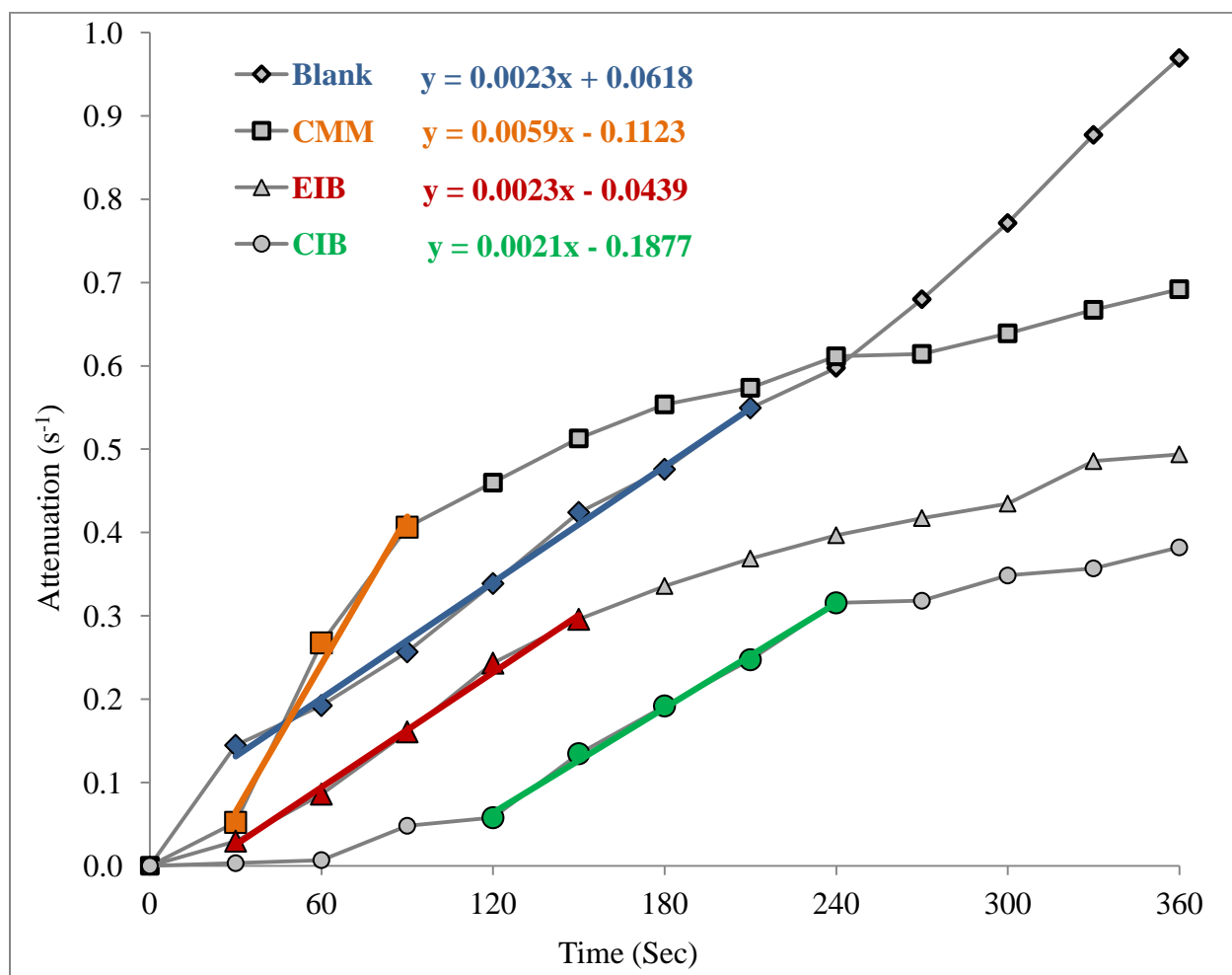
Figure 5.6- Attenuation of intensity laser light with and without of PAA ($M_n \leq 2000$ g/mol) with different end groups.
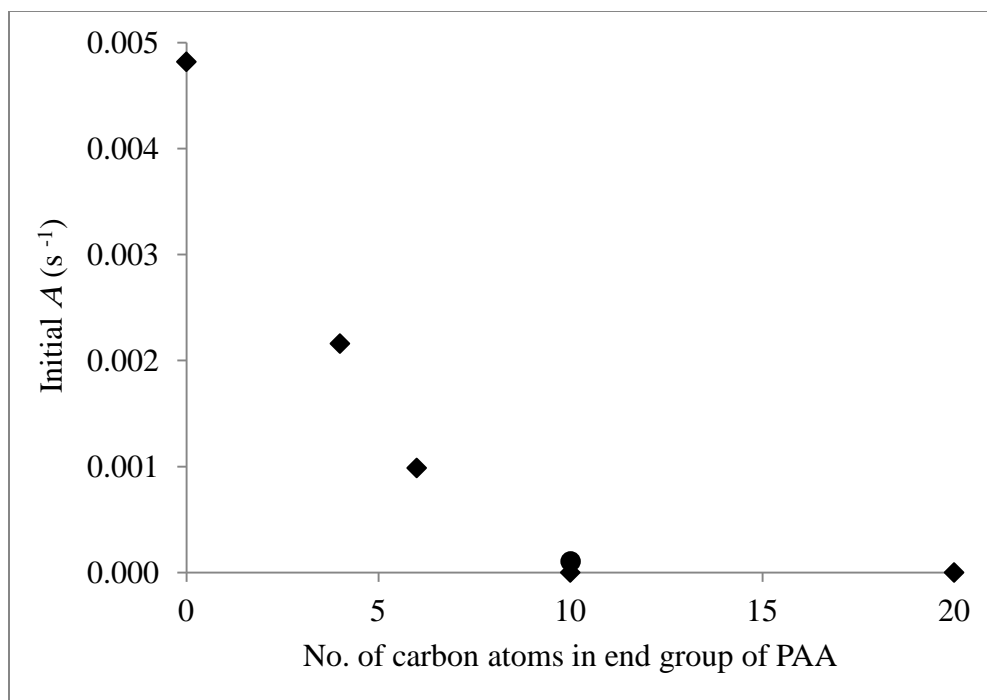
Figure 5.7- Initial attenuation rate of PAA with different end group for heterogeneous

crystallization of $CaCO_3$ on optical fibre surface.

The heterogenous crystallization of $CaCO_3$ on optical fibre surface in the presence of CMM-PAA, EIB-PAA and CIB-PAA can be characterized by three stages (Figure 5.8) as follows:

Stage 1 was the initial attenuation rate (first 30 s of the experiment) where the attenuation rate was inhibited in the presence of PAA with short hydrophilic (CMM) and hydrophobic (EIB) end groups. However, in the presence of PAA with middle hydrophobic end group (CIB), the formation of $CaCO_3$ in optical fibre surface did not begin until after 60 s induction time.

Stage 2 was the maximum attenuation rate (0.0059, 0.0023 and $0.0021s^{-1}$) that was obtained in the presence of CMM-PAA, EIB-PAA and CIB-PAA respectively. In this stage, there was no significant different in attenuation rate between in the absence (blank, $A = 0.0023$ s^{-1}) and presence of PAA with hydrophobic end groups (EIB and CIB). However, the attenuation rate in

the presence of PAA with hydrophilic end group (0.0059 s^{-1}) was higher than the blank as shown in Table 5.3 and Figure 5.9.

Stage 3 was the steady state period where the attenuation rate value for all of PAA with those end groups was less than the attenuation rate of blank.
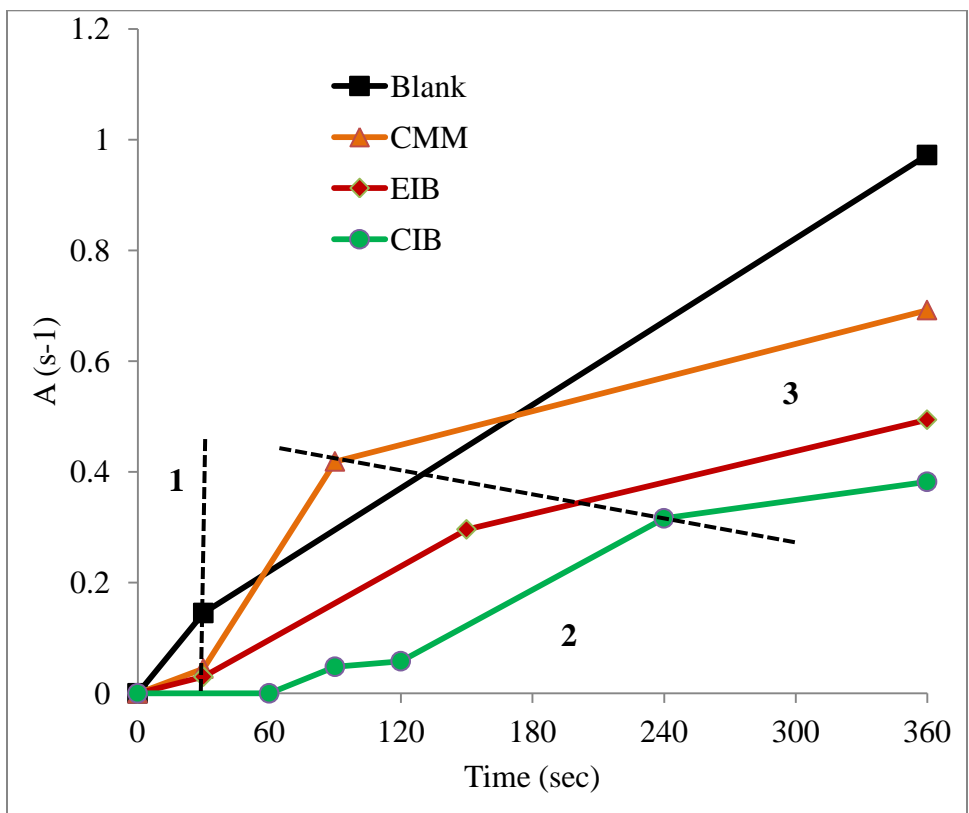
Figure 5.8- The stages for heterogenous crystallization of $CaCO_3$ in optical fibre surface in the presence of CMM-PAA, EIB-PAA and CIB-PAA.

Table 5.3- Initial and maximum attenuation rate of heterogeneous crystallization of $CaCO_3$ on optical fibre surface in the presence of PAAs.

End Groups terminated-PAA		No. of C in end group of PAA	M_n	Induction time (IT) (s)	Initial A rate (s^{-1}) (stage 1)	maximum A rate (s^{-1}) (stage 2)
Blank		0	-	0	0.0048	0.0023 ± 0.0003
CMM		4	2106	0	0.0022	0.0059 ± 0.0022
Hydrophobic End Groups	EIB	6	1669	0	0.0010	0.0023 ± 0.0006
	CIB	10	1689	60	0	0.0021 ± 0.0016
	HIB	10	1403	No IT	0	0
	HDIB	20	1687	No IT	0	0
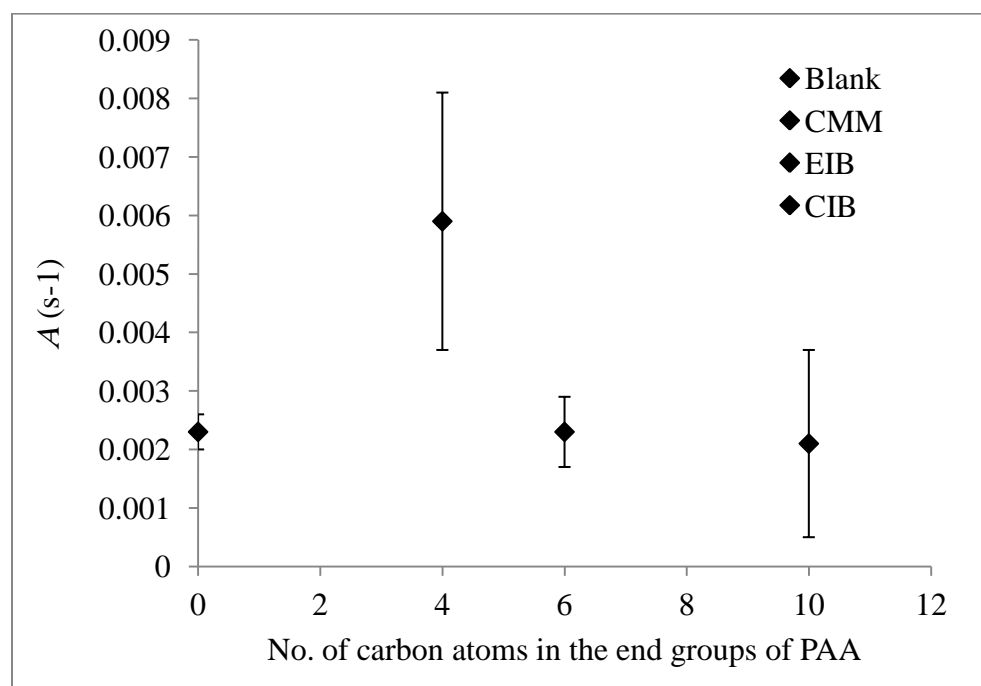
Figure 5.9- Maximum attenuation rate of heterogeneous crystallization of $CaCO_3$ on optical fibre surface in the presence of PAAs.

SEM images in the presence of PAA with mid-length hydrophobic end group (CIB) showed crystals of $CaCO_3$ present in vaterite flower polymorph as shown in Figure 5.10. The vaterite metastable polymorph forms first as the kinetically-favoured product and can be stabilized kinetically by the adsorbing of additives such as scale inhibitors (PAA) on its active growth faces to retard and prevent the phase transformation into aragonite and calcite.[7-9] Vaterite crystals may have six active surfaces, four of them terminated with calcium atoms (positive charge) and they will be strongly inhibited by PAA as was explained in Chapter 3. The images with CIB-PAA illustrated the highest distortion in vaterite flower polymorph which may be due to the strong adsorption of CIB-PAA on all active faces of the growing $CaCO_3$ nucleus.

In the presence of PAA with short-length hydrophobic end-group (EIB), crystals of $CaCO_3$ occurred primarily as a mixture of distorted vaterite florettes with a few rod-like crystals and trace of rhombohedral calcite as shown in Figure 5.11. However, the SEM micrograph of $CaCO_3$ crystals obtained in the presence of PAA with hydrophilic end group (CMM) showed a distorted rhombohedral calcite as shown in Figure 5.12. The distortion in rhombohedral calcite may be due to the adsorption of CMM-PAA on the positive charge face $\{1\bar{1}0\}$ which is the fastest growing face in the crystal of rhombohedral calcite and neutral face $\{104\}$.[10]

PAA with hydrophobic end groups can affect both nucleation and crystal growth and stabilizes the vaterite polymorph. However, PAA with hydrophilic ends can apparently only affect the crystal growth stage which may be because the hydrophobic end groups discourage the PAA chains from desorbing from the nuclei of $CaCO_3$ as fast as PAA with hydrophilic end groups, delaying the growth of the $CaCO_3$ nuclei.

With increasing hydrophobicity by increasing the length of end groups of PAA, the amount of the less thermodynamically stable vaterite polymorph (which is formed first) increases. probably for the same reason maintained above, as shown in Scheme 5.2.

| End group | increasing in hydrophobicity | | | |
	blank	CMM	EIB	CIB
polymorph	Rod-like (mainly hexagonal calcite)	rhombohedral calcite	Vaterite, rod-like and rhombohedral calcite	All vaterite

Scheme 5.2- The relationship between the hydrophobicity of PAA end groups and predominate of CaCO$_3$ polymorph
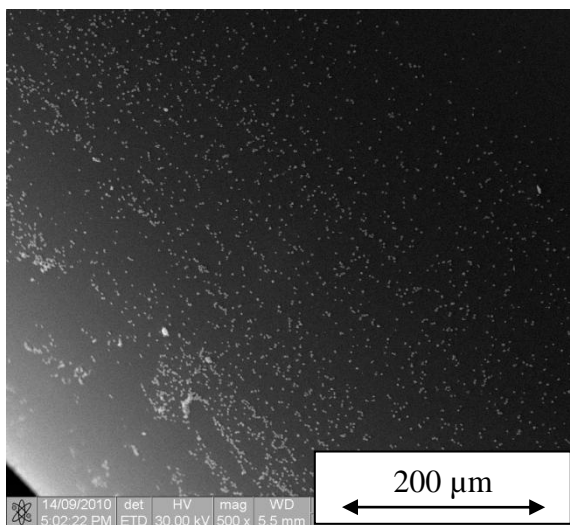
A
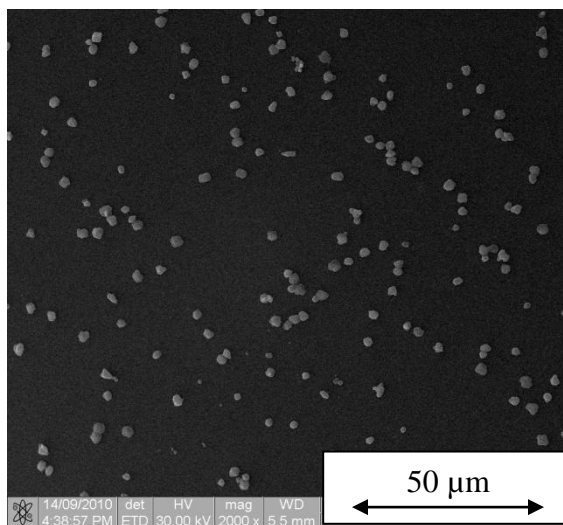
B

SEM images A ($\times$ 500) and B ($\times$ 2000) showing CaCO$_3$ crystals on a section of an exposed fibre

core (diameter 1000 µm)
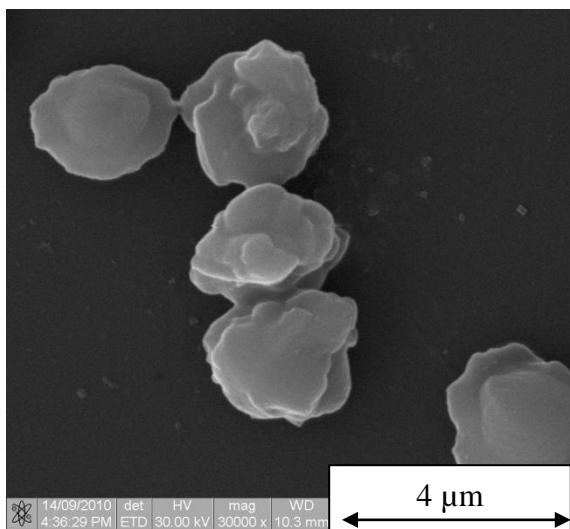
C
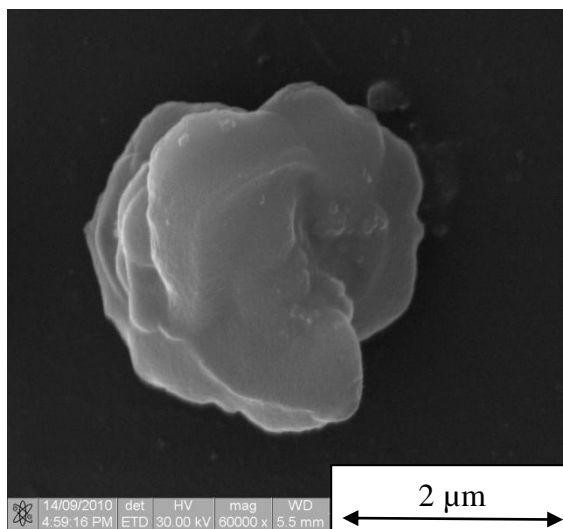
D

SEM images C ($\times$ 30000) and D ($\times$ 60000) for the highest distortion of single crystals of vaterite

flower polymorph

Figure 5.10- SEM images of heterogeneous crystallization of CaCO$_3$ on optical fibre core in the

presence CIB-PAA at 100 °C.
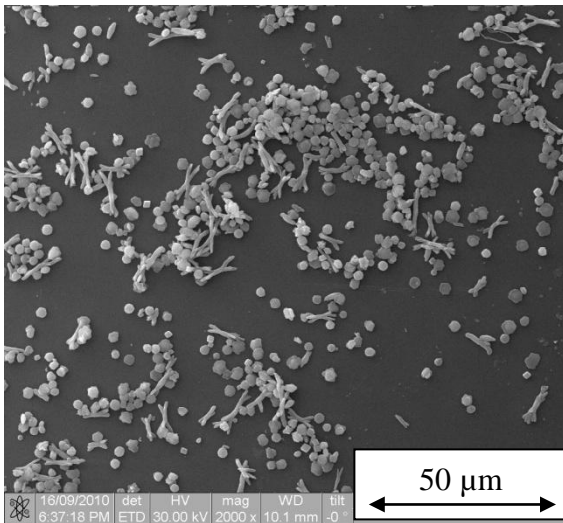
A
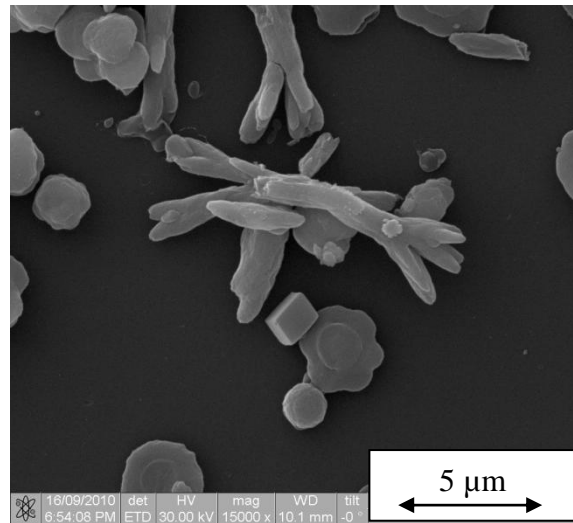
B

SEM images A ($\times$ 2000) and B ($\times$ 15000) showing a mixture of three polymorphs of $CaCO_3$

(vaterite, rod-like and rhombohedral calcite)
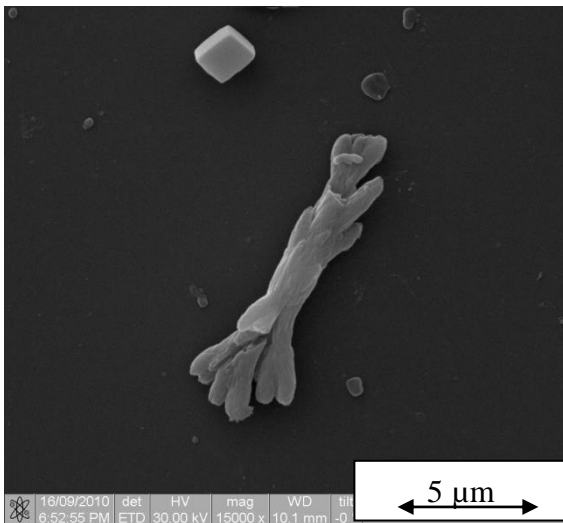
SEM image ($\times$ 15000) of rod-like and

rhombohedral calcite polymorphs
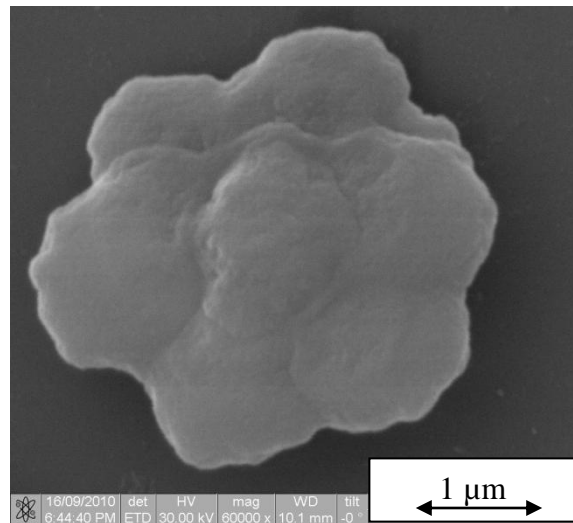
SEM micrograph ($\times$ 60000) showing distorted

vaterite polymorph

Figure 5.11- SEM images of heterogeneous crystallization of $CaCO_3$ on optical fibre core

(diameter 1000 µm) in the presence of EIB-PAA at 100 °C.
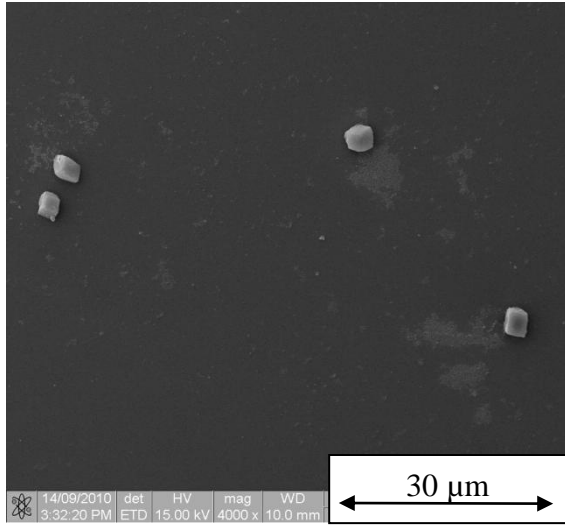
SEM image ($\times$ 4000) showing CaCO$_3$ crystals   SEM image ($\times$ 50000) showing distorted
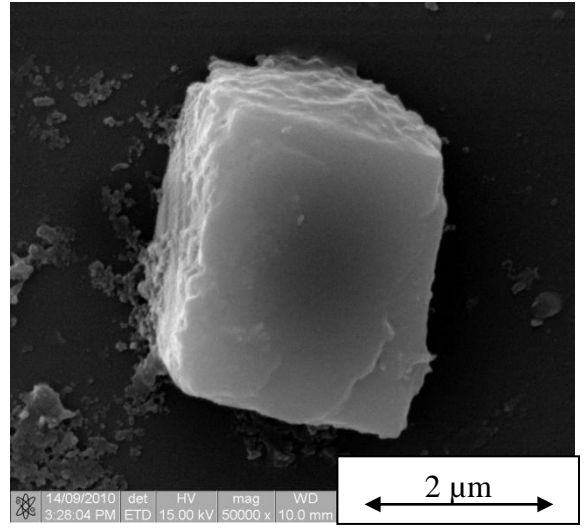
as rhombohedral calcite polymorph   rhombohedral calcite polymorph

Figure 5.12- SEM images of heterogeneous crystallization of CaCO$_3$ on optical fibre core

(diameter 1000 µm) in the presence of CMM-PAA at 100 °C

PAA with HIB and HDIB hydrophobic end groups no significant change in attenuation of IECOFS was obtained during experiments. Those results indicate no heterogeneous crystallization of CaCO$_3$ or deposition of settled scale on optical fibre surface. Those results were reinforced by the SEM micrographs for optical fibre core samples in the presence of HIB-PAA and HDIB-PAA which were clean and agree well with attenuation results as shown by SEM image in Figure 5.13.

Although there was plenty of homogeneous crystallization of CaCO$_3$ in the bulk solution in the presence of HDIB-PAA, the surface of the optical fibre and heat transfer tube were clean, with good evidence that the response of IECOFS was only for the heterogeneous crystallization.[3, 4]

The significant difference in the efficiency of HDIB-PAA to inhibit $CaCO_3$ in both homogeneous crystallization in the bulk solution and heterogeneous crystallization on surface can be explained by the high surface activity of HDIB-PAA. This phenomenon is very clear when the solutions that contain 10 and 15 ppm of this material on boiling, plenty of foam was formed which was proposed in Chapter 4.

This result is very interesting due to the fact that HDIB-PAA may work as surfactant or dispersant more than as scale inhibitor. The suggested mechanism for inhibition of heterogeneous crystallization of $CaCO_3$ by HDIB-PAA is by the formation of micelles that can act as foci for nucleation in the bulk, or maybe it can stabilise dispersed particles and increase their affinity for calcium.

The hydrophobic end groups play a very important role in that mechanism. The surface activity and dispersant properties of PAA increase with increasing number of carbon atoms in the end group of PAA in the same way as the hydrophobicity increases. The initial attenuation rate significantly decreases (comparing with blank) with increasing number of carbon atoms in end group of PAA. As the experiment was continued however, the attenuation rate in Stage 2 increased only for PAA with short (CMM and EIB) and middle end groups.
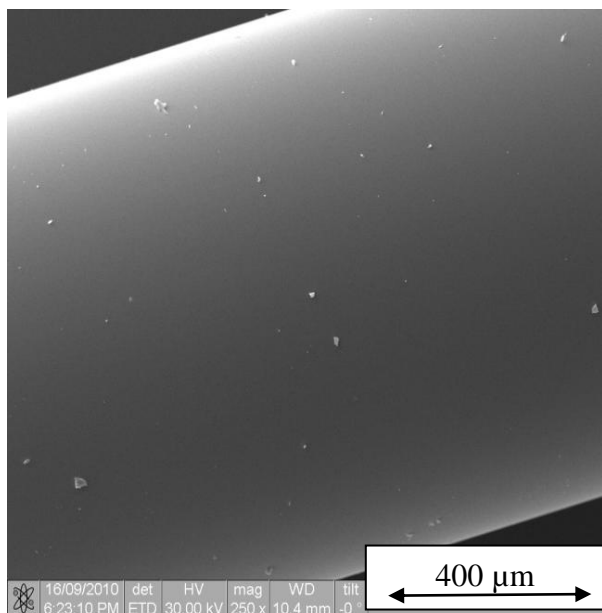
| SEM image magnification ($\times$ 250) showing a clean section of exposed optical fibre core in the presence of HIB-PAA | SEM image magnification ($\times$ 200) showing a clean section of exposed optical fibre core in the presence of and HDIB-PAA |
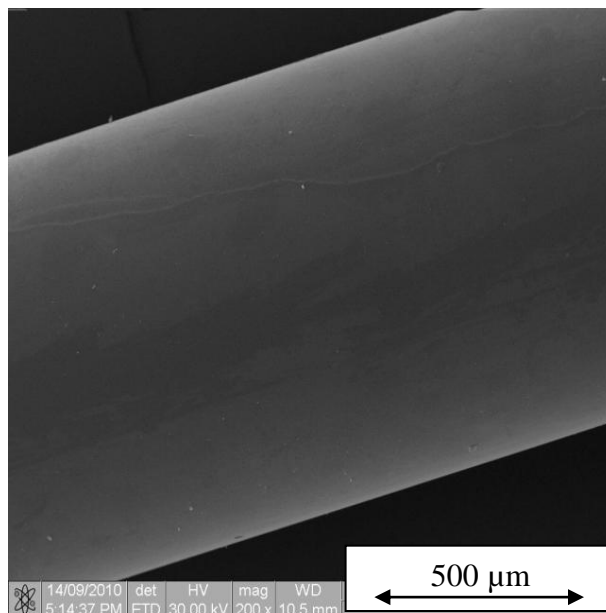
Figure 5.13- SEM images of exposed optical fibre core (diameter 1000 µm) at 100 °C

Energy dispersive X-ray spectroscopy (EDS) of the light spots in the SEM images (Figure 5.13) found only Si and O as shown in Figure 5.14, suggesting they are silica artifacts of sample preparation.

Note: The EDX spectra showed that the sample was an iron-rich spot, and might have been a fleck of rust collected in sample preparation particularly at coating stage.
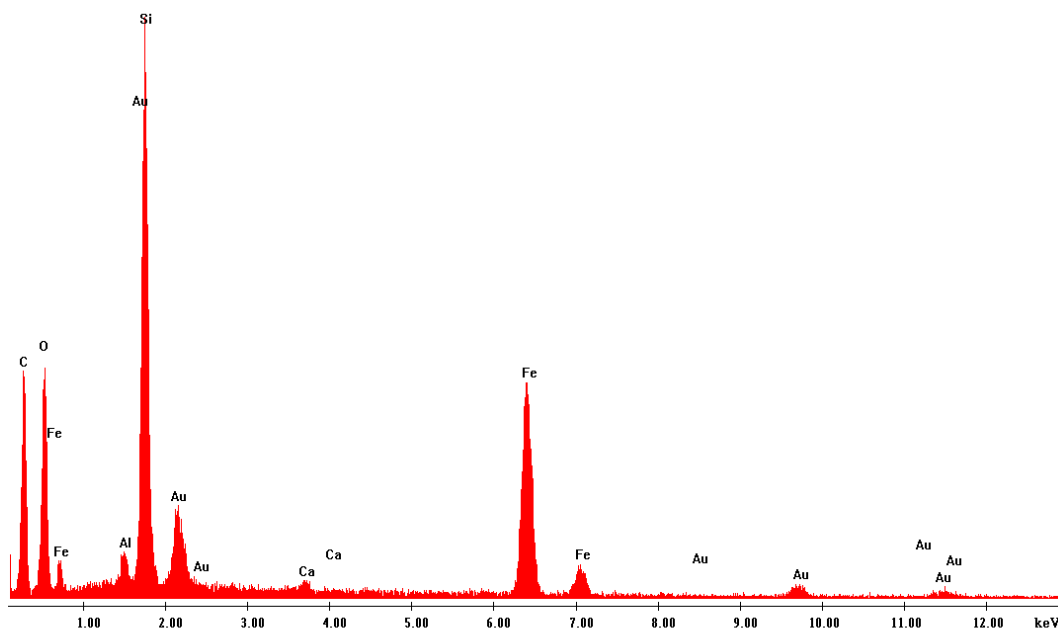
Figure 5.14- Energy dispersive X-ray spectroscopy result to determine the main elements in small parts that appear on the optical fibre surface in Figures 5.14.

The inhibition efficiency of PAA with different end groups to prevent heterogeneous crystallization of $CaCO_3$ in order of decreasing % IE was HIB-PAA > CIB-PAA > EIB-PAA > CMM-PAA, which was of the same order for homogeneous crystallization in bulk solution proposed in Chapter 3 (Table 5.4). The inhibition efficiency of HDIB-PAA, however; is significantly different in having % IE 100 and 45 for heterogeneous and homogeneous crystallization of $CaCO_3$ respectively. The different values of % IE for homogeneous crystallization (HMC) and heterogeneous crystallization (HTC) of $CaCO_3$ for the same PAA may be due to the different impact of PAA on the different mechanisms. The predominant mechanism for the inhibition of $CaCO_3$ formation in bulk solution may be by the adsorption of PAA on the active face of $CaCO_3$ crystals. However, in the HTC it may be by the stabilisation of dispersed particles and increase in their affinity for calcium.

Table 5.4- The inhibition efficiency of PAA with different end groups to prevent homogenous and heterogeneous crystallization of $CaCO_3$.

End Groups terminated-PAA		No. of C in end group of PAA	M_n	% IE for HTC of $CaCO_3$	% IE for HMC of $CaCO_3$
Blank		0	-	0.0	0.0
CMM		4	2106	55.9	65.9
Hydrophobic End Groups	EIB	6	1669	64.0	75.0
	CIB	10	1689	67.9	93.0
	HIB	10	1403	100.0	100.0
	HDIB	20	1687	100.0	45.5

5.4 Heterogeneous coprecipitation of CaCO$_3$ and CaSO$_4$ on optical fiber surface at 120 °C

Three solutions, 0.5 M (48000 ppm) of SO$_4^{2-}$ as Na$_2$SO$_4$, 0.0625 M (3750 ppm) of CO$_3^{2-}$ as Na$_2$CO$_3$ and 0.15 M (6000 ppm) of Ca^{2+} as CaCl$_2$, were prepared. These solutions and the R/O water used were filtered and degassed using a 0.45 μm Millipore solvent filter.

5.4.1 Experimental

48 mL of deionized water (0.45μm cellulose acetate membrane containing SO$_4^{2-}$ as Na$_2$SO$_4$ to give a final concentration of 5760 ppm in the absence and presence of 10 ppm of PAA was placed in a 70 mL cleaned cell under magnetic stirring. When the solution reached the target temperature (120 °C), 1 ml of CO$_3^{2-}$ as Na$_2$CO$_3$ solution and 1 ml of Ca^{2+} as CaCl$_2$ solution were added to the cell to give a final concentration of 75 ppm and 120 ppm respectively (Q_{ip} /K_{sp} (CaCO$_3$) = 2752).

The recording of loss on the laser light density was begun immediately on injection and detected by photometric detector over 3000 s. Analogue outputs from photometric detector were digitally converted using a Picolog A/D Converter 16 (16 Bit) and Picolog recording software and data was acquired every 5 seconds.

Optical fibre samples containing deposits of CaCO$_3$ and CaSO$_4$ formed in the absence and presence of PAA ($M_n \leq 2000$ g/mol) were collected at the end of experiment (after 50 min) then characterized by SEM.

5.4.2 Results and discussion

Attenuation of solutions containing 5760 of SO_4^{2-} as Na_2SO_4, 75 ppm of CO_3^{2-} as Na_2CO_3 and 120 ppm of Ca^{2+} as $CaCl_2$, and in the absence and presence 10 ppm of PAA ($M_n \leq 2000$ g/mol) with different end groups at pH = 9.0, t = 50 min and T = 120 °C was determined in the absence of PAA (blank) and in the presence of PAA as follows

5.4.2.1 In the absence of PAA (blank)

A linear response of attenuation ($R^2 = 0.980$, n = 52) by optical fibre sensor as IECOFS was obtained in the absence of PAA for the period of (0 − 260 s) as shown in Figure 5.15. In that period, the overall attenuation rate was 0.0039 ± 0.0004 s^{-1} indicating continuous heterogeneous crystallization on the optical fibre surface. After that period, the change in attenuation was slow ($A = 0.0010$ t + 0.7266 s^{-1}) until 465 s (Figure 5.15) then the system reached the steady state until the end of experiment. At the end of experiment, there was a large amount of precipitation on the surface of heat transfer tubes as shown in Figure 5.16 for three different experiments (Figure 5.17). This was largely loose material which was presumably generated by homogeneous crystallization and precipitated on the surfaces (settled scale).

Under the same experimental conditions, the change in attenuation for single heterogeneous precipitation of $CaSO_4$ was very slow, even though precipitation was observed in the bulk solution.[*] This indicates that the kinetics of heterogeneous deposition of $CaSO_4$ is very slow or that it is weakly adherent on the optical fibre surface. Therefore, the predominant deposits in the first period (0 − 260 s) of the heterogeneous coprecipitation of $CaCO_3$ and $CaSO_4$ may be $CaCO_3$ which is faster and stronger adherent than $CaSO_4$ deposits. In heterogeneous coprecipitation,

CaCO$_3$ was formed first then it bonded the CaSO$_4$ deposit layer with optical fibre surface as was proposed to occur on a heated stainless steel surface by Bramson *et al*., (1996).[11]
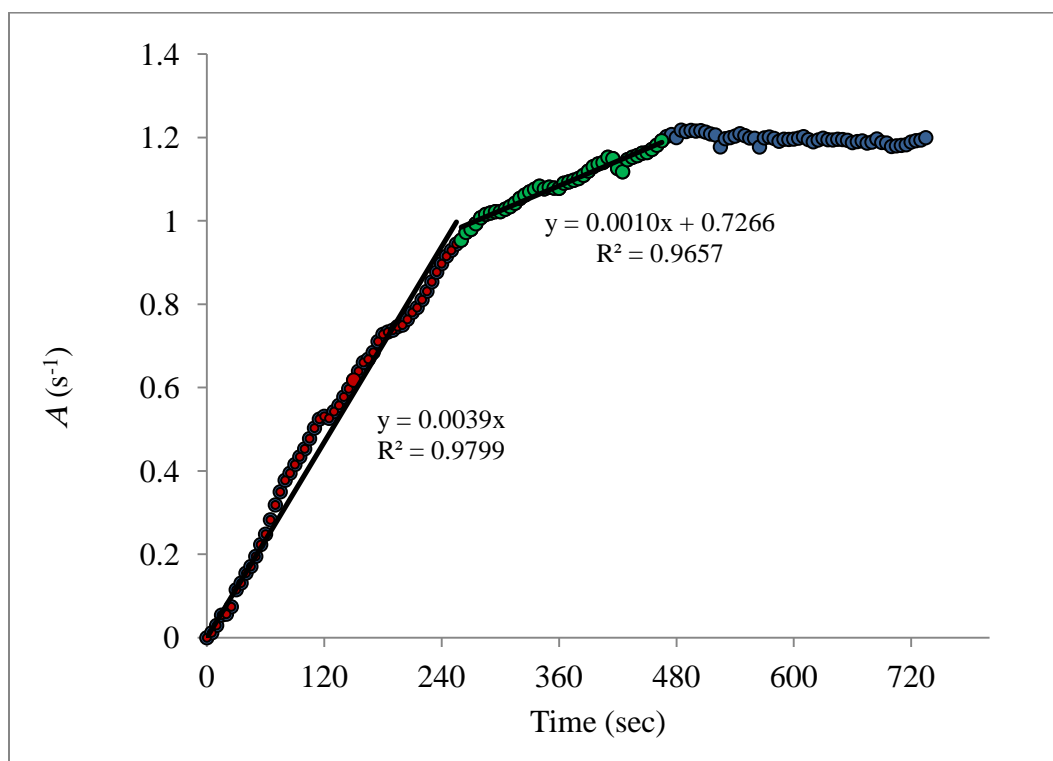
Figure 5.15- Attenuation of intensity laser light in absence of PAA (blank) with progressive co-calcium carbonate and calcium sulphate crystallization.

Figure 5.16- The precipitation on the surface of heat transfer tubes in the absence of PAA (blank)
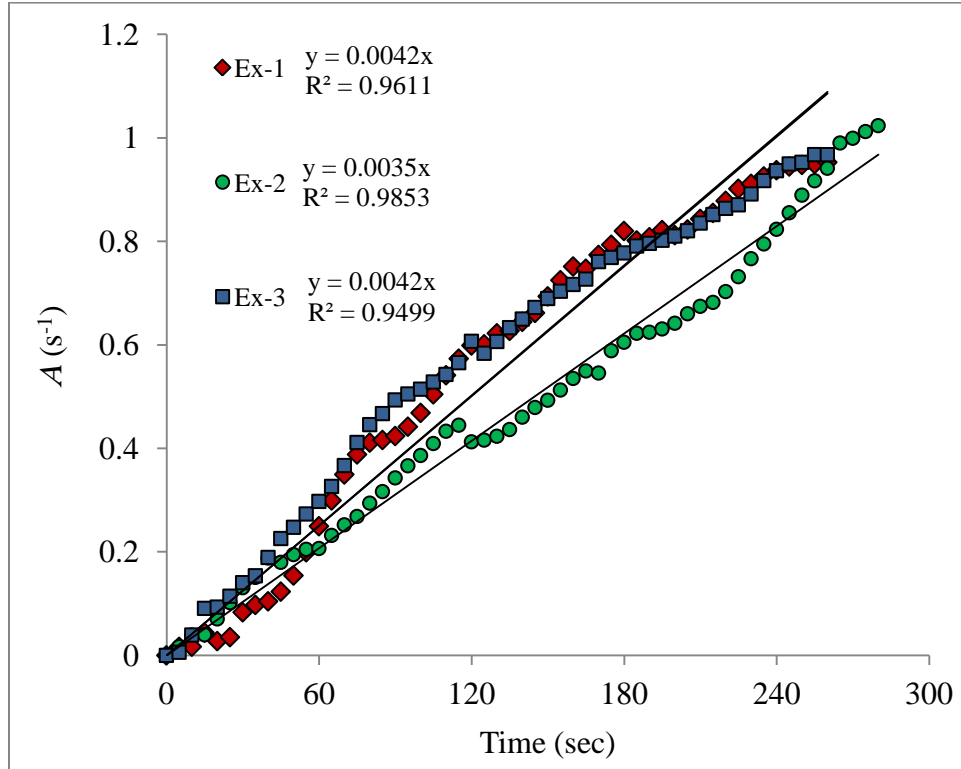
for calcium carbonate and calcium sulfate coprecipitation.

Figure 5.17- Attenuation of three different experiments for calcium carbonate and calcium

sulfate coprecipitation at 120 °C.

SEM micrographs of the optical fibre surface (Figure 5.18) showed that the crystals were a

mixture of $CaCO_3$ and $CaSO_4$ most of it formed as scale clusters consist of $CaSO_4$ as a spherical

polymorph and $CaCO_3$ as a rod-like hexagonal calcite as shown in Figures 5.19 and 5.20, with

some single crystals that look like rhombohedral calcite as shown in Figure 5.21. The

polymorphs of $CaCO_3$ crystals seem to be affected by $CaSO_4$ deposition, whereas the rod-like

polymorph of $CaCO_3$ was the main polymorph in single precipitation of $CaCO_3$. However, in

coprecipitation of $CaCO_3$ and $CaSO_4$ the predominant scales were as clusters.

This result agrees with the results of Sudmalis and Sheikholeslami (2000).[12] They proposed that

the presence of one scale can affect on the other scale in term of structure (Chapter 1). Moreover,

the scale layer formation results are consistent with the results that were observed by Bramson *et al.*(1996)[11] as well as the attenuation results in this study.
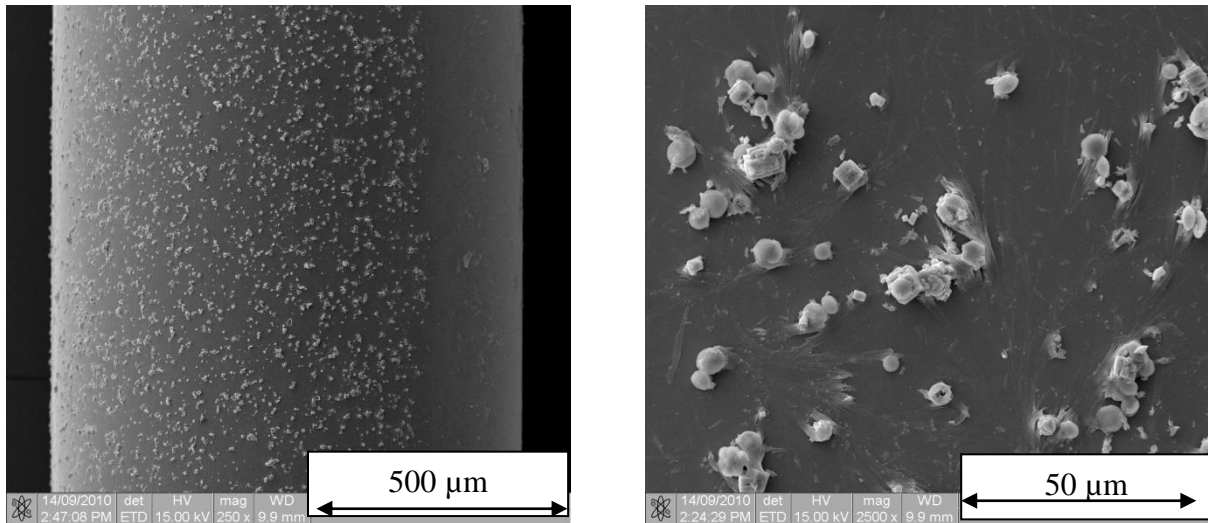
A- SEM image ($\times$ 250) showing a section of an exposed optical fibre core	B- SEM image ($\times$ 2500) showing a crystals of $CaCO_3$ and $CaSO_4$

Figure 5.18- SEM micrographs of an exposed optical fibre core (diameter 1000 µm) in absence of PAA (blank) for coprecipitation of calcium carbonate and calcium sulfate at 120 °C.
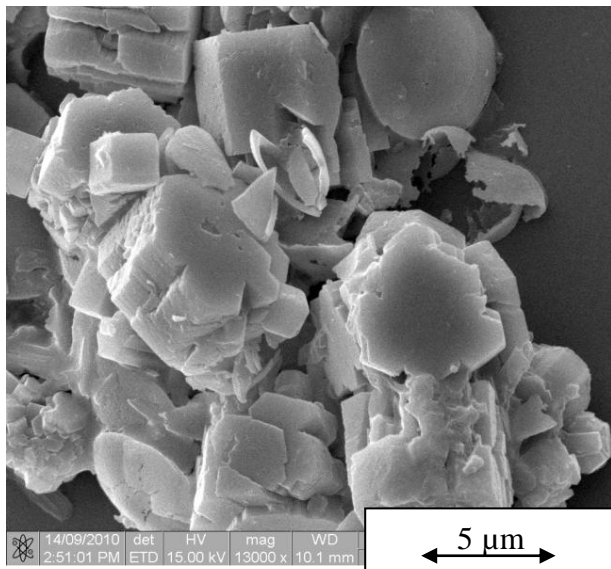
A- SEM image ($\times$ 13000) showing scale clusters consist of CaCO$_3$ and CaSO$_4$
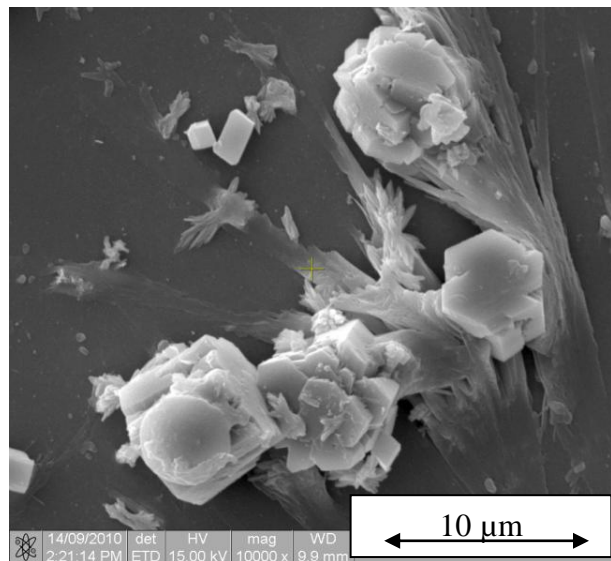
B- SEM image ($\times$ 10000) showing crystals of coprecipitation of CaCO$_3$ and CaSO$_4$ in scale clusters

Figure 5.19- SEM micrographs of an exposed optical fibre core in absence of PAA (blank) for scale clusters showing coprecipitation of calcium carbonate and calcium sulfate.
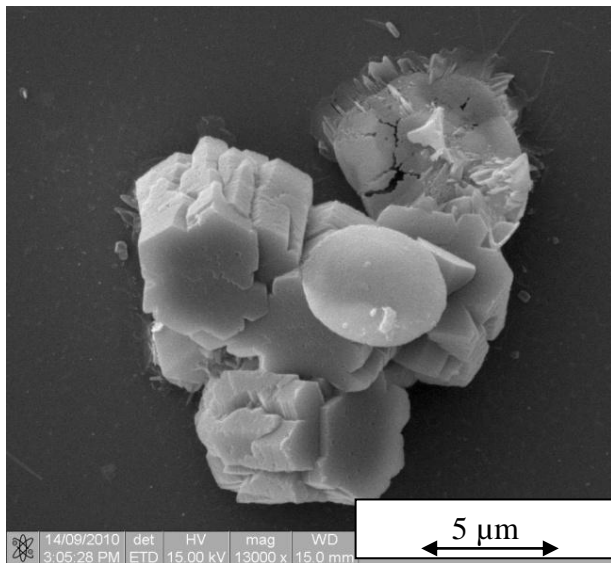
A- SEM image ($\times$ 13000) showing a spherical polymorph of $CaSO_4$ in scale clusters
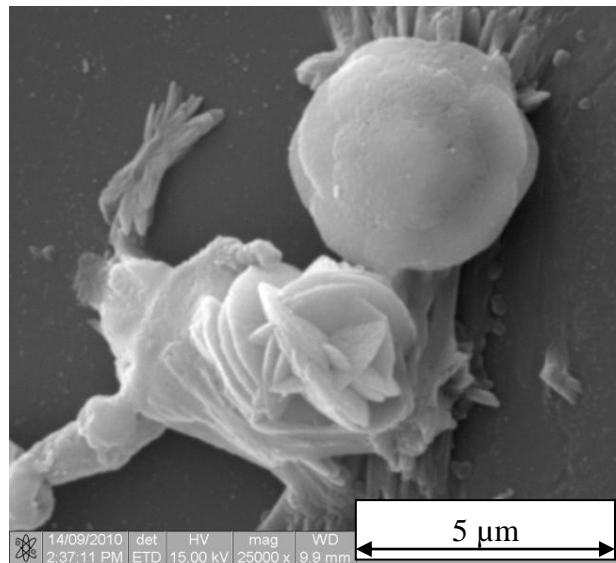
B- SEM micrograph ($\times$ 25000) of $CaSO_4$ as spherical polymorph and $CaCO_3$ as rod-like hexagonal calcite polymorph

Figure 5.20- SEM micrographs of an exposed optical fibre core in absence of PAA (blank) for scale clusters showing coprecipitation of calcium carbonate and calcium sulfate.
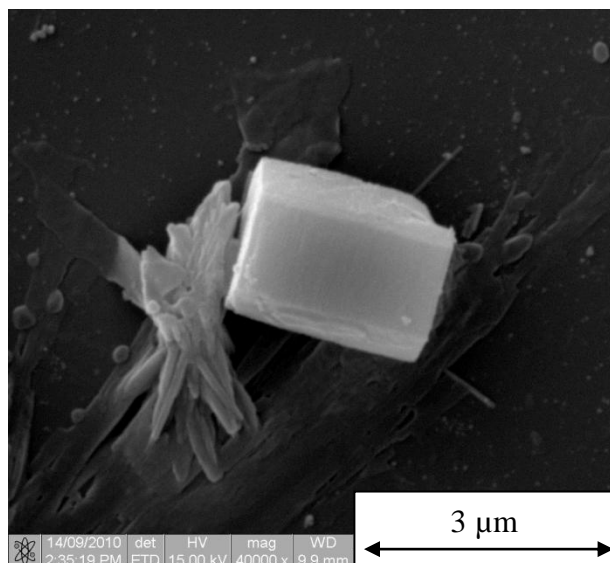
A- SEM micrograph ($\times$ 40000) showing a
single crystal of rhombohedral calcite of
$CaCO_3$
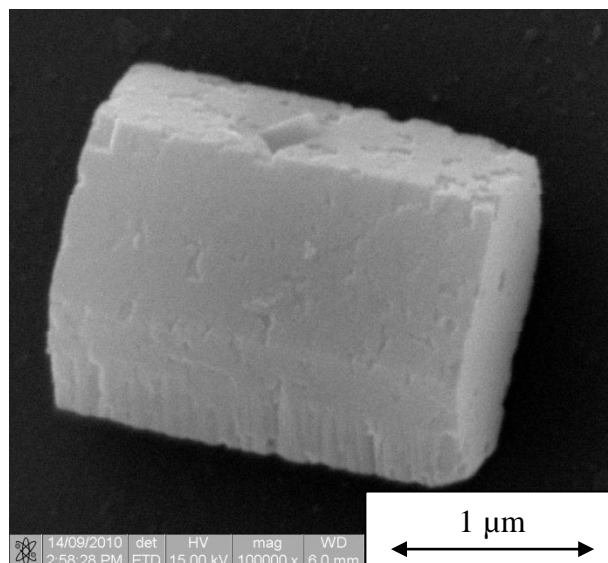
B- SEM micrograph ($\times$ 100000) showing a
single crystal of rhombohedral calcite of
$CaCO_3$

Figure 5.21- SEM micrographs of an exposed optical fiber core in the absence of PAA (blank)

for single crystal formation of coprecipitation of calcium carbonate and calcium sulfate.
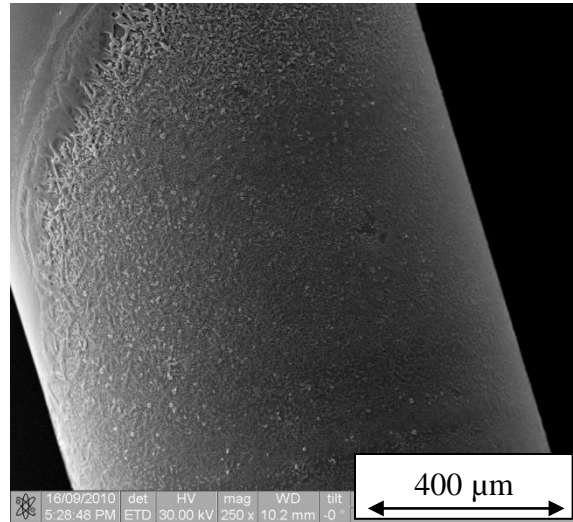
5.4.2.2 In the presence of PAA

No significant change in attenuation of IECOFS sensor in the presence of 10 ppm of CMM-PAA, EIB-PAA, CIB-PAA, HIB-PAA and HDIB-PAA was obtained during the experiments. These results indicated the excellent control of heterogeneous coprecipitation of $CaCO_3$ and $CaSO_4$ by PAA with different end groups at that concentration. The SEM of optical fibre core samples in the presence of PAA with different end groups showed that the optical fibre core were largely clean which agree with attenuation results. While there were some deposits on the surface of optical fibre as shown in Figures 5.22 (A, B) 5.23 (A, B) they do not look like calcite and calcium sulfate dihydrate crystals.

EDS was carried out to determine the main elements in amorphous scales. EDS results showed that the deposit contains a high level of Na, C and S and a low level of Ca which suggests that the deposit was Na_2SO_4 and Na_2CO_3 as shown in Table 5.5, and is only starting material generated by drying of solution containing a large amount of dissolved species onto the fibre.

HIB-PAA and HDIB-PAA significantly reduced the coprecipitation of $CaCO_3$ and $CaSO_4$ on the surface of heat transfer tubes (Figure 5.24).
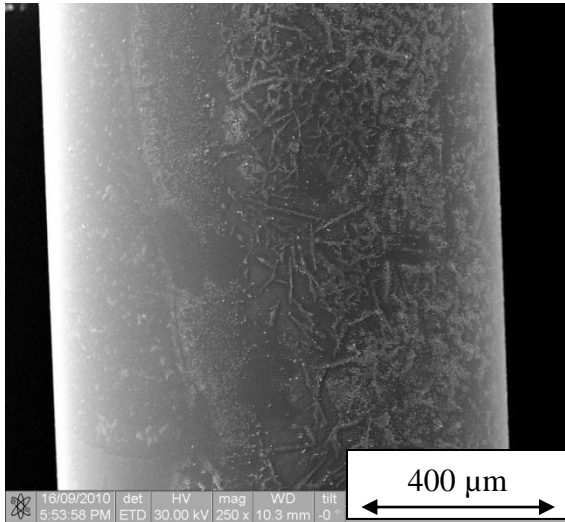
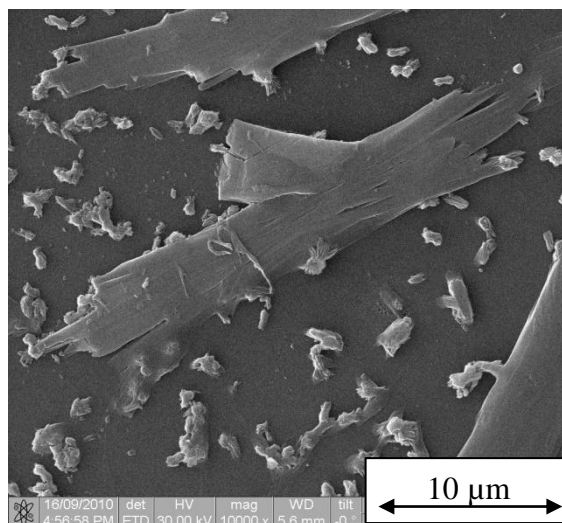| A- SEM micrograph ($\times$ 250) showing a section of an exposed optical fibre core (in the presence of CMM-PAA) | B- SEM micrograph ($\times$ 250) showing a section of an exposed optical fibre core (in the presence of HIB-PAA) |

Figure 5.22- SEM micrographs of an exposed optical fibre core (diameter 1000 µm) for coprecipitation of calcium carbonate and calcium sulfate at 120 °C.
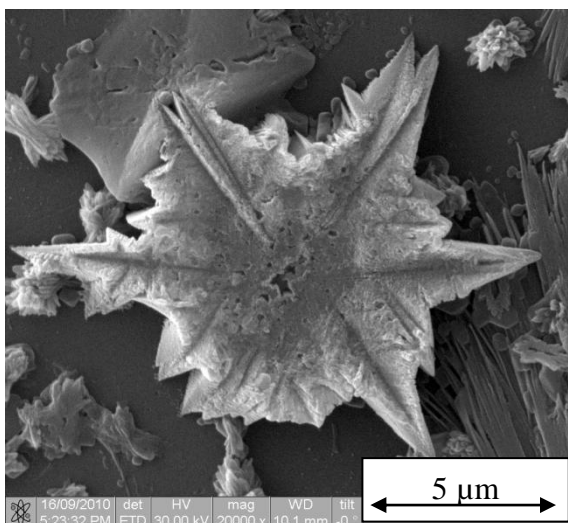
A- SEM micrograph ($\times$ 20000) showing	B- SEM micrograph ($\times$ 10000) showing
deposit of Na_2SO_4 and Na_2CO_3 (in the	deposit of Na_2SO_4 and Na_2CO_3 (in the
presence of HIB-PAA)	presence of HDIB-PAA)

Figure 5.23- SEM micrographs of an exposed optical fibre core (diameter 1000 µm) for

coprecipitation of calcium carbonate and calcium sulfate at 120 °C.

Table 5.5- Main elements in the amorphous deposit that obtained by EDS analysis.

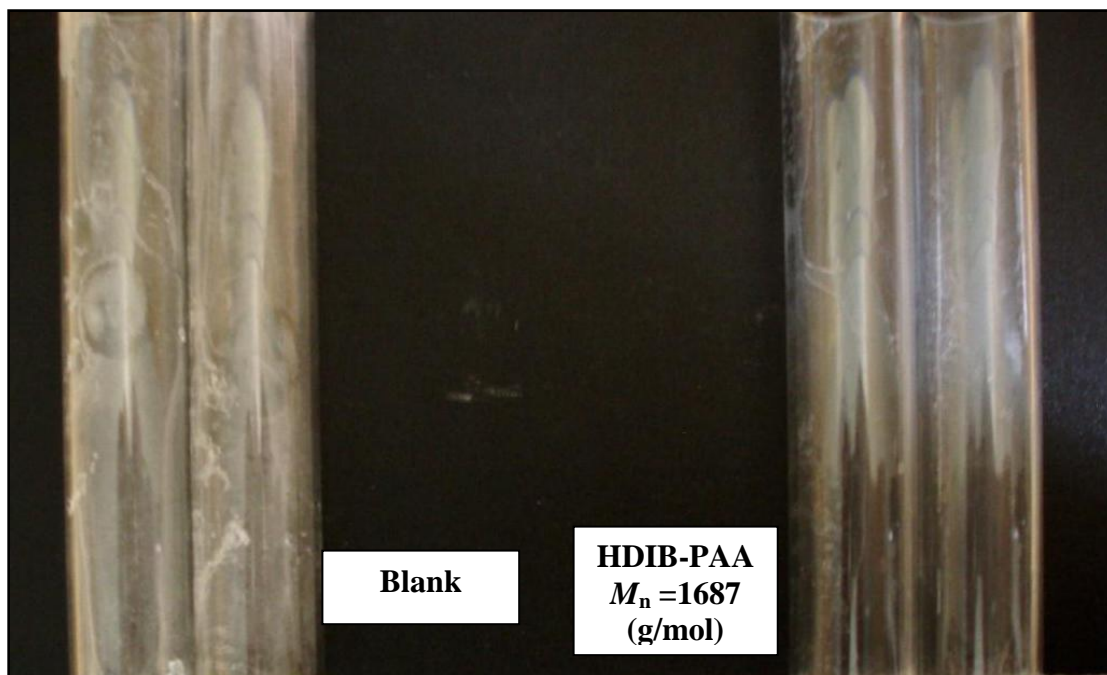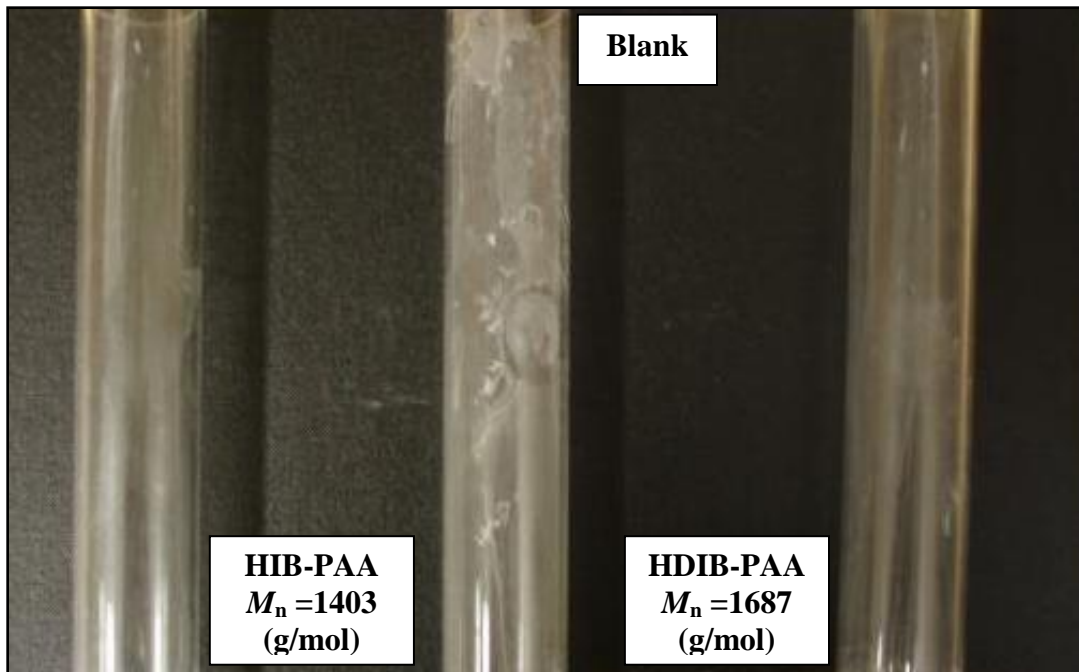| Element	Wt %	At %
C	3.29	5.88
O	39.62	53.21
Na	5.73	5.35
Mg	0.07	0.06
Si	42.72	32.69
S	3.09	2.07
Cl	0.04	0.02
Ca	0.23	0.13
Fe	0.10	0.04
Au	5.12	0.56
Total	100.00	100.00

Figure 5.24- The precipitation on the surface of heat transfer tube in the absence and presence of PAA with HIB and HDIB end group for co-calcium carbonate and calcium sulfate crystallization at 120 °C.

5.5 Conclusion

The heterogeneous precipitation of $CaCO_3$ and coprecipitation of $CaCO_3$ and $CaSO_4$ at 100 - 120 °C were studied using the optical fibre system as IECOFS ed. The effect of PAA ($M_n \leq 2000$ g/mol) with different end groups on the heterogeneous precipitation of $CaCO_3$ at 100 °C was found to be significant. The results showed that the end groups of PAA play very important roles, with mid-length (HIB) and long (HDIB) hydrophobic groups giving an excellent inhibition efficiency to prevent the heterogeneous deposit of $CaCO_3$. Moreover, the results of PAA with short hydrophilic (CMM) and hydrophobic (EIB) and middle hydrophobic (CIB) showed the inhibition efficiency increaseswith increasing the hydrophobicity of end group. However, the results for the inhibition efficiency of PAA with different end groups to prevent the heterogeneous coprecipitation of $CaCO_3$ and $CaSO_4$ at 120 °C showed an excellent inhibition efficiency for PAA with all different end group.

The low molecular mass PAA with long hydrophobic end group (HDIB) showed different inhibition efficiency for homogeneous and heterogeneous precipitation and that may be due to the active surface property which increases with an increase in the ratio of hydrophobic to hydrophilic portion in the PAA.

The IECOFS sensor has some advantages over other conventional methods for monitoring scale precipitation. First is that its response is only for the heterogeneous crystallization on its surface, not crystals formed in suspension. Second is that it can be used at high temperatures and ionic strength such as seawater and brine solution.
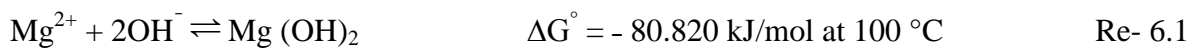
References

1.   Sheikholeslami, R.; Watkinson, A. P. *Journal of Heat Transfer* **1986,** 108, (1), 147-52.

2.   Sheikholeslami, R.; Watkinson, A. P. *Canadian Journal of Chemical Engineering* **1998,** 76, (1), 141-147.

3.   Wallace, A. D.; Boerkamp, M.; Lye, P. G.; Lamb, D. W.; Doherty, W. O. S.; Fellows, C. M. *Industrial & Engineering Chemistry Research* **2008,** 47, (4), 1066-1070.

4.   Boerkamp, M.; Lamb, D. W.; Lye, P. G.; Fellows, C. M.; Al-Hamzah, A.; Wallace, A. D. *Ind. Eng. Chem. Res.* **2010,** 49, (10), 4682-4686.

5.   Tandon, S. P. *Z. Phys. Chem. (Leipzig)* **1965,** 228 (3/4).

6.   de Leeuw, N.; Parker, S. C. *J. Phys. Chem. B* **1998,** 102, 2914-2922.

7.   Altay, E. Effect of Reaction Conditions and Organic Additives on the Morphologies of Synthetic Calcium Carbonate. Izmir Institute of Technology, Izmir, 2006.

8.   Sawada, K. *Pure and Applied Chemistry* **1997,** 69, (5), 921-928.

9.   Yu, S.-H.; Colfen, H. *Journal of Materials Chemistry* **2004,** 14, 2124-2147.

10.   Rieger, J.; Hadicke, E.; Rau, I. U.; Boeckh, D. *Tenside Surf. Det.* **1997,** 34, (6), 430-435.

11.   Bramson, D.; Hasson, D.; Semiat, R. *Desalination* **1996,** 100, (1-3), 105-113.

12.   Sudmalis, M.; Sheikholeslami, R. *The Canadian Journal of Chemical Engineering* **2000,** 78, (1), 21-31.

CHAPTER SIX

Inhibition of Homogeneous Formation of

Magnesium Hydroxide

6.1 Introduction

Magnesium hydroxide $Mg(OH)_2$ formation depends on the concentration of Mg^{2+} and pH of solution. In thermal desalination plants $Mg(OH)_2$ deposit (Re- 6.1) usually appears above 80 °C and predominates in alkaline scale above 100 °C when the concentrations of Mg^{2+} and OH^- exceed the thermodynamic solubility product (K_{sp}). This value of $Mg(OH)_2$ (Eq- 6.1) at that temperature was proposed by H. Hiller (1952).[1-4]

$$Mg^{2+} + 2OH^- \rightleftharpoons Mg\,(OH)_2 \qquad\qquad \Delta G^{\circ} = -\,80.820 \text{ kJ/mol at } 100 \text{ °C} \qquad\qquad \text{Re- 6.1}$$

$$K_{sp} = [Mg^{2+}] \times [OH^-]^2 \qquad\qquad K_{sp} = 4.85 \times 10^{-12} \text{ mole}^3 L^{-3} \quad \text{at } 100 \text{ °C} \qquad\qquad \text{Eq- 6.1}$$

Note: ΔG° and K_{sp} were calculated in Chapter 4.

Several methods have been used to determine the K_{sp} value of $Mg(OH)_2$, such as hydrogen electrode measurements (pH meter) by Gjalbaek, 1925[5] , conductivity method by Nasanen (1941)[6], and glass electrode titration by Whitby, 1933.[7] The K_{sp} value of $Mg(OH)_2$ however, was divergent (2×10^{-9} to 1.2×10^{-11} mole^3 L^{-3} at room temperature). Gjalbaek suggested that $Mg(OH)_2$ can be present in two different crystalline forms, an unstable form having a high solubility forms first which then undergoes recrystallization to form the low solubility polymorph.

The effect of two phosphonate additives (methylenephosphonic acid and N,N,N′N′, ethlenediaminetetramethylenephosphonic acid) on the growth of seed crystals of $Mg(OH)_2$ was studied by Liu and Nancollas (1973).[8] The experimental results showed a significant reduction in crystal growth of $Mg(OH)_2$ by those additives. However, the effect of those scale inhibitors was much less than found for $CaCO_3$ and $CaSO_4$.

This aim of this chapter is to determine the efficiency of low molecular mass ($M_n \leq 2000$ g/mol) PAA with different end-groups as scale inhibitors to retard the homogeneous crystallization of $Mg(OH)_2$ in calcium-free solutions containing non-equivalent concentrations of Mg^{2+} and OH^- ions ($[Mg^{2+}] / [OH^-] > 12$) at high temperature (T = 100 °C) using conductivity measurements.

6.2 Experimental determination of conductivity at 100 °C

A stock solution of 0.823 M (20000 ppm) of Mg^{2+} as $MgCl_2.6H_2O$ was prepared as well as 0.20 M of OH^- as NaOH solution which was prepared daily. These solutions and the RO water used were filtered and degassed using a 0.45 μm Millipore solvent filter.

Filtered deionized water (346.4 mL) was placed in a 500 mL three-neck vertical round-bottom flask containing two platinum conductivity probes (0.3 × 0.3 cm) under a water-cooled glass condenser. 1.4 mL of Mg^{2+} solution as $MgCl_2.6H_2O$ was added to round-bottom flask to give a final concentration of 3.292×10^{-3} (80 ppm) under stirring. When the solution began boiling, recording of conductivity was begun (the first sampling was for the conductivity of Mg^{2+} solution) and 1.75 mL of PAA solution and 0.45 mL of OH^- as NaOH solution were added (15 s from the second sampling) to give a final [PAA] = 5 ppm and $[OH^-] = 2.571 \times 10^{-4}$ M respectively. Conductivity was measured by conductivity meter (CHK Engineering).

Analogue outputs from conductivity prop and spectrophotometer were digitally converted using a Picolog A/D Converter 16 (16 Bit) and Picolog recording software and data was acquired every 300 s as shown in Figure 6.1
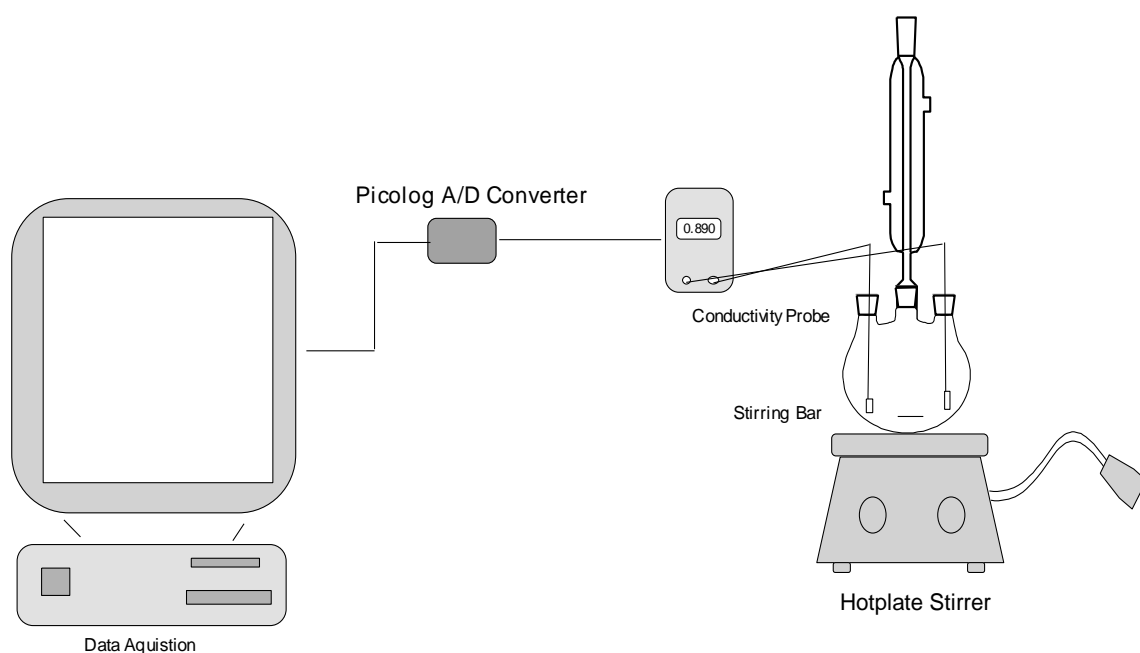
Figure 6.1- The system of conductivity measurement for the homogeneous crystallization of

$Mg(OH)_2$

6.3 Result and discussion

The curves of conductivity with time of solutions containing of $[Mg^{2+}] = 3.292 \times 10^{-3}$ M (80 ppm) and $[OH^-] = 2.571 \times 10^{-4}$ M in the absence and presence of [PAA] = 5 ppm, and T = 100 °C were collected to determine the inhibition efficiency of low molecular mass PAA with different end groups. At those experimental conditions, the supersaturation level (SL) of was calculated as $Mg(OH)_2 = 44.9$ $\left(SL = \frac{Q_{ip}}{K_{sp}}\right)$. The inhibition efficiency (% IE) of PAAs were determined by applying Eq-6.1

$$\% \, IE = \left[1 - \frac{a_{(PAA)}}{a_{(blank)}}\right] \times 100 \tag{Eq -6.1}$$

Where, $a_{(PAA)}$ and $a_{(blank)}$ are the a values in logarithmic equation ($Y = a \times \ln(x) + b$) for conductivity curve after normalization in the presence and absence (blank) of PAA respectively and $x = t$ (time) as shown in Figure 6.2.

Note that all conductivity curves in this Chapter are presented after the normalization of conductivity to initial value of one by applying Eq- 6.2.

$$N.Conductivity = \frac{K_{(t)}}{K_{(o)}} \hspace{4cm} \text{(Eq- 6.2)}$$

Where, $K_{(0)}$ and $K_{(t)}$ are the conductivity value at initial time ($t = 0$) and at any time over the experiment ($t = t$) respectively.

The results of conductivity measurements and (% IE) of homogeneous formation of $Mg(OH)_2$ in the absence of PAA and s in the presence of PAA will be discussed in turn.

6.3.1 In the absence of PAA (blank)

The conductivity curve of homogeneous formation of $Mg(OH)_2$ in the absence of PAA showed increased conductivity for the second sampling compared to the first due to the adding of OH^- solution. As the experiment continued, the conductivity decreased, which indicates more formation of $Mg(OH)_2$ in bulk solution as shown in Figure 6.2.
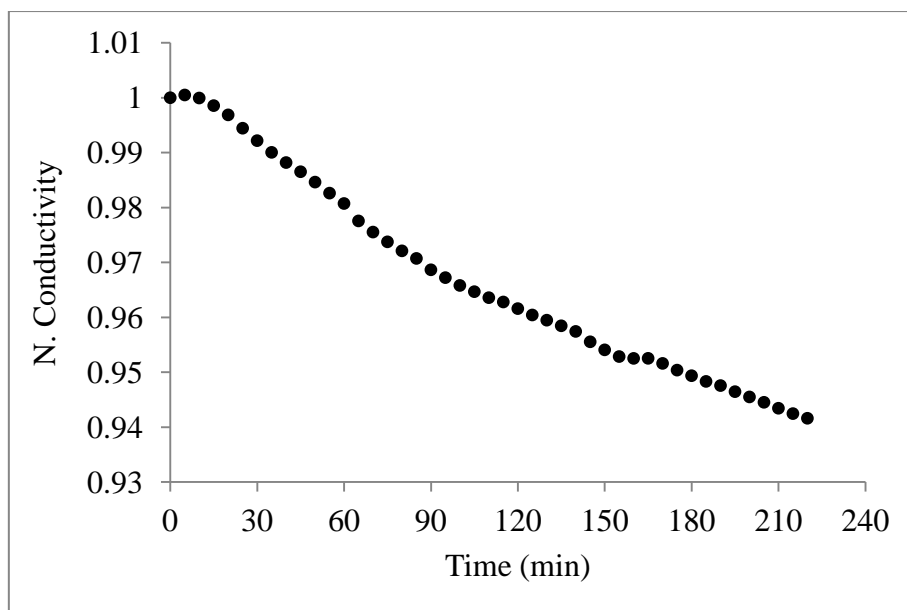
Figure 6.2- The decline of conductivity measurements (after normalization) for homogeneous formation of $Mg(OH)_2$ in the absence of PAA (blank) for more than 3 hours.

The conductivity measurements of $Mg(OH)_2$ formation in absence of PAAs were analysed over the period 5 - 50 min. The decline of conductivity could be fit to a logarithmic curve ($y= a\times \ln (t) +b$) with a good correlation coefficient ($R^2 = 0.98$). However, the system did not reach the steady state even when the experiment continued more than 3 hours as shown in Figure 6.2, indicating $Mg(OH)_2$ formation is slow . Although the formation of $Mg(OH)_2$ under those experimental conditions is thermodynamically favourable ($\Delta G = $ -11 800 kJ) its slow kinetics may be due to the complexation of Mg^{2+} ions with H_2O molecules by strong coordinate bonding as an octahedral structure, making the transition state where all those bonds are broken have a high energy and thus the $Mg(OH)_2$ formation is a slow reaction as shown in Figure 6.3.[3]

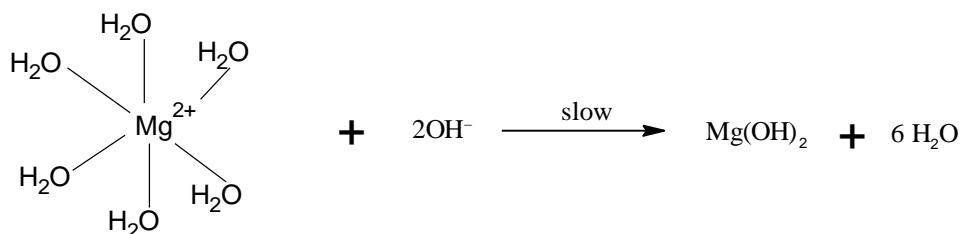Figure 6.3- The formation of $Mg(OH)_2$

6.3.2 In the presence of PAA

All conductivity measurements in the presence of low molecular mass of PAA with different end groups showed a significant decrease in the conductivity. The decreasing conductivity may be due to two reactions. First is the neutralization reaction between carboxylic acid groups in PAA with OH^- ions. Second is the complexation reaction between Mg^{2+} and carboxylate groups in PA^- as shown in Figure 6.4. As the experiment continued, the conductivity decreased and the logarithmic curve indicated more formation of $Mg(OH)_2$ in bulk solution for all PAA with different end groups as shown in Figure 6.5.
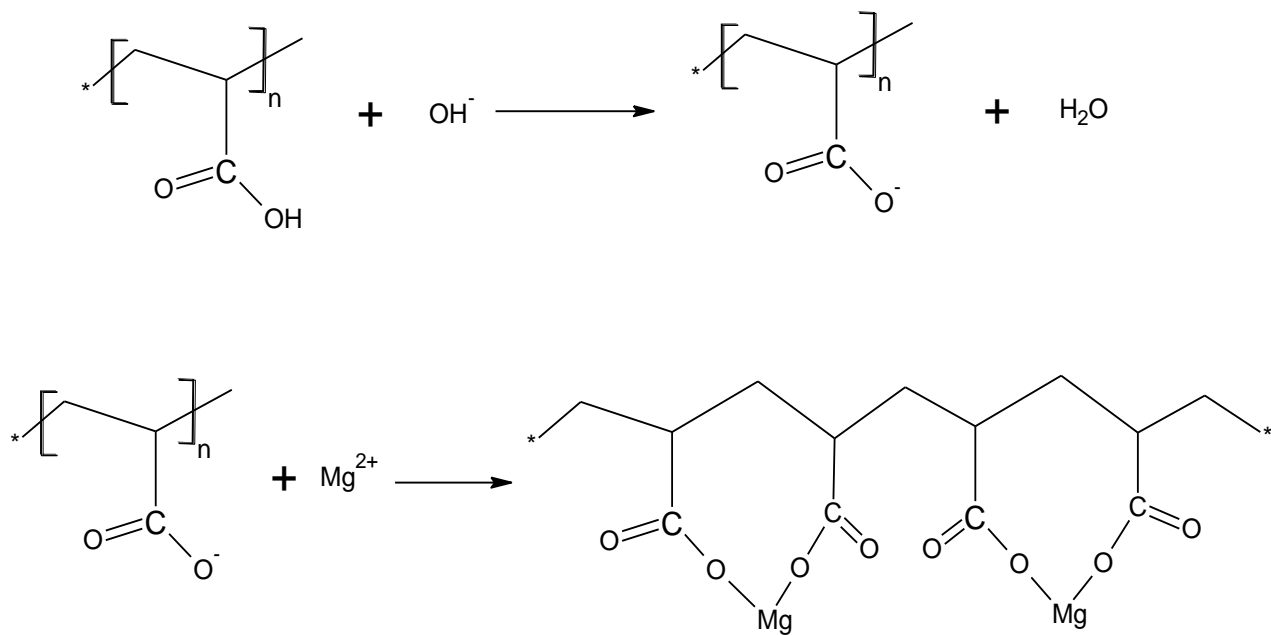
Figure 6.4- The neutralization and complexation reactions between OH^- and Mg^{2+} with carboxylic acid groups in PAA
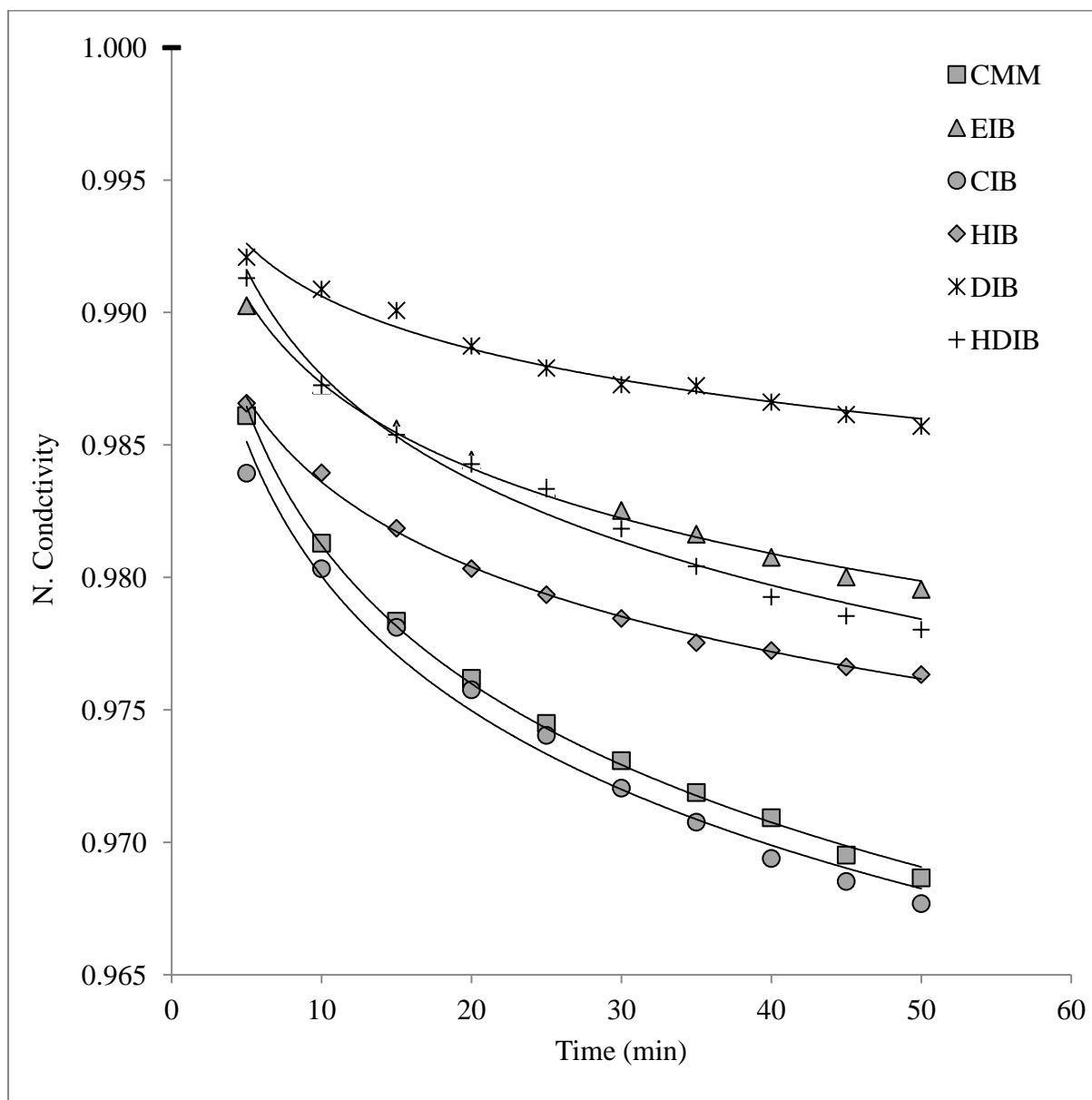
Figure 6.5- Normalized conductivity measurements for solutions containing Mg^{2+}, OH^-

ions and 5 ppm PAA with different end groups ($M_n \leq 2000$ g/mol).

The theoretical residual concentrations of [OH⁻] and [Mg²⁺] ions in the presence of 5 ppm of PAA were calculated based on the number of carboxylic acid units and their concentrations in monomol/L as shown in Table 6.1. The values of residual concentration of [OH⁻] and [Mg²⁺], ΔK_{Exp} (K is the conductivity in μS/cm) for the first 5 minutes, and Q_{IP}/K_{SP} were summarized in Table 6.2.

Table 6.1- The calculation of carboxylic acid units and their concentration in monomol/L unit in the presence of 5 ppm of PAA with different end groups.

End Groups of PAA	M_n	Units (n)	[PAA] (ppm)	[PAA] × 10⁻⁶ (M)	Monomol/L × 10⁻⁵
CMM	2106	29	5	2.374	2.410
EIB	1669	22	5	2.996	2.307
CIB	1689	21	5	2.960	2.176
HIB	1403	17	5	3.564	2.120
DIB	2422	30	5	2.064	2.168
HDIB	1687	19	5	2.964	1.971

Under the experimental conditions, the general % IE (for both complexation and inhibition) of low molecular mass PAA ($M_n \leq 2000$ g/mol) with different end groups to retard Mg(OH)₂ formation was calculated using Eq- 6.1. The results showed the DIB-PAA has the best % IE (74 %) which was clear from the conductivity curve with time (Figure 6.5). In the presence of 5 ppm of DIB-PAA conductivity change was slowest (conductivity (μS) = - 0.00287× ln t ± 0.00032) compared with the other end groups of PAA. Short and middle hydrophobic end groups (EIB-PAA and HIB-PAA) had approximately the same % IE (60 %). However, the lowest % IE was for CMM-PAA and CIB-PAA which were 31 % and 33 % respectively, as shown in Table 6.3 and Figure 6.6.

In the results presented above, PAA with different end groups of molecular mass $M_n \sim 2000$ g/mol generally have a good control of scale deposition of $Mg(OH)_2$. In addition to the effect of molecular mass of scale inhibitor, the results showed the hydrophobicity of the end groups terminating PAA have an important effect. All PAA with hydrophobic end groups have better inhibition efficiency than the hydrophilic end group (CMM) as shown in Figure 6.6. This may be due to the hydrophobic end groups discouraging the PAA chains from desorbing from the nuclei of $Mg(OH)_2$ as fast as PAA with hydrophilic end groups, delaying the growth of the $Mg(OH)_2$ nuclei. The hydrophobic end groups terminating PAA may affect both nucleation and crystal growth, however the hydrophilic end group terminating PAA make the PAA affect on growth greater than the effect on nucleation.

Table 6.2- The residual concentration of $[OH^-]$ and $[Mg^{2+}]$, $\Delta K_{Exp.}$ and SL in the presence of 5 ppm of PAA with different end groups.

End Groups of PAA	M_n (g/mol)	$\Delta_{Exp.}$ N ($K_{0\,s}$ - $K_{300\,s}$)	$[Mg^{2+}]$ $\times 10^{-3}$	$[OH^-]$ $\times 10^{-4}$	SL
Blank	-	-	3.929	2.571	45
CMM	2106	0.0139 ± 0.0013	3.154	1.882	23
EIB	1669	0.0097 ± 0.0033	3.160	1.912	24
CIB	1689	0.0161 ± 0.0037	3.168	1.949	25
HIB	1403	0.0104 ± 0.0020	3.171	1.965	25
DIB	2422	0.0079 ± 0.0020	3.168	1.952	25
HDIB	1687	0.0087 ± 0.0027	3.179	2.008	26

Table 6.3- The effect of PAA with different end groups in $Mg(OH)_2$ formation. $[Mg^{2+}] = 80$ ppm, pH =10.28 &T= 100 °C

$$Y = a \times \ln(t) + b$$

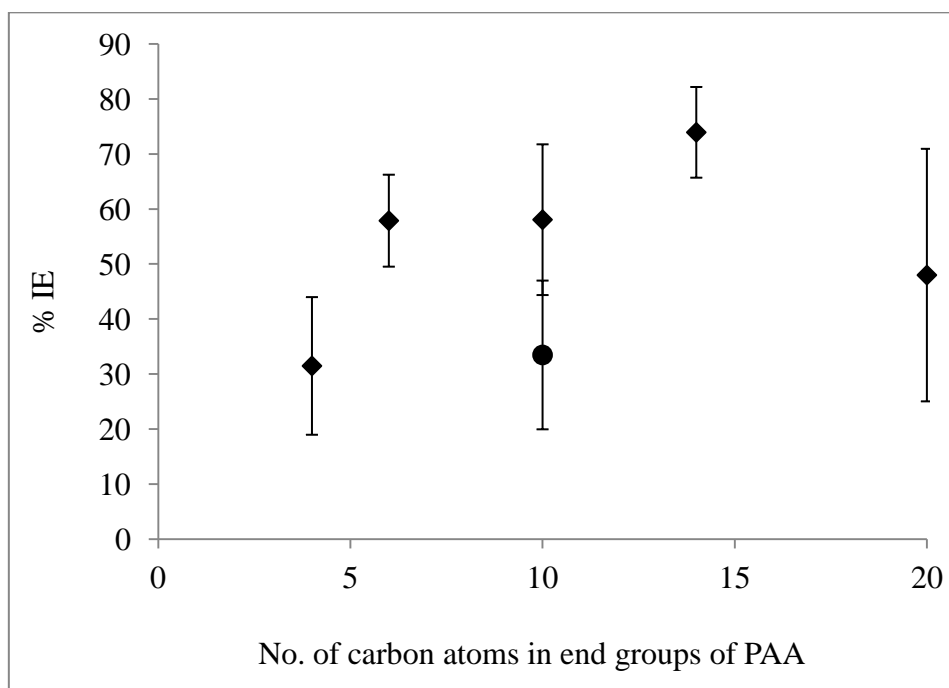| End Groups of PAA	M_n (g/mol)	a	R^2	% IE
Blank	-	-0.01102 ± 0.00100	0.978	0
CMM	2106	-0.00755 ± 0.00300	0.998	31 ±12
EIB	1669	-0.00464 ± 0.00067	0.994	58 ±8
CIB	1689	-0.00733 ± 0.00296	0.983	33 ±14
HIB	1403	-0.00462 ± 0.00109	0.982	58 ±14
DIB	2422	-0.00287 ± 0.00032	0.977	74 ±8
HDIB	1687	-0.00573 ± 0.00274	0.985	48 ±23

Figure 6.6- % IE of $Mg(OH)_2$ formation by PAA with different end groups ($M_n \leq 2000$).

($\bullet$ = CIB)

6.3.3 The estimation of order and crystal growth rate (CGR) for Mg(OH)$_2$ formation

The supersaturation level is a very important factor affecting the rates of nucleation and crystal growth.[9] The model that was proposed by Liu and Nancollas [8] for Mg(OH)$_2$ crystallization (Eq- 6.3) was used to estimate the order and rate of crystal growth for Mg(OH)$_2$ formation by analysing the conductivity data obtained in this study.

$$\frac{-d[Mg^{2+}]}{dt} = k_c S \left\{ ([Mg^{2+}] \times [OH^-]^2)^{\frac{1}{3}} - \left(\frac{K_{sp}}{f_1^2 \times f_2}\right)^{\frac{1}{3}} \right\}^n \qquad \text{Eq- 6.3}$$

In this model k_c is the rate coefficient for crystal growth, S is a function of the number of effective sites added as seed crystals and n is the order of crystal growth with respect to supersaturation of Mg(OH)$_2$.[8]

The estimation of n was done by plotting $\log \frac{-d[Mg^{2+}]}{dt}$ versus $\log\{([Mg^{2+}] \times [OH^-]^2)^{1/3} - (K_{sp})^{1/3}\}$ where the slope $= n$, as shown in Figure- 6.7. The rate of crystal growth for Mg(OH)$_2$ was determined from the plot of $\log \left\{ \frac{[Mg^{2+}]_i - [Mg^{2+}]_o}{[Mg^{2+}]_t - [Mg^{2+}]_o} \right\}$ versus time (t) where, $[Mg^{2+}]_i$, $[Mg^{2+}]_t$ and $[Mg^{2+}]_o$ are the initial concentration, the concentration at t and the concentration at equilibrium of Mg^{2+} respectively. The concentration $[Mg^{2+}]_i$ was equal to the residual of Mg^{2+} ions in solution after that all OH$^-$ ions reacted with Mg^{2+} to form Mg(OH)$_2$ at equilibrium stage (the equilibrium constant value of Mg(OH)$_2$ formation at 100 °C , $K_{eq} = 2.06 \times 10^{11}$). The concentration of Mg^{2+} at time (t) was calculated from conductivity data over the course of the experiment using ionic conductance values of Mg^{2+}, OH$^-$, Cl$^-$ and Na$^+$ at 100 °C which were estimated from their ionic conductance values at 25 °C using Eq 6.4 (Table 6.4). (CRC Handbook of Chemistry and Physics)

$$\lambda_{i,T}^0 = \lambda_{i,25\,°C}^0 \left[1 + \alpha(T - 25°C)\right] \qquad \text{(Eq 6.4)}$$

Where α is a temperature coefficient and its value for all ions ≈ 0.02 $°C^{-1}$ except H_3O^+ ($\approx$ 0.0139 $°C^{-1}$) and OH^- (≈ 0.018 $°C^{-1}$).

Table 6.4- Ionic Conductance of Mg^{2+}, Na^+, OH^- and Cl^- at 25 and 97.2 °C (CRC Handbook of Chemistry and Physics)

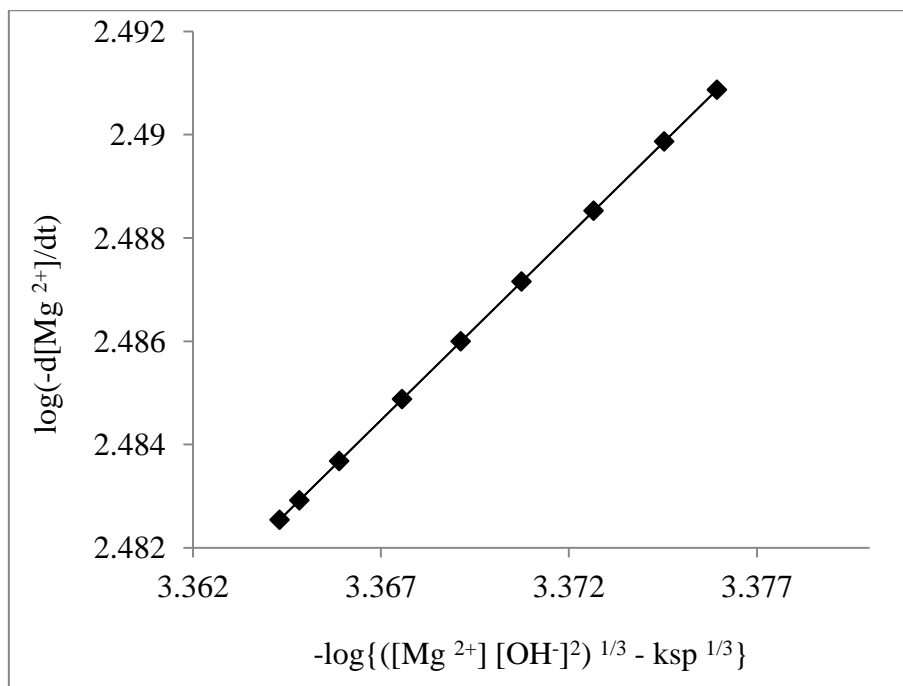| Ions	$(S·cm^2/ eq)/1000$ (25 °C)	$(S·cm^2/ eq)/1000$ (100 °C)
Mg^{2+}	0.053	0.133
OH^-	0.1991	0.468
Na^+	0.051	0.125
Cl^-	0.076	0.191

Figure 6.7- The plot of $\log \dfrac{-d[Mg^{2+}]}{dt}$ versus $\log\{([Mg^{2+}] \times [OH^-]^2)^{1/3} - (K_{sp})^{1/3}\}$ to determine n for the crystal growth of $Mg(OH)_2$ in the absence of PAA.
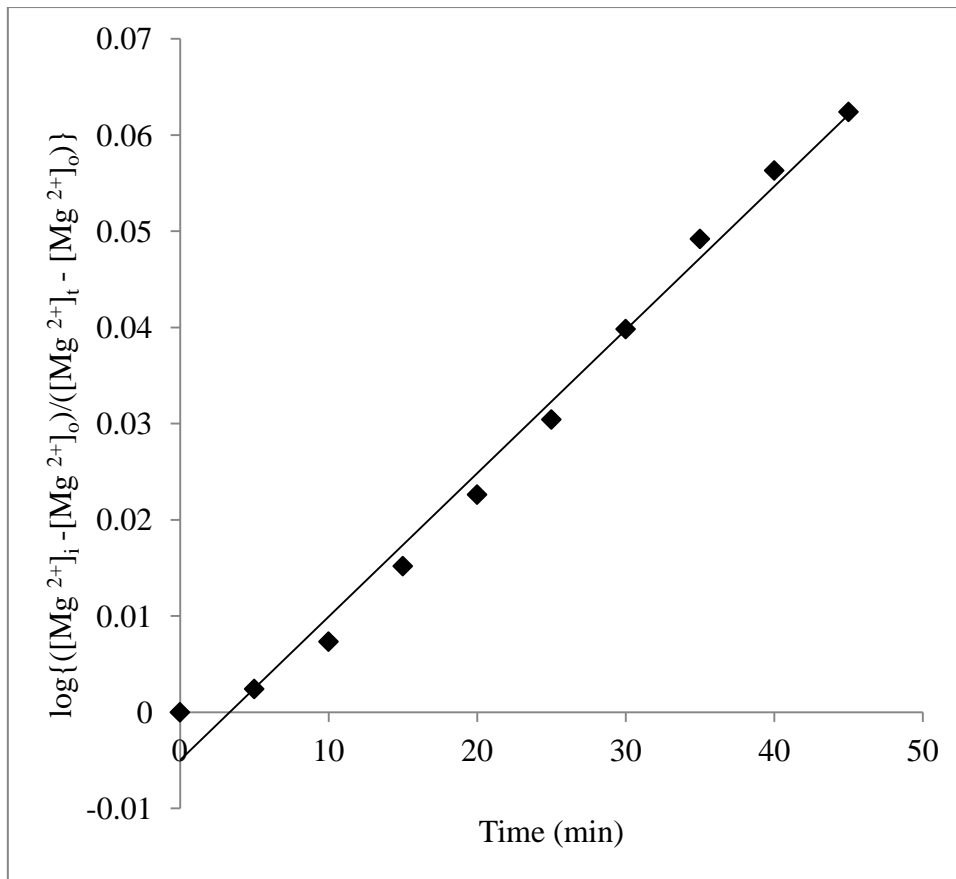
Figure 6.8- The plot of $log\left\{\frac{[Mg^{2+}]_i - [Mg^{2+}]_o}{[Mg^{2+}]_t - [Mg^{2+}]_o}\right\}$ versus time (t) to determine the rate of crystal

growth of $Mg(OH)_2$ in the absence of PAA.

The results of the estimations of the order of crystal growth (n) and the crystal growth rate for

homogeneous formation of $Mg(OH)_2$ in solution containing non-equivalent concentrations of

Mg^{2+} and OH^- ions in the absence and present of PAAs are summarized in Table 6.5. Those

results showed the order (n) of $Mg(OH)_2$ formation with respect to supersaturation in the

absence and presence of PAAs was 0.72 and 0.66 respectively. The small difference between

the values may be due to the reduction in concentration of Mg^{2+} and OH^- ions in the

presence of PAA as a result of neutralization and complexation reactions. Those results agree

with the results obtained by Dabir (1982) who observed "the kinetics of $Mg(OH)_2$ are a

sensitive function of pH", whereas the order of $Mg(OH)_2$ formation decrease when the

concentration of OH$^-$ ions decrease. The order of Mg(OH)$_2$ formation in the presence of excess magnesium ions (20 %) was 1.0 ± 0.3 at room temperature.[9]

The rate of crystal growth for homogeneous formation of Mg(OH)$_2$ significantly decreased with different values in the presence of PAAs as shown in Figure-6.9. The decrease may be due to two effects. The first effect is the increase in the ratio of [Mg^{2+}]/[OH$^-$] in the presence of PAAs as shown in Table- 6.5 for those experiments carried out in the presence of more excess magnesium ions in solution when compared in the absence of PAA (blank). Larson and Buswell (1940)[10] proposed that, the Mg^{2+} ions in the supersaturated solution "are more strongly adsorbed by the crystal surface than [OH$^-$] ions and when the latter are in excess, the rate constant for crystal growth is increased". Those results agree with the results obtained by Liu and Nancollas (1973)[8] where the rate of crystal growth decreased in the presence of excess magnesium ions.

The second effect is the adsorption of PAA on active nucleus surfaces of Mg(OH)$_2$. This effect appeared clearly for different values of the rates of crystal growth in the presence of PAA with different end groups, where if the first effect was the only reason for the decrease in rate of crystal growth, the rate of crystal growth value would be approximately the same in all cases. The different values of the rate of crystal growth in the presence of PAA with different end groups indicated that the complexation of carboxylate groups with Mg^{2+} in PA$^-$ was not for all of them (fully) as was supposed initially. The amount of complexation was estimated as outlined below.

Table 6.5- The order (n), rate of crystal growth K_cS and ratio of $[Mg^{2+}]/[OH^-]$ for $Mg(OH)_2$ crystallization

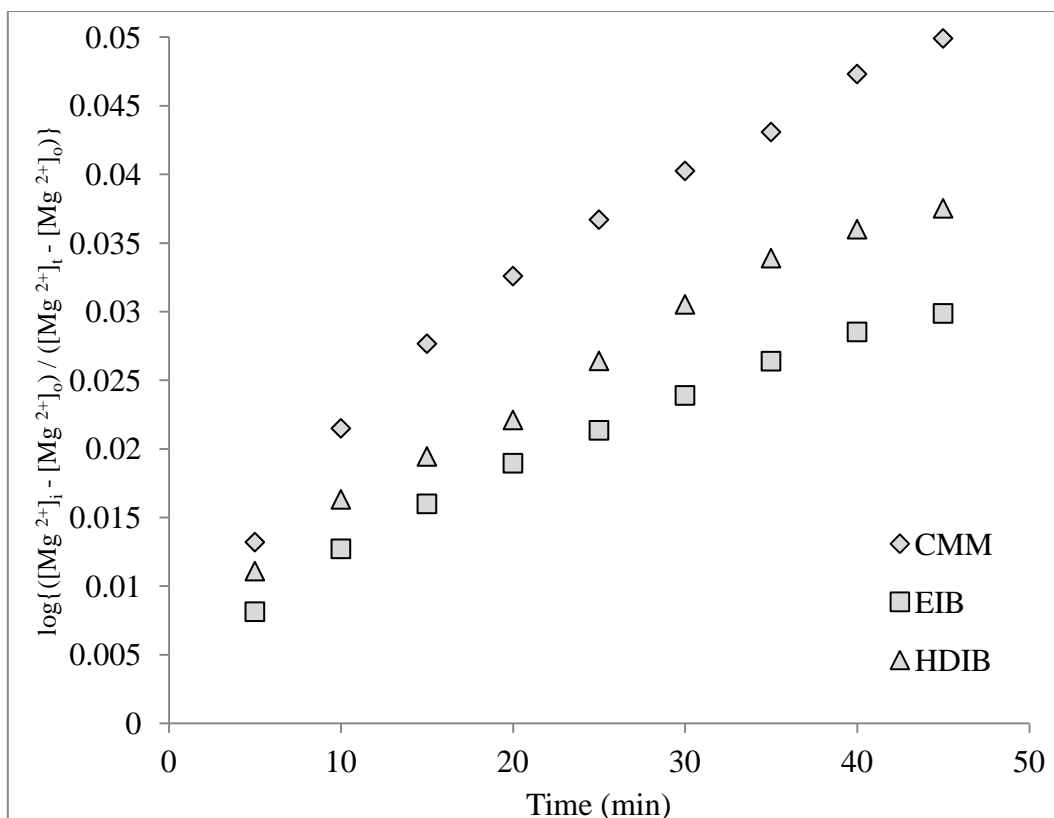| End Groups of PAA	n	K_cS (min^{-1}) Rate of crystal growth	% of retardation	$[Mg^{2+}]/[OH^-]$
Blank	0.72	1.491×10^{-3}	0	12.8
CMM	0.65	1.015×10^{-3}	32	16.8
EIB	0.65	0.613×10^{-3}	59	16.5
CIB	0.65	1.012×10^{-3}	32	16.3
HIB	0.66	0.601×10^{-3}	60	16.1
DIB	0.66	0.378×10^{-3}	75	16.2
HDIB	0.66	0.773×10^{-3}	48	15.8

Figure 6.9- The plot of $log\left\{\frac{[Mg^{2+}]_i - [Mg^{2+}]_o}{[Mg^{2+}]_t - [Mg^{2+}]_o}\right\}$ versus time (t) to determine the crystals growth of $Mg(OH)_2$ in the presence of PAA with different end groups.

The ratio of complexation (% RC) that taken place between carboxylate groups in PA^- with Mg^{2+} can be determined by applying Eq- 6.5:

$$\% RC = \frac{(\Delta K_{Exp.})_{ave}}{(\Delta K_{Etheor.})_{ave}} \times 100 \qquad \text{Eq- 6.5}$$

Where $(\Delta K_{Etheor})_{ave.}$ is the average theoretical reduction in conductivity when the complexation is 100% which was equal to 0.0380 and $(\Delta K_{Exp.})_{ave}$ is the average experimental reduction in conductivity for the first sampling after OH^- ions was added to Mg^{2+} solution regardless of the conductivity of OH^- ions which was equal to 0.0116. The results suggest that more than 69 % of carboxylate groups in PA^- were not complexed by Mg^{2+}.

6.4 Conclusion

The inhibition efficiency of low molecular mass ($M_n \leq 2000$ g/mol) PAA with different end-groups to prevent $Mg(OH)_2$ formation in solution containing non-equivalent concentrations of Mg^{2+} and OH^- ions at 100 °C was studied by using conductivity measurements.

The results showed the hydrophobicity of the end group of low molecular mass PAA affects in the inhibition of $Mg(OH)_2$ deposit. Low molecular mass of PAA with long hydrophobic (DIB) end group showed the highest % IE, however the low molecular mass of PAA with hydrophilic end group (CMM) showed the lowest % IE. The conductivity data in the presence of PAAs witf different end groups illustrated that two consecutive reactions take place. The First reaction was the neutralization of carboxylic acid groups in PAA by OH^- ions. The second reaction was the complexation of carboxylate groups in PA^- with Mg^{2+}.

The order and rate of crystal growth with respect to supersaturation of $Mg(OH)_2$ crystallization were estimated based on Liu and Nancollas expression for $Mg(OH)_2$ formation at low temperature. The results showed a significant decrease in the rate of crystal growth of $Mg(OH)_2$ in the presence of PAA with different end groups. The decrease in crystal growth may be due to two effects. First is the increase in ratio of $[Mg^{2+}]/[OH^-]$ in the presence of PAAs, whereas the rate of crystal growth decreased in the presence of excess magnesium ions. Second is the adsorption of PAA on active nucleus surface of $Mg(OH)_2$ which appear clearly in the different values of the rates of crystal growth in the presence of PAA with different end groups.

References

1.   Shams El Din, A. M.; El-Dahshan, M. E.; Mohammed, R. A. *Desalination* **2005,** 177, (1-3), 241-258.

2.   Hiller, H., In *Proc. Inst. Mech. Engrs*, london, 1952; Vol. 1B, p 295.

3.   Mubarak, A. *Desalination* **1998,** 120, (1-2).

4.   Shams El Din, A. M.; El-Dashan, M. E.; Mohammed, R. A. *Desalination* **2002,** 142, (2), 151-159.

5.   Gjalbaek, J. K.; Anorg, Z. *Allgem. Chem.* **1925,** 144, 269.

6.   Nasanen, R. *Z.physik. Chem.* **1941,** 188, 272.

7.   Whitby, L. *Trans. Faraday Soc.* **1933,** 29, 844-853.

8.   Liu, S.-T.; Nancollas, G. *Desalination* **1973,** 12, 75-84.

9.   Dabir, B.; Peters, R. W.; Stevens, J. D. *Ind. Eng. Chem. Fundam* **1982,** 21, 298-305.

10.   Larson, T. E.; Buswell, A. M. *Ind. Eng. Chem.* **1940,** 32, 132-134.